PHENOMENOLOGICAL MODELING OF CIRCULAR ARRAYS OF DIPOLE-ANTENNAS

MOHAMMAD ASADUZZAMAN KHAN

Ph.D

The Hong Kong Polytechnic University

2018

The Hong Kong Polytechnic University

Department of Electronic and Information Engineering

Phenomenological Modeling of Circular Arrays of Dipole-antennas

Mohammad Asaduzzaman KHAN

A thesis submitted in partial fulfilment of the requirements for the degree of Doctor of Philosophy

February 2018

CERTIFICATE OF ORIGINALITY

I hereby declare that this thesis is my own work and that, to the best of my knowledge and belief, it reproduces no material previously published or written, nor material that has been accepted for the award of any other degree or diploma, except where due acknowledgement has been made in the text.

————————————————————(Signed)

Mohammad Asaduzzaman KHAN

————————————————————(Name of the student)

Abstract

In an array of antennas, the inter-antenna mutual coupling can greatly affect the array's overall performance in various application, such as direction-of-arrival (DOA) estimation and beamforming. For a uniform circular array (UCA) of identical dipoles oriented perpendicular or radial to the circle plane, this thesis advances a simple expression of their electromagnetic mutual impedance, in simple closed forms, explicitly in terms of the dipoles' length (L), the number (M) of dipoles comprising the array, and the circular array grid's radius (R).

This simple model is obtained via a "behavioral" (a.k.a. "phenomenological" or "block-box") approach, which is new to UCA inter-antenna mutual coupling modeling. This "phenomenological" or "behavioral" approach takes mutual impedance data, (generated by Method-of Moments (MoM) electromagnetic simulations) to fit into a low-dimensional manifold. Such an approach is commonplace in modeling wireless fading channels and the nonlinear amplifier's input/output relationship, though admittedly can be used to mutual coupling modeling. Despite the conceptual simplicity of this approach, subsequently presented results will demonstrate its success to yield simple rule-of-thumb relationships of how the mutual impedance varies with the wavelength-normalized dipole length ($\frac{L}{\lambda}$), the number M of such dipoles in the circular array, and the circle's radius ($\frac{R}{\lambda}$).

Acknowledgements

First of all, I am grateful to Almighty Allah for giving me strength and ability to continue this course of study.

I would like to express my deep and sincere gratitude to my honourable chief supervisor, Dr. Kainam Thomas WONG, for his excellent guidance, endless inspiration, encouragement, and continuous unconditional support throughout the research. Dr. WONG dedicated a lot of precious time to nurture my academic knowledge and intellectual ability with the patient. Beside the study Dr. Wong has given me a lot of moral support to overcome all the difficulties and complexities I faced on during my study period.

I am grateful to my co-supervisor, Dr. Wai-Yip TAM, for his admirable guiding, advising, checking, correcting, and enhancing this research work in view of electromagnetics consideration. Dr. TAM's contributions have been of the great value of the success of this investigation.

I am thankful to Dr. Caleb J. FULTON for his intellectual suggestions to get the phenomenological models explainable from the electromagnetics aspects.

It gives me great pleasure to offer my profound gratitude to Dr. Yue Ivan WU, for his limitless support in conducting the four-dimensional (4D) least-squares model fitting, and to show the usefulness of this research work by direction-of-arrival (DOA) estimation's derivations with MATLAB code.

I wish to express my sincere and whole-hearted appreciation and gratitude to all the faculty members of the Department of Electronic and Information Engineering (EIE). I am grateful to the Hong Kong Polytechnic University for providing the postgraduate studentship. I would also like to thank the research staffs, and students of the Department of EIE for making my research period fruitful. Also, I am thankful to Gerald P. ARADA and Salman KHAN, who introduced me the EMCoS VLab computer simulation software and help me to the DOA estimation MATLAB code for radially oriented dipoles array respectively.

Finally, I would like to thank my family, especially my parents, my wife Khalada NAHAR, and my beloved son Ayaan AREEB (Sahil) for their sacrifice, support, and encouragement during my PhD programme.

Table of Contents

List of Figures

List of Tables

Chapter 1

Introduction

1.1 Overview

The performance of a single antenna is imprudent for various application fields, such as radar, radio astronomy, localization in communications, and medical diagnosis where often uses several antennas in a group, i.e. as an antenna array.

In practice there are several arrays available for example linear array, circular array, planar array, rectangular array, and triangular array. This thesis has investigated the uniform circular array among the above mentioned arrays because of it's nice properties of diversity reception and circularly symmetrical by a $\frac{2\pi}{M}$ radians rotation about the circle's origin, where M is the number of antenna. Figures 1.1-1.2 are some practically used examples of uniform circular array for direction finding.

However, these antennas (in an array) electromagnetically interact with each other, such that one antenna's voltage affects its neighboring antennas' voltages, this phenomenon is called mutual coupling. This mutual coupling could greatly change the overall array's operation. This mutual coupling

Figure 1.1: Circular array of antenna system, company name ARTIKUL-S direction finder. This is design by IRCOS company [1].

Figure 1.2: Circular array round-the-clock radio navigation, security and unauthorized sources of radiation detection in the Republic of Armenia [2].

depends on many factors like the antenna type, the array geometry, the number of antennas in an array, and the inter-antenna spacings.

1.2 The Critical Effects of Mutual Coupling in Antenna-Array Signal Processing

An antenna array can separate incident emitters and can localize them, based on their different incident directions-of-arrival (DOAs) besides based on their signals' different time-frequency structures. An antenna array can also facilitate transmission, e.g., in massive MIMO communications / radar.

The use of antennas as sensing devices or as transmission devices is predicated on their measurements (transmissions) having a known relationship to the electromagnetic phenomenon being measured (effected), i.e., how the antennas voltages are related to the incident (transmitted) electromagnetic wave-field. This foundational presumption is often unmet in reality, especially for an array of close-by antennas which induce electric currents on each other, producing inter-antenna mutual coupling. Such antenna arrays are widely used in wireless sensing and wireless communications. Thousands of signal-processing algorithms have been devised over the decades.

At the core of such thousands of antenna-array signal-processing algorithms is a typical requirement for some prior knowledge on how the antenna array, as a unit, would correspond to the incident electromagnetic wave-field, as a function of the wave-field's frequency, azimuth-elevation direction-of-arrival, and polarization. This "response", termed an "array manifold", depends not only on the inter-antenna spatial geometry, but also should depend on the inter-antenna electromagnetic coupling, which is often overlooked or arbitrarily oversimplified.

However, inter-antenna mutual coupling complicates these antenna-array signal-processing algorithms, which typically simply "idealizes away" or over-simplifies much of such electromagnetic realities. Why is electromagnetic coupling "idealized away" in the signal-processing literature? It is because the electromagnetic effects require complicated mathematical descriptions, typically involving nested layers of integrals and/or summations with respect to several independent variables [4, 5, 18, 25, 37]. For example, one single mutual-coupling expression occupies 6 pages in [11]. Such complicated descriptions, obtained by analytical solutions to the Maxwell's equations, are too convoluted to lend themselves to "elegant" signal-processing algorithmic paradigms.

In antenna-array signal processing (such as beamforming, direction finding, tracking, diversity transmission/reception), the signal processing algorithms generally are predicated on a prior knowledge of the precise mathematical inter-relationship among the various antennas that comprise the array. This inter-antenna relationship (at any particular frequency) may be encapsulated as a vector of scalar functions. This vector, called an "array manifold" and denoted as $\mathbf{a}(\phi, \theta, \lambda)$, mathematically relates the incident signal's DOAs (ϕ, θ) in azimuth/elevation (see figure 1.3) and wavelength (λ) to the array's M constituent antennas' data measurement, which may be represented as a $M \times 1$ vector $\mathbf{X}(t)$ at time t:

$$\mathbf{X}(t) \;=\; \int_{\forall \lambda} \mathbf{a}_{\text{presumed}}(\phi, \theta, \lambda)\; s(\lambda)\; e^{j2\pi ct/\lambda} d\lambda, \tag{1.1}$$

where $s(\lambda)$ represents the incident signal's frequency spectrum (or the spectrum expressed here in terms of wavelength, in order to ease the subsequent exposition), and c symbolizes the speed of light.

If the array manifold $\mathbf{a}_{\text{presumed}}(\phi, \theta, \lambda)$ *presumed* in a signal-processing algorithm deviates from the actual array manifold $\mathbf{a}_{\text{actual}}(\phi, \theta, \lambda)$ in physical

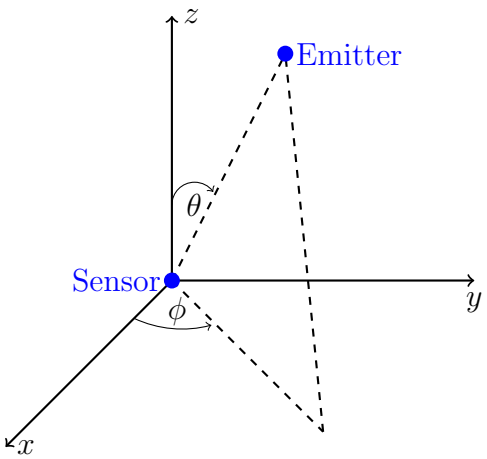

Figure 1.3: Azimuth (ϕ) and elevation (θ) angles.

reality, model mismatch would occur and would degrade the signal-processing algorithm's nominal performance.

One physical actuality, often overlooked/oversimplified, is the electromagnetic coupling across the antennas comprising the antenna-array of the wireless transceiver. This "mutual coupling" would require $\mathbf{a}_{\text{presumed}}(\phi, \theta, \lambda) = \mathbf{a}_{\text{coupling}}(\phi, \theta, \lambda)$ in equation (1.1), instead of an ideally presumed $\mathbf{a}_{\text{presumed}}(\phi, \theta, \lambda) = \mathbf{a}_{\text{no-coupling}}(\phi, \theta, \lambda)$. The estimates $(\hat{\phi}, \hat{\theta})$ to be extracted from $\{\mathbf{X}(t),\ t = t_1, t_2, \cdots, t_N\}$ would obviously be very different, depending on whether the estimator signal-processing algorithm *correctly* presumes $\mathbf{a}_{\text{presumed}}(\phi, \theta, \lambda) = \mathbf{a}_{\text{coupling}}(\phi, \theta, \lambda)$ or *in*correctly presumes $\mathbf{a}_{\text{presumed}}(\phi, \theta, \lambda) = \mathbf{a}_{\text{no-coupling}}(\phi, \theta, \lambda)$.

Take the example of direction finding using a UCA of dipoles spacing uniformly on a circle and oriented vertically. Their *actual* array manifold (accounting for mutual coupling) may be represented as a $M \times 1$ vector function, $\mathbf{a}^{(\text{UCA})}_{\text{actual}}(\phi, \theta, \lambda) := \mathbf{C}(\lambda)\, \mathbf{a}^{(\text{UCA})}_{\text{no-coupling}}(\phi, \theta, \lambda)$, where

$$\mathbf{a}^{(\mathrm{UCA})}_{\mathrm{no-coupling}}(\phi,\theta,\lambda) \;:=\; \alpha \begin{bmatrix} d_{1,1}(\phi,\theta,\lambda) \\ d_{2,1}(\phi,\theta,\lambda) \\ \vdots \\ d_{M,1}(\phi,\theta,\lambda) \end{bmatrix} \tag{1.2}$$

refers to the nominal array manifold overlooking mutual coupling between the UCA dipoles, α refers to some electromagnetics factor independent of (ϕ,θ,λ), and $\mathbf{C}(\phi,\theta,\lambda)$ denotes a $M \times M$ "coupling matrix". The performance of the DOA estimation results show the serious degradation in their DOA estimation accuracy if the signal-processing algorithm overlooks mutual coupling by wrongly presuming $\mathbf{a}_{\mathrm{presumed}}(\phi,\theta,\lambda) = \mathbf{a}^{(\mathrm{UCA})}_{\mathrm{no-coupling}}(\phi,\theta,\lambda)$, instead of the correct $\mathbf{a}_{\mathrm{presumed}}(\phi,\theta,\lambda) = \mathbf{a}^{(\mathrm{UCA})}_{\mathrm{actual}}(\phi,\theta,\lambda)$.

Generally speaking, why would a signal-processing algorithm *not* use $\mathbf{a}_{\mathrm{presumed}}(\phi,\theta,\lambda) = \mathbf{a}^{(\mathrm{UCA})}_{\mathrm{actual}}(\phi,\theta,\lambda)$? It is primarily because $\mathbf{a}^{(\mathrm{UCA})}_{\mathrm{actual}}$ varies with the incident signal's frequency/wavelength (λ) and azimuth-elevation direction-of-arrival (ϕ,θ) through nested layers of multivariate integrals/summations, to render most signal-processing technique ineffectual.

This model-mismatch problem has long persisted in the antenna-array signal-processing literature, posing a critical bottle-neck for further advancement in this field. The above discussions have thus highlighted the need for simple mathematical expressions of $\mathbf{C}_{\mathrm{presumed}}(\lambda)$, even if considerable approximations are to be incurred.

A fresh approach is unquestionably needed to account for inter-antenna "mutual coupling", but with a "signal-processing-friendly" mathematical simplicity.

This thesis will avoid solving the Maxwell equations analytically, but will instead take a "behavioral" or "phenomenological" or "black box" approach, as is typical in modeling a propagation channel's fading statistics. That is,

much data of diverse cases of the "array manifold" are collected and are then numerically fit to parametric models of low degrees-of-freedom, without requiring any deep analysis of antenna physics. What emerges can be a refreshingly simple model, as will be demonstrated later in Sections 3.3, 4.3, and 5.3 for a UCA of dipole antennas oriented vertically or radially.

1.3 Intuitive Attempts in the Open Literature to Approximate Mutual Coupling (but Unsatisfactory)

How has the literature on antenna-array signal-processing dealt with inter-antenna "mutual coupling", short of calibrating the antenna array adaptively in the field?[1] Not a few parametric models have been proposed to model the coupling matrix, based on intuitive arguments on the electromagnetics involved. Yet, those models oversimplify and perform unsatisfactorily, as illustrated below.[2]

Take as example a uniform circular array of M number of antennas – all identical, all uniformly oriented in a circle with a radius R. If these M antennas were IMAGINED to suffer no mutual coupling among themselves, their inter-relationship would be encapsulated in the following $M \times 1$ array

[1]Even with array calibration, the present study would still be useful in supplying a parametric model to form a more realistic initial estimate of the mutual coupling to start off the calibration.

[2]Some antenna-array signal-processing algorithms do not *parametrically* model the coupling matrix. However, that suffers a shortcoming of leaving many unknown mutual impedance scalars to be estimated along with the direction(s)-of-arrival, for example, in direction finding. For example, an M-antenna array has $\frac{M(M+1)}{2}$ impedance (unknown) scalars, in addition to the 2 unknowns in azimuth-elevation direction-of-arrival. If $M = 10$, this would mean $55+2 = 57$ scalar unknowns instead of just 2 azimuth-elevation direction-of-arrival scalar unknowns.

manifold,

$$\mathbf{a}^{(\text{UCA})}_{\text{no}-\text{coupling}}(\phi,\theta,\lambda) \;:=\; \gamma \begin{bmatrix} e^{j\frac{2\pi}{\lambda}R\sin(\theta)\cos(\phi)} \\ e^{j\frac{2\pi}{\lambda}R\sin(\theta)\cos\left(\phi-\frac{2\pi}{M}\right)} \\ \vdots \\ e^{j\frac{2\pi}{\lambda}R\sin(\theta)\cos\left(\phi-\frac{2\pi(m-1)}{M}\right)} \end{bmatrix}, \tag{1.3}$$

where γ represents a factor common to all antennas in the array. The $e^{j\frac{2\pi}{\lambda}R\sin(\theta)\cos(\phi-\phi_m)}$, $\phi_m = \frac{2\pi(m-1)}{M}$, $\{m = 1, 2, ..., M\}$, factor is commonly labeled as the "spatial phase factor" of the incident signal, which here has a wavelength of λ and which impinges upon the dipoles at a direction-of-arrival of θ, and ϕ.

For the above UCA of identical antennas, an "intuitive" model of $\mathbf{C}(\lambda)$ common in a considerable body of signal-processing literature [22–24, 26, 29, 30, 43, 45, 46, 54–56, 69, 70, 74, 96–100, 100–106] is a circulant Toeplitz matrix: [3]

$$\mathbf{C}_{\text{intuitive}}(\lambda) \;:=\; \begin{bmatrix} c_0 & c_{n-1} & \dots & c_2 & c_1 \\ c_1 & c_0 & c_{n-1} & & c_2 \\ \vdots & c_1 & c_0 & \ddots & \vdots \\ c_{n-2} & & \ddots & \ddots & c_{n-1} \\ c_{n-1} & c_{n-2} & \dots & c_1 & c_0 \end{bmatrix}, \tag{1.4}$$

The "intuitive" justification in the literature:

{a} The electromagnetic coupling between the ℓth and the mth dipoles "should" (!) intuitively depend on only (and exponentially decreases with) the two dipoles' separation. This presumption gives the Toeplitz matrix structure.

[3] Many other mutual-coupling idealizations exist in the signal-processing literature, with some models more sophisticated than others. The model in (1.4) serves as an illustration here.

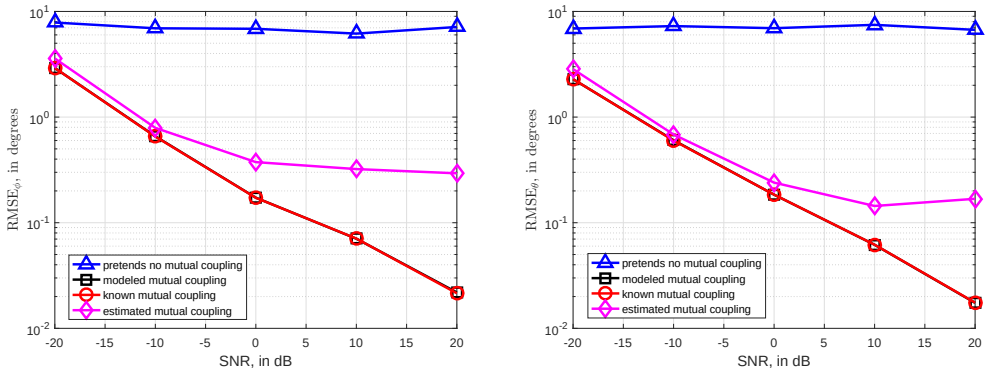

(a) (b)

Figure 1.4: RMSE versus SNR at $\frac{L}{\lambda} = 0.7$, $M = 10$, $\frac{R}{\lambda} = 5$, and $(\phi, \theta) = (30^0, 45^0)$: 180 snapshots, 100 Monte Carlo trials.

This "intuitive" model is presumed in many signal-processing algorithms (e.g., in [96, 97] for MIMO communications, in [98, 99] for beamforming, and in [23, 70, 76, 78, 100–106] for direction finding).

Is this "intuitive" model in (1.4), with all its algebraic elegance, valid? Unfortunately, our results in figure 1.4 suggest a resounding "no". The pink line with 'diamond' graph in the figure 1.4 is obtained by the blind estimate the mutual coupling matrix in (1.4) which is always worse than our phenomenological model's curve of black solid line with 'square'. [4]

Further several methods are available in literature, where the mutual impedance is used to explain the effects of the mutual coupling. One of the earliest methods is proposed by Gupta in [35], based on open-circuit method. In this method each antenna's terminal voltage is considered as an open-circuit voltage, which is calculated and related with all the antennas' voltages in an array and put them in an impedance matrix. This impedance matrix which consists of the impedances are used to depict the mutual cou-

[4] More simulation results are in appendix D.3

pling effects. This method is widely used because its concepts is directly related to the circuit theory. However, this method overlooks the scattering effects due to the nearby antennas' in an array [40]. In [40] the mutual impedance is calculated based on the receiving characteristics and considered the ignoring scattering effects of the Gupta's open-circuit method. Further modification is done in [27, 28, 49, 50] by considering all elements' scattering effects concurrently.

The transfer function based method of the mutual coupling effects are available in [20,30,45,69,75,76,82], Further a modified transformation method is also available in [50]. But these methods need an intuitive assumption of the mutual coupling matrix.

Furthermore, the self- and mutual impedances are varied by the type of antenna and its' configuration on an array. Due to the induced antenna nearby the surface current of an antenna in an array changes very much. So, it is a real problem to calculate the current distribution on the antenna's surface for computing the self- and mutual impedances. There are two popular methods, first the integral-equation moment method in [39, 42, 62, 63, 73] , and second, the induced electromotive force (EMF) method [25, 37, 38, 44] have tried to calculate that surface current distribution. Both methods are based on the integral forms of induced current and voltages at antenna terminals. However, these methods are found computationally extensive with integrals/summations problem.

The phenomenological approach for modeling the mutual coupling has already been used in [108, 109], but which is described for a pair of skewed dipoles.

Instead of

(i) affronting the full complexity of nested integrals/sums in each entry of

the $M \times M$ coupling matrix $\mathbf{C}(\lambda)$, or

(ii) making "intuitive" but "wild" guesses on the algebraic/mathematical structure of $\mathbf{C}_{\text{intuitive}}(\lambda)$ as in (1.4), or

(iii) ignoring all inter-antenna coupling altogether,

this thesis takes a different approach – a "phenomenological" or "behavioral" approach that takes mutual impedance data to fit them to a low-degrees-of-freedom (low-DoF) parametric manifold.

This "phenomenological" or "behavioral" method assume the coupling matrix prior, but "empirically" gathers numerous instances of this coupling matrix for various settings, then fits the dataset to different low-DoF models.

One cost-effective manner to collect vast datasets of the coupling matrix's numerical values is via computational electromagnetics simulations. For example, for wire antennas such as dipoles, the"method of moments" (MoM), a.k.a. the "boundary element method" (BEM), is known for its reliability to approximately solve the Maxwell equations for the unknown current distribution on wire antennas, thereby obtaining a dipoles array's mutual impedance matrix $\mathbf{Z}$; and such methods are realized in commercial software, like "EMCoS Antenna VLab"[5] among many others.

This somewhat brute-force approach of modeling might seem inelegant if viewed to some people as a "natural *philosophy*", but can be very effective as an *engineering* solution. This approach is widely used in the statistical modeling of wireless fading channels, of turbulent fluid flow, and many other phenomena of such complicated physics to be analytically intractable. The investigated case study in this thesis will demonstrate the power of this "phenomenological" or "behavioral" approach.

[5]URL: https://www.emcos.com

1.4 The Organization of this Thesis

The subsequent chapter describes the detail research methodology with theoretical frameworks in Chapter 2.

The new phenomenological models of the mutual coupling for vertical dipoles spaced uniformly on a horizontal circle with inter-dipole spacing more than 1.0 λ are described in Chapter 3.

In Chapter 4, the phenomenological models of the mutual coupling for vertical dipoles spaced uniformly on a horizontal circle with inter-dipole spacing less than 1.0 λ is described.

In Chapter 5, the phenomenological models of the mutual coupling among dipoles oriented radially on a horizontal circle are described.

The Chapter 6, concluded our research outcome with some observations and ended by the future investigation.

Chapter 2

The Phenomenological Modeling of the Mutual Coupling

In this thesis the"Phenomenological" modeling approach is used to model the mutual coupling by fitting the mutual coupling data (produced by finite-element simulations) to manually selected a model parameterized by few degrees-of-freedom, with the model-fitting leaving aside the intractable electromagnetic that produce the finite-element simulated data.

In the experimental investigation, the dipole is used as an antenna of a circular array, where dipoles are oriented vertically or radially and spaced uniformly on the circle's $x - y$ plane.

2.1 The Practical Significance of Electric Dipoles

The dipole antenna is simple in construction and widely used. The dipole antenna is constructed by two identical conductive elements (such as metal

wires or rods). It is inherently a balanced antenna, because it is bilaterally symmetrical. Figure 2.1 shows the feeding arrangement and geometry of a finite length dipole with length L.

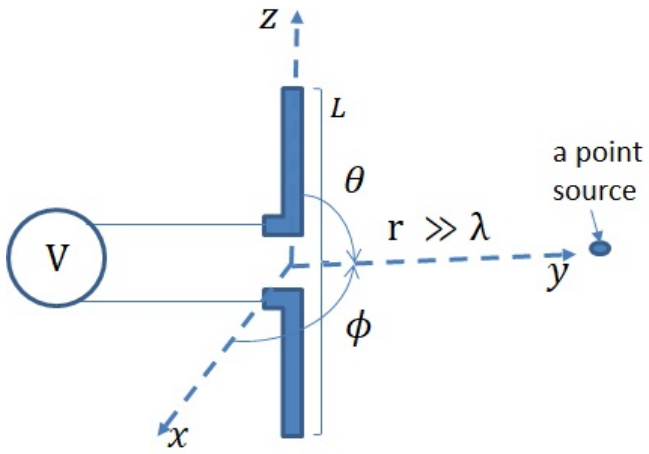

Figure 2.1: Feeding arrangment and geometry of a dipole.

The dipole's electric-field (E_θ) and magnetic (H_ϕ) pattern for a far field radiation ($r >> \lambda$) are of equations (4-62a) and (4-62b) in [11],

$$E_\theta = j\eta \frac{I_{max} e^{-j\omega_n r}}{2\pi r} \left[\frac{\cos\left(\frac{1}{2}\omega_n L \cos\theta\right) - \cos\left(\frac{1}{2}\omega_n L\right)}{\sin\theta} \right] \tag{2.1}$$

and

$$H_\phi = \frac{E_\theta}{\eta} \tag{2.2}$$

where η is the characteristic impedance (377 ohms in free space), I_{max} is the maximum current flow into the antenna, $\omega_n (:= \frac{2\pi}{\lambda})$ is the wave number and λ in [m] is the wavelength, r is the far-field distance, the azimuth angle ϕ, and elevation angle θ (here denotes the spatial angle with respect to the dipole axis). For a short dipole with a physical length of $\frac{\lambda}{50} < L < \frac{\lambda}{10}$, the

current along the dipole's length is in phase but its amplitude is approximately triangular. On a non-short dipole ($L > \frac{\lambda}{10}$), the current amplitude and phase are no longer constant. For a dipole with length $\frac{\lambda}{2}$, the current is still in phase and its amplitude can be approximated by a sinusoid.

The feedpoint impedance of a dipole antenna is very sensitive to the dipole's electrical length ($\frac{L}{\lambda}$). The infinitely thin half-wave dipole in free space has a center feed radiation resistance of 73.1 ohms.

At a dipole length of exactly half wave, the impedance is slightly inductive, but it drops rapidly to zero as the dipole length is foreshorten. At resonance, the dipole impedance is fully resistive. Below the resonance its impedance is capacitive. For a dipole's of an electrical length $\frac{L}{\lambda} < \frac{\lambda}{2}$, the radiation resistance decreases monotonically with length and is almost independent of diameter. In practice, a dipole has a finite length-to-diameter ratio. The dipole radiation pattern and impedance are influenced by the presence of nearby objects.

2.2 Dipole Effective Length

Suppose a signal imping on a dipole antenna of physical length L at a polar angle θ with an electric field E_{im} which transform into a voltage at the feeding point v_{oc} and vice versa, and the mathematical form is

$$v_{oc} = \mathbf{E}_{im} \cdot \boldsymbol{\ell}_{ef}, \tag{2.3}$$

where $\boldsymbol{\ell}_{ef}$ is the dipole's effective length and is defined as equation (2) of [65] and (3.2) on p. 19 of [19].

2.3 The Practical Significance of the Uniform Circular Array (UCA)

By placing M number of identical antennas uniformly on a circle (shown in figure 2.2), a uniform circular array (UCA) is obtained. This UCA has the advantage that its behavior is circularly symmetrical by a $\frac{2\pi}{M}$ radians rotation about the circle's origin. Specifically [20, 24–26, 29, 30, 100] investigated direction-of-arrival estimation using a UCA of dipoles oriented perpendicularly to the circle's plane.

In Figure 2.2 the M number of identical isotropic dipole antennas spaced uniformly (arranged counterclockwise from the positive x-axis) on the circumference of a circle of radius R, lying on the x-y Cartesian plane, and centered at the Cartesian origin. The plane wave incident on the origin by the elevation angle of θ, estimated clockwise on the positive z-axis, and the azimuth angle of ϕ, estimated counterclockwise on the positive x-axis.

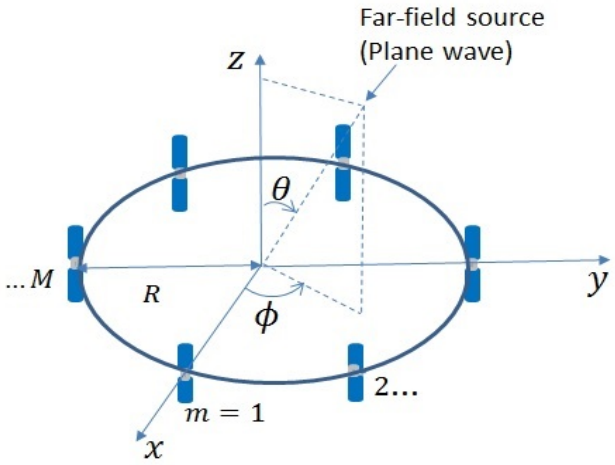

Figure 2.2: An array of M dipoles spaced uniformly on the rim of circle of radius R, on the x-y Cartesian plane and centered at the Cartesian origin.

The position of the m^{th} antenna for m=1, 2, ..., M can be represented by (x_m, y_m, z_m)=$\left(R\cos\left(\frac{2\pi(m-1)}{M}\right), R\sin\left(\frac{2\pi(m-1)}{M}\right), 0\right)$ and the angular distance between any two consecutive antennas is $\frac{2\pi R}{M}$.

Let $\boldsymbol{\chi}(t)$ is the center received signal at a time t. The observations at the array of antennas can thus be represented as (see equations (2.13)-(2.15) on page 29 of [10]),

$$\boldsymbol{\chi}(t, \boldsymbol{\varrho}_m) = \begin{bmatrix} \chi(t-\tau_1) \\ \chi(t-\tau_2) \\ \vdots \\ \chi(t-\tau_M) \end{bmatrix}, \tag{2.4}$$

where $\boldsymbol{\varrho}_m = [\boldsymbol{\varrho}_1, \boldsymbol{\varrho}_2, ..., \boldsymbol{\varrho}_M]^T$ is the position vector, M is the total number of antennas used, and

$$\tau_m = \frac{\mathbf{v}^T \boldsymbol{\varrho}_m}{c}, \tag{2.5}$$

is the time delay for the signal to reach the m^{th} sensor. In the above $c\,\{:= \lambda f\}$ denotes the medium propagation velocity and $\mathbf{v}$ denotes a unit vector which is presented as

$$\mathbf{v} = -\begin{bmatrix} u_x(\theta,\phi) \\ u_y(\theta,\phi) \\ u_z(\theta) \end{bmatrix} = -\begin{bmatrix} \sin(\theta)\cos(\phi), \\ \sin(\theta)\sin(\phi), \\ \cos(\theta) \end{bmatrix}, \tag{2.6}$$

where $u_x(\theta,\phi)$, $u_y(\theta,\phi)$, and $u_z(\theta)$ are direction cosines along the three axes, respectively. The negative sign arises due to the direction of the incident signal.

Then τ_m (of equation (2.5)) for $\boldsymbol{\varrho}_m = (x_m, y_m, z_m)$ is given by

$$\begin{aligned}\tau_m &= -\frac{R\sin(\theta)}{c}\left[\cos(\phi)\cos\left(\frac{2\pi(m-1)}{M}\right) + \sin(\phi)\sin\left(\frac{2\pi(m-1)}{M}\right)\right] \\ &= -\frac{R}{\lambda f}\sin(\theta)\cos\left(\phi - \frac{2\pi(m-1)}{M}\right)\end{aligned} \tag{2.7}$$

We apply the Fourier transform of $\boldsymbol{\chi}(t, \boldsymbol{\varrho}_m)$ and we can get the m^{th} element as

$$\begin{aligned}X_m(\omega) &= \int_{-\infty}^{\infty} e^{-j\omega t}\chi(t-\tau_m)dt = X(\omega)e^{-j\omega\tau_m} \\ &= X(\omega)e^{j\frac{2\pi}{\lambda}R\sin(\theta)\cos\left(\phi - \frac{2\pi(m-1)}{M}\right)}\end{aligned} \tag{2.8}$$

where $\omega\,\{:= 2\pi f\}$ denotes the angular frequency. Hence the observations in frequency domain can be written as

$$\mathbf{X}(\omega) = \begin{bmatrix} X_1(\omega) \\ X_2(\omega) \\ \vdots \\ X_M(\omega) \end{bmatrix} = X(\omega)\begin{bmatrix} e^{j\frac{2\pi}{\lambda}R\sin(\theta)\cos(\phi)} \\ e^{j\frac{2\pi}{\lambda}R\sin(\theta)\cos\left(\phi - \frac{2\pi}{M}\right)} \\ \vdots \\ e^{j\frac{2\pi}{\lambda}R\sin(\theta)\cos\left(\phi - \frac{2\pi(m-1)}{M}\right)} \end{bmatrix} \tag{2.9}$$

The array manifold vector can be expressed as

$$\mathbf{a}(\theta, \phi) = \begin{bmatrix} e^{j\frac{2\pi}{\lambda}R\sin(\theta)\cos(\phi)} \\ e^{j\frac{2\pi}{\lambda}R\sin(\theta)\cos\left(\phi - \frac{2\pi}{M}\right)} \\ \vdots \\ e^{j\frac{2\pi}{\lambda}R\sin(\theta)\cos\left(\phi - \frac{2\pi(m-1)}{M}\right)} \end{bmatrix} \tag{2.10}$$

The array manifold vector which contains essential information relating to the received signal since $X(\omega)$ is constant across the vector and hence can be ignored. The time difference between consecutive antennas is equivalent to the phase shift on the frequency domain.

2.4 Mutual Impedance

The impedance of an isolated antenna is the self-impedance [13], when the current I_2 on the antenna 2 is zero (see figure 2.3), the input impedance at antenna 1 as

$$Z_{11} = \frac{V_1}{I_1}|_{I_2=0}, \tag{2.11}$$

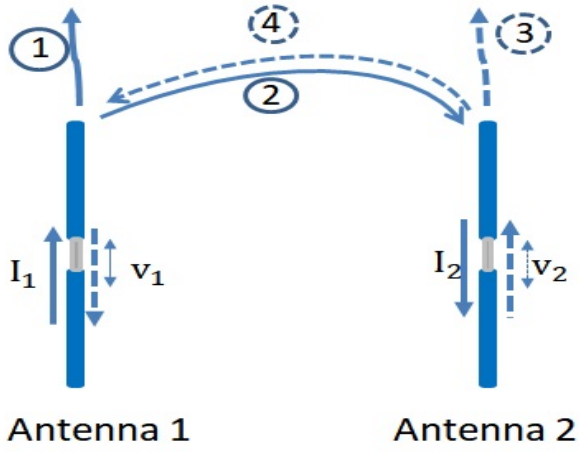

Figure 2.3: Reflected and radaited fields of an array elements.

where Z_{11} is the self-impedance. Further if antenna 1 is open circuit (i.e. $I_1 = 0$) (see figure 2.3), the mutual impedance at antenna 1 due to the current I_2 on the antenna 2 is

$$Z_{12} = \frac{V_1}{I_2}|_{I_1=0}, \tag{2.12}$$

where Z_{12} is the mutual impedance.

When the current I_1 on the antenna 1 is zero, then the input impedance at antenna 2 as

$$Z_{22} = \frac{V_2}{I_2}|_{I_1=0}, \tag{2.13}$$

where Z_{11} is the self-impedance. Further if antenna 2 is open circuit (i.e. $I_2 = 0$) (see figure 2.3), the mutual impedance at antenna 2 due to the current I_1 on the antenna 1 is

$$Z_{21} = \frac{V_2}{I_1}|_{I_2=0}, \tag{2.14}$$

where Z_{21} is the mutual impedance.

The voltage-current relations of this antenna system in figure 2.3 is

$$V_1 = Z_{11}I_1 + Z_{12}I_2, \tag{2.15}$$

$$V_2 = Z_{21}I_1 + Z_{22}I_2. \tag{2.16}$$

The impedances Z_{11} and Z_{22} are the self-impedances. The existence of an antenna nearby modifies the self-impedance (input impedance) and this modification influences by the type of antenna, the spacing between antennas, and the antenna's feeding characteristics [11].

The above equations (2.15) and (2.16) can be as

$$Z_{d1} = \frac{V_1}{I_1} = Z_{11} + Z_{12}\left(\frac{I_2}{I_1}\right) \tag{2.17}$$

$$Z_{d2} = \frac{V_1}{I_1} = Z_{22} + Z_{21}\left(\frac{I_1}{I_2}\right) \tag{2.18}$$

The impedances Z_{d1} and Z_{d2} are the driving-point impedances of antenna 1 and 2, respectively. For the antenna matching, this driving-point impedance is needed to match properly, but this driving point impedance depends on the mutual impedance and which is influenced by the current ratio $\frac{I_1}{I_2}$. Therefore, apparent that the mutual impedance has a significant role on the performance of an antenna and should be analyzed. Further, this analysis is usually quite complex and avoiding this complexity a simplified closed form phenomenological modeling approach is used in this thesis.

In a receive array, a plane wave, induces the current on antennas. The current induced on the antenna 2 radiates and received by the antenna 1, adding more antennas in an array causes more waves interaction. If there are M antennas, then there are M self-impedances and $M(M-1)$ mutual impedances. The mutual impedance between two elements in an array is found by dividing the open-circuit voltage at one antenna by the current on the other antenna as

$$Z_{mn} = \frac{V_m}{I_n}. \tag{2.19}$$

After calculating all the self- and mutual impedances, they are placed in the $M \times M$ impedance matrix.

A $M \times M$ impedance matrix is given below

$$\mathbf{Z} = \begin{bmatrix} Z_{11} & Z_{12} & \dots & Z_{1M} \\ Z_{21} & Z_{22} & \dots & Z_{2M} \\ \vdots & \vdots & \ddots & \vdots \\ Z_{M1} & Z_{M2} & \dots & Z_{MM} \end{bmatrix}, \tag{2.20}$$

where the diagonal terms represent the self-impedances and the off-diagonal terms denote the mutual impedances between the antennas.

2.5 Mutual Coupling

A coupling matrix is used to characterize the mutual coupling between the antenna elements at the port level. This matrix is calculated using scattering parameters (**S**-parameters) or impedance parameters (**Z**-parameters) and is used to decouple the array. To calculate the coupling matrix we have used the **S**-parameters matrix. The impedance matrix **Z** as in the equation (2.20) has a simple relation to the scattering parameters matrix as described in [15, 17]. The mathematical form of the mutual coupling characterized by the **S**−parameter is,[1] [2]

$$\mathbf{C} := \mathbf{S} = \left(\mathbf{Z}/z_L + \mathbf{I}\right)^{-1} \left(\mathbf{Z}/z_L - \mathbf{I}\right), \tag{2.21}$$

where **C** is the $M \times M$ coupling matrix, **Z** is the $M \times M$ impedance matrix, z_L is the dipole load impedance or characteristics impedance of the system, and **I** is the $M \times M$ identity matrix.

[1] The equation (2.21) of mutual coupling is derived from the conversion relationship of **Z**− parameters to **S**− parameters (please see the referecne [15] for details).

[2] For wave-guide fed antennas, it is more convenient to define the coupling between antennas in terms of scattering parameters instead of mutual impedances. Whereas the mutual impedance Z_{mn} relates the voltages and currents at the ports, the scattering parameters S_{mn} relates the voltage waves incident on the ports to those reflected from the ports [15].

2.6 The Phenomenological Models Obtained

Phenomenological expressions are proposed based on the following three perspectives:

(a) ($|Z|$) or ($\angle Z$), vs. $\{M, \frac{L}{\lambda}\}$ for a given $\frac{R}{\lambda}$,

(b) ($|Z|$) or ($\angle Z$), vs. $\{M, \frac{R}{\lambda}\}$ for a given $\frac{L}{\lambda}$,

(c) ($|Z|$) or ($\angle Z$), vs. $\{\frac{L}{\lambda}, \frac{R}{\lambda}\}$ for a given M.

By carefully observing the behavior of the plots in three perspectives, several models for each of the dependent variables

$|z_0| = |Z_{11}| = |Z_{22}|, \angle z_0 = \angle Z_{11} = \angle Z_{22}$,

$|z_m| = |Z_{12}| = |Z_{21}|$, and $\angle z_m = \angle Z_{12} = \angle Z_{21}$,

are proposed.

2.6.1 Expected Electromagnetical Trends in the Self-impedance z_0

1) All dipoles' self-impedances are equal.

2) $|z_0|$, $\Re\{z_0\}$, and $\Im\{z_0\}$ are each proportional to $\left(\frac{L}{\lambda}\right)^{-2}$ at small $\left(\frac{L}{\lambda}\right)$, i.e. for $\left(\frac{L}{\lambda}\right) \sim \frac{1}{4}$.

3) $|z_0|$, $\Re\{z_0\}$, and $\Im\{z_0\}$ increases slightly as the dipoles get closer to each other.

4) $\Im\{z_0\}$ would not change much w.r.t. M and w.r.t. R individually.

5) $|z_0|$ is minimum at $\left(\frac{L}{\lambda}\right) \sim \frac{1}{2}$,

   at resonance the electric filed (capacitor) and magnetic field (inductor) store same energy, leading to a purely real resistance so the magnitude of self-impedance is minimum near half-wave length of the dipole.

6) $\Im\{z_0\}$ goes through zero at $\left(\frac{L}{\lambda}\right) \sim \frac{1}{2}$.

2.6.2 Expected Electromagnetical Trends in the Mutual impedance z_m

a) At a small $\left(\frac{L}{\lambda}\right)$, and when neighboring dipoles are far apart (i.e. $\left(\frac{R}{\lambda}\right)$ large and/or M small) — z_m depends on $\{m, M, \left(\frac{R}{\lambda}\right)\}$ only through the inter-dipole spacing $\left(\frac{\Delta}{\lambda}\right)$.

b) $|z_m| \propto \left(\frac{L}{\lambda}\right)^2$, for small $\frac{L}{\lambda}$. i.e., for $\frac{L}{\lambda} \leq \frac{1}{4}$.

c) $z_m \propto e^{-(\alpha+j\beta)\frac{\Delta}{\lambda}}$. [3] This means that

c1) $|z_m| \propto e^{-\alpha\frac{\Delta}{\lambda}} = Ke^{-\alpha\frac{\Delta}{\lambda}} \Leftrightarrow \log|z_m| = \text{offset} - \alpha\frac{\Delta}{\lambda}$.

c2) $\angle z_m = \text{offset} - \beta\frac{\Delta}{\lambda}$, where $\beta > 0$.

In the above, α and β might vary w.r.t. $\frac{L}{\lambda}$.

2.6.3 Mathematical Model based on Electromagnetical Considerations

(A) For a fixed m and for a fixed M, but a variable $\frac{R}{\lambda}$:
$\frac{\Delta}{\lambda} \propto \left(\frac{R}{\lambda}\right)$
$\rightarrow \log|z_m| = \text{offset} - \alpha\frac{R}{\lambda}$.

(B) For a fixed $m = 1$ and for a fixed $\frac{R}{\lambda}$, but a variable M:
$\frac{\Delta}{\lambda} = \frac{R}{\lambda}\sin\left(\frac{\pi}{M}\right)$
$\rightarrow \log|z_m| = \text{offset} - \alpha\frac{R}{\lambda}\sin\left(\frac{\pi}{M}\right)$.

[3] The mutual impedance behaves roughly as a damped complex exponential with respect to dipole spacing, as the waves propagate out from one dipole to another in the near-field region.

(C) For a fixed M and for a fixed $\frac{R}{\lambda}$, but a variable m:

$\frac{\Delta}{\lambda} \;=\; \frac{R}{\lambda}\sin\left(m\frac{\pi}{M}\right)$

$\rightarrow \quad \log|z_m| \;=\; \text{offset } -\alpha\frac{R}{\lambda}\sin\left(m\frac{\pi}{M}\right).$

From (A)-(C):

$$\log|z_m| \;=\; \beta\left(\frac{L}{\lambda}\right) - \alpha\left(\frac{L}{\lambda}\right)\;\frac{R}{\lambda}\;\sin\left(\frac{m}{M}\pi\right). \tag{2.22}$$

and similarly,

$$\angle z_m \;=\; \alpha\left(\frac{L}{\lambda}\right) - \beta\left(\frac{L}{\lambda}\right)\;\frac{R}{\lambda}\;\sin\left(\frac{m}{M}\pi\right). \tag{2.23}$$

In the above $\alpha\left(\frac{L}{\lambda}\right)$ means that α depends on $\frac{L}{\lambda}$ similarly for $\beta\left(\frac{L}{\lambda}\right)$.

2.7 "Method of Moment" Electromagnetic Simulations of the Impedance Matrix

Consider a uniform circular array (UCA) of identical dipoles, spaced uniformly on a circle, but oriented perpendicular or radial to the circular plane. Their mutual impedance is approximated by numerical simulations, via the"method of moments" (MoM), a.k.a. the "boundary element method" (BEM), in order to solve the Maxwell equations. This "method of moments" is known for its reliability to solve for the unknown current distribution on wire antennas.[4] This is critical here, because *near*-field mutual coupling (as in this thesis investigation) is induced by a smooth current distribution on the dipoles and by rapid changes of the current distribution near the feed point, unlike *far*-zone radiation pattern evaluation. The specific software used here is the "EMCoS Antenna VLab". The "EMCoS Antenna VLab" simulations were conducted by simultaneously exciting each dipole with its own voltage source and while connecting each dipole to its own load.

The EMCoS VLab is a full-functional "method of moments" based 3-dimensional electromagnetic solver with CAD interface. The simulation parameters can be controlled and set through its graphical user interface (GUI) in the Geometry mode, the Model mode, and the Mesh mode stages.

[4]Please see the details of the MoM technique in the reference [16]

2.8 Research Methodology

In this section step by step phenomenological modeling method is described.

2.8.1 Geometry for the Phenomenological Modeling

This thesis has used the "Phenomenological" or "behavioral" method for modeling of the electromagnetic mutual impedance among dipoles placed uniformly on a circle as,

(A) the vertical dipoles spaced uniformly on a horizontal circle with inter-dipole spacing (i) more or (ii) less than 1.0 λ, is shown in the figure 2.4,

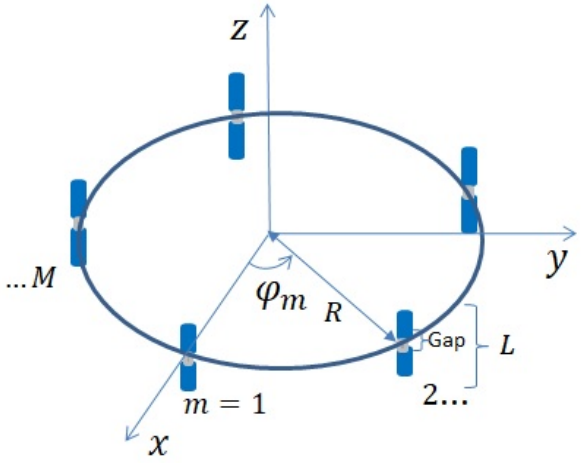

Figure 2.4: The spatial geometry of a circular array of $M = 5$ identical dipoles, spaced uniformly on a circle, but oriented perpendicular to the circular plane. Where $\varphi_m \left(= \frac{2\pi(m-1)}{M}\right)$ is the angular displacement of each dipole.

(B) dipoles are oriented radially on a horizontal circle with inter-dipole spacing less than 1.0 λ, is shown in the figure 2.5.

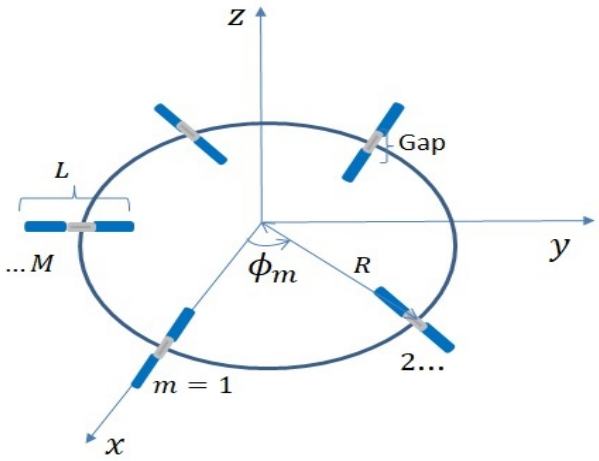

Figure 2.5: The spatial geometry of a circular array of $M = 5$ identical dipoles, spaced uniformly on a circle, but oriented radially to the circle's radius. Where $\phi_m \left(= \frac{2\pi(m-1)}{M}\right)$ is the angular displacement of each dipole.

2.8.2 Perform VLab Simulation for the Mutual Impedance Matrix

There are two stages in the VLab processing namely "pre-processing" and "post-processing". Three modes such as "Geometry Mode", "Model Mode", and "Mesh Mode" are belonged to the "pre-processing" stage.

In the "Geometry Mode" the uniform circular array of dipoles is constructed as shown in the figure 2.6 (the VLab screen-short view).

The physical parameters such as the dipole's structure, feed segment, size of each segment, and operating frequency are inserted in the "Model Mode" stage. The dipole feed segment's termination device is also created in this stage. The VLab view of the "Model Mode" is shown in the figure 2.7.

The discretization of the obtained model for calculation is done in the "Mesh Mode" step. According to the defined (in the "Model Mode" stage)

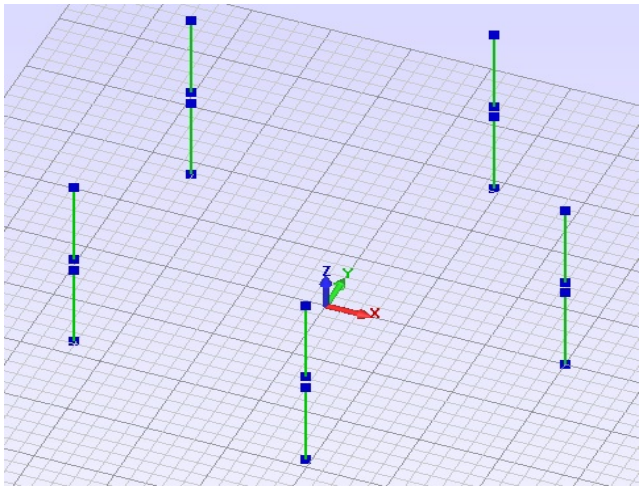

Figure 2.6: Geometry view of a circular array dipoles in VLab.

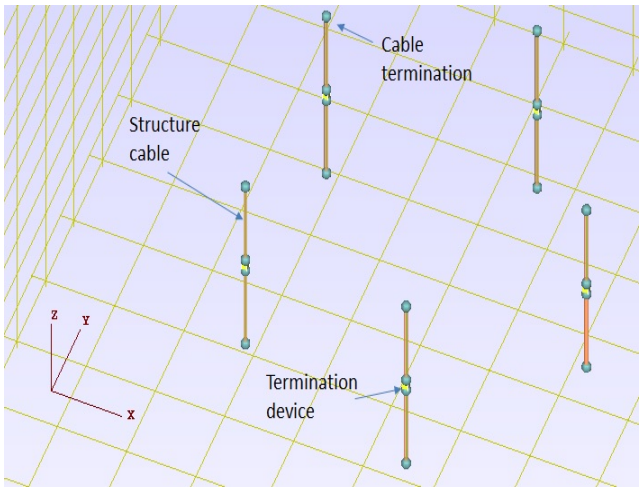

Figure 2.7: Model Mode view of a circular array dipoles in VLab.

segmentation sizes the wire segments are generated in this "Mesh Mode" period. For generating the output, a port is created in each dipole. The VLab view of the "Mesh Mode" is shown in the figure 2.8.

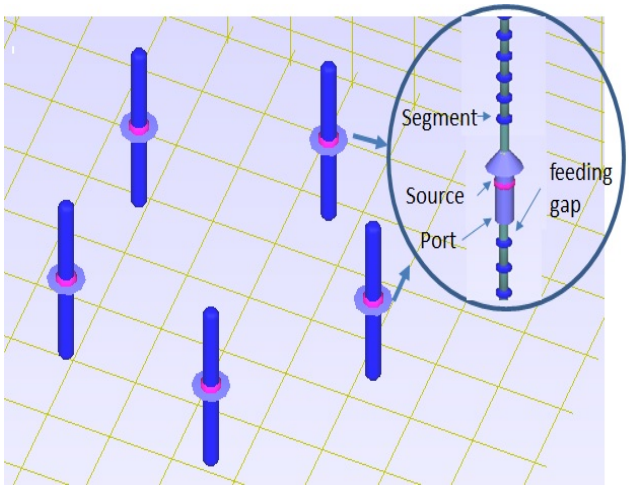

Figure 2.8: Mesh Mode view of a circular array dipoles in VLab.

Finally, the mutual impedance calculation is functioned in the "post-processing" stage and from where we can extract the data for our further analyze of modeling.

Parameters – for – VLab – Simulation :

This thesis has characterized the mutual coupling among M number of identical dipoles of length $\frac{L}{\lambda} \in \{0.1, 1.0\}$, how the $M \times M$ mutual impedance matrix's entries would vary with

1) the dipoles' normalized length ($\frac{L}{\lambda}$),

2) the number M of such dipoles in the circular array, and

3) the circle's radius ($\frac{R}{\lambda}$).

Due to the uniform circular array's rotational symmetry, this $M \times M$ mutual impedance matrix has only $\lfloor \frac{M+1}{2} \rfloor$ number of distinct entries.

In all VLab simulations, all electric dipoles have a core diameter of 0.02 millimeters, a feeding gap of $\frac{\lambda}{50}$, a wavelength-normalized length of $\frac{L}{\lambda} \in \{0.1 \sim 1.0\}$. There are 1000 segments over the length of each dipole. The array circle radius $\frac{R}{\lambda} \in \{0.3 \sim 20\}$. The number M of dipoles is $M \in \{5 \sim 10\}$. The student edition of "EMCoS Antenna VLab v1.0.1 SV" would run out of memory for a higher value for M.

From our VLab simulation output, we have got a circulant matrix of the mutual impedance, e.g., a 6×6 circulant matrix $\mathbf{Z}$ would take the mathematical form of

$$\mathbf{Z} = \begin{bmatrix} z_0 & z_1 & z_2 & z_3 & z_4 & z_5 \\ z_5 & z_0 & z_1 & z_2 & z_3 & z_4 \\ z_4 & z_5 & z_0 & z_1 & z_2 & z_3 \\ z_3 & z_4 & z_5 & z_0 & z_1 & z_2 \\ z_2 & z_3 & z_4 & z_5 & z_0 & z_1 \\ z_1 & z_2 & z_3 & z_4 & z_5 & z_0 \end{bmatrix}, \tag{2.24}$$

which has only M numbers of distinct entries, and where z_0 is the self-impedance, and the mutual impedance is $z_m, m = 1, 2, ..., (M-1)$. The VLab

simulations indicated that $z_1 = z_5$ and $z_2 = z_4$, always and exactly. These equalities are expected on account of geometric symmetry on the unit circle.

Moreover, due to the circular array's clockwise and counterclockwise symmetry, the $M \times M$ mutual impedance matrix would have only $\lceil \frac{M+1}{2} \rceil$ number of distinct entries, where $\lceil x \rceil$ refers to the smallest integer greater than or equal to x.

2.8.3 Model Fitting and Select the Best Model

For the model fitting, we have chosen $|z_0|, |z_m|, \angle z_0$, and $\angle z_m$, the magnitude ($|.|$) and phase ($\angle.$) of the self-and mutual impedance respectively, instead of $\mathrm{Re}\{z_0\}$, $\mathrm{Re}\{z_m\}$, $\mathrm{Im}\{z_0\}$, and $\mathrm{Im}\{z_m\}$. This is because $|z_0|, |z_m|$, $\mathrm{Re}\{z_m\}$, and $\mathrm{Im}\{z_m\}$ each takes on values over a large range. Hence to avoid overweighting of the large values, $\log|z_0|$, and $\log|z_m|$ will be fitted versus $\log \frac{L}{\lambda}$. However, $\mathrm{Re}\{z_0\}$ and $\mathrm{Re}\{z_m\}$ could go negative , rendering log(.) inapplicable, see in figure 2.9.

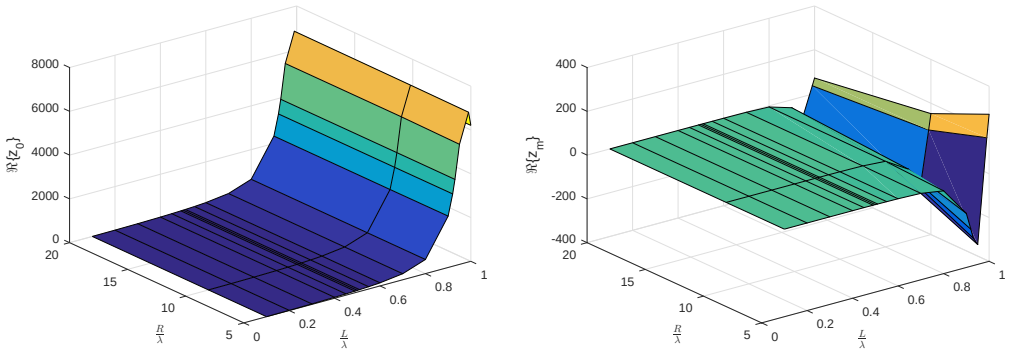

(a) (b)

Figure 2.9: VLab data of $\Re\{z_0\}$ and $\Re\{z_m\}$ versus $\frac{L}{\lambda}$ versus $\frac{R}{\lambda}$ for $M = 6$.

In the first stage of the model fitting we can define an objective function

as

$$SSE = \sum_{n=1}^{N} (z_n - \hat{z}_n)^2, \tag{2.25}$$

where the sum-of-squares error (SSE) denotes the closeness of the VLab data (the length of N is all combination of $M \times \frac{R}{\lambda} \times \frac{L}{\lambda}$ data length) of the impedance (z_n) and the model's predicted impedance ($\hat{z}_n$) values for the N number of observations.

Second, for finding the unknown coefficients of the predicted model we need to optimize the SSE error function by minimization as follows

$$\{\alpha_1, \alpha_2, ..., \alpha_p\} = \arg\min_{\alpha} \sum_{n=1}^{N} (z_n - \hat{z}_n)^2, \tag{2.26}$$

where $\{\alpha_1, \alpha_2, ..., \alpha_p\}$ are the unknown coefficients, and p represents the number of coefficients to be optimized.

Third, we have tested our model's the goodness-of-fit of by the number of coefficients (a.k.a. the number of degrees-of-freedom) and the value of R^2. The R^2 is computed as

$$R^2 = 1 - \frac{SSE}{SST}, \tag{2.27}$$

where the sum-of-squares total (SST) denotes the closeness of the data from the mean, symbolically,

$$SST = \sum_{n=1}^{N} (z_n - \bar{z})^2, \tag{2.28}$$

where the mean of the VLab data ($\bar{z}$) is

$$\bar{z} = \frac{1}{N} \sum_{n=1}^{N} z_n. \tag{2.29}$$

The range of R^2 value is between 0 and 1, the value closer to 1 indicating that a greater proportion of the variance is accounted for by the model. The higher the R^2, the better is the model fitting.

An MATLAB code is written for performing the four dimensional model fitting, i.e. $|z_0|, M, \frac{R}{\lambda}$, and $\frac{L}{\lambda}$, to produce the optimized coefficients and the corresponding R^2 value.

How to select the best − model − fit?

Finally, based on the highest R^2 value and with fewer numbers of the coefficients (a.k.a. degrees-of-freedom) the model has selected. The chosen model has returned the closest value of the VLab data and considerable with the existing electromagnetic theories and principles.

Chapter 3

UCA of Vertical Dipoles with Inter-dipole Spacing more than 1.0λ

A "phenomenological" or "behavioral" approach is used here to model the electromagnetic mutual impedance among dipoles placed uniformly on a circle, with the dipole axis perpendicular to the circular plane, where the inter-dipole spacing is 3.0λ to 20λ. This "phenomenological" or "behavioral" approach leads to a simple closed form for the mutual impedance matrix, explicitly in terms of the dipoles' electric length, the number of dipoles on the circle, and the circle's radius.

3.1 Introduction

In this chapter, we have considered a circular array shown in the figure 3.1, where the dipole's axis is parallel to the z-axis and spaced uniformly on the $x-y$ plane. The angular location of each dipole is

$$\varphi_m = 2\pi(m-1)/M, \tag{3.1}$$

where M is the number of dipoles in an array, $m = 1, 2, ..., M$,
and the inter-dipole spacing is

$$\Delta = 2R\sin(\pi/M), \tag{3.2}$$

where R is the radius of the circle.

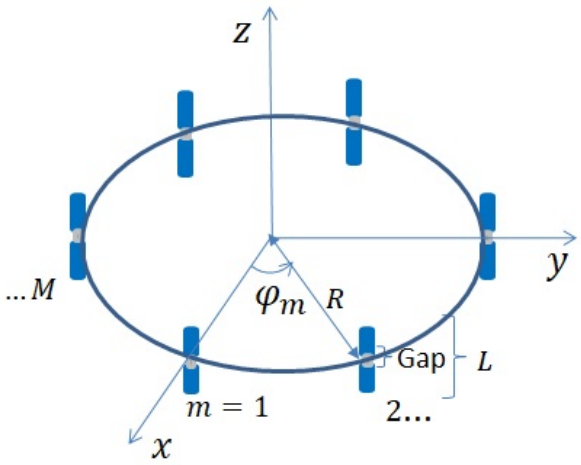

Figure 3.1: The spatial geometry of a circular array of $M = 6$ identical dipoles, spaced uniformly on a circle, but oriented perpendicular to the circular plane.

Such a uniform circular array (UCA) of dipoles oriented orthogonal to the circular plane – it has been used in [32, 33, 37–39, 42, 51, 53, 60, 66, 68].

3.2 Basic Consideration to Generate the Mutual Impedance Matrix

To obtain mathematically simple models of the mutual impedance matrix's $2\lceil\frac{M+1}{2}\rceil$ real-value scalars, this dissertation uses a "phenomenological" or "behavioral" approach as described in Chapter 2.

In this chapter, we have assumed for all subsequently presented results: each dipole's diameter is maintained at 0.02λ millimeters; each dipole's feeding gap equals $\frac{\lambda}{50}$; the voltage source's internal impedance is always matched to a half-wavelength dipole, regardless of the actual value of $\frac{L}{\lambda}$; there exist $1,000$ segments[1] over the length of each dipole. The following $3 \times 3 \times 18$ combinations of numerical settings are evaluated:

1) a radius of $R \in \{5, 10, 20\}\lambda$ for the circle,

2) $M \in \{6, 8, 10\}$ number of identical dipoles on the circle[2],

3) each dipole's electric length $\frac{L}{\lambda} \in \{0.1, 0.2, 0.3, 0.4, 0.45, 0.49, 0.5, 0.51, 0.55, 0.6, 0.7, 0.8, 0.9, 0.92, 0.93, 0.95, 0.99, 1.0\}$,

4) inter-dipole spacing is shown in the Table 3.1.

[1] In MoM analysis, currents of the antenna are divided by segments. The charge distribution on a wire has been accomplished by approximating the unknown with some basis functions, dividing the wire into segments, and then sequentially enforcing the unknown current at the center of each segment to form a set of linear equations. The antenna's radiation characteristics and feed point impedance are derived from the current distribution. [11]

[2] The student edition of EMCoS Antenna VLab V 1.0.1 SV would run out of memory for a higher value for M.

Table 3.1: Inter-dipole spacing in a UCA of large circle's radius

inter-dipole spacing, $\Delta = 2R\sin(\pi/M)$			
Radius	$M = 6$	$M = 8$	$M = 10$
R = 5 λ	5 λ	3.83 λ	3.09 λ
R = 10 λ	10 λ	7.65 λ	6.18 λ
R = 20 λ	20 λ	15.31 λ	12.36 λ

3.3 Phenomenological Model of the Entire Trivariate Dataset

[3]

3.3.1 Magnitude of the Self-impedance ($|z_0|$)

In an array all dipoles' self-impedance are equal and vary by a dipole's length. At a dipole length of exactly half-wave, the impedance is slightly inductive, but it drops rapidly to zero as the dipole length is foreshorten. At resonance, the dipole impedance is fully resistive. Below the resonance its impedance is capacitive. For a dipole's of an electrical length $\frac{L}{\lambda} < \frac{\lambda}{2}$, the radiation resistance decreases monotonically with length and is almost independent of diameter.

The "best" model [4] for the magnitude of the self-impedance for the entire trivariate dataset is found as

$$|z_0| \;\cong\; \exp\left\{\left|\alpha_1 + \frac{\alpha_2\left(1-\left(\frac{L}{\lambda}\right)^2\right)}{\alpha_3+\left(\frac{L}{\lambda}-\alpha_4\right)^2}\right|\right\}, \tag{3.3}$$

where

$\alpha_1 := 8.6288$,

$\alpha_2 := -0.1745$,

$\alpha_3 := 0.0333$,

$\alpha_4 := 0.5184$,

with $R^2 = 0.9678$.

[3] "Other candidate models are presented in appendix A.

[4] "Best" considering the fewness of coefficients.

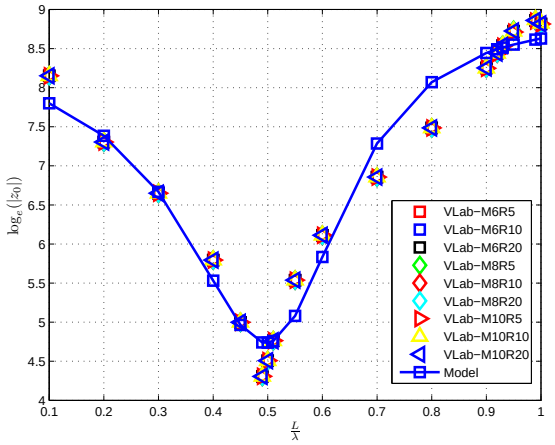

Figure 3.2: Magnitude of the self-impedance ($\log_e(|z_0|)$) versus $\frac{L}{\lambda} \in [0.1, 1.0]$ for $M = \{6, 8, 10\}$ and $\frac{R}{\lambda} = \{5, 10, 20\}$.

According to the R^2 value of 0.9678, this model can explain 96.78% of the variability in the VLab's data of the magnitude of the self-impedance.

The R^2 is evaluated of the equation (3.3) as

$$\log_e |z_0| \approxeq \left\{ \left| \alpha_1 + \frac{\alpha_2 \left(1 - \left(\frac{L}{\lambda}\right)^2\right)}{\alpha_3 + \left(\frac{L}{\lambda} - \alpha_4\right)^2} \right| \right\}. \tag{3.4}$$

Figure 3.2 shows the results of fitting (graphical view) of VLab data with least-squares fitted curve (Model). From the figure we can observe that when $\frac{L}{\lambda}$ becomes small, the dipole works like an open circuit with maximum impedance and decreasing by increasing $\frac{L}{\lambda}$ up to 0.5 after that again impedance increases before decreasing $\frac{L}{\lambda}$ near 1.0.

This trend is reasonable in view of electromagnetics, the magnitude of $|z_0|$ should go through a minimum at near $\frac{L}{\lambda} = 0.5$,

The partial derivation of equation (3.3) with respect to $\frac{L}{\lambda}$ is

$$\frac{d|z_0|}{d\frac{L}{\lambda}} = \exp\left\{\alpha_1 + \frac{\alpha_2\left(1-\left(\frac{L}{\lambda}\right)^2\right)}{\alpha_3+\left(\frac{L}{\lambda}-\alpha_4\right)^2}\right\}\cdot\left[\frac{d|z_0|}{d\frac{L}{\lambda}}\left\{\alpha_1 + \frac{\alpha_2\left(1-\left(\frac{L}{\lambda}\right)^2\right)}{\alpha_3+\left(\frac{L}{\lambda}-\alpha_4\right)^2}\right\}\right]$$

$$= \exp\left\{\alpha_1 + \frac{\alpha_2\left(1-\left(\frac{L}{\lambda}\right)^2\right)}{\alpha_3+\left(\frac{L}{\lambda}-\alpha_4\right)^2}\right\} \tag{3.5}$$

$$\cdot\left[\frac{\left\{\alpha_3+\left(\frac{L}{\lambda}-\alpha_4\right)^2\right\}\left\{-2\alpha_2\frac{L}{\lambda}\right\} - \alpha_2\left(1-\left(\frac{L}{\lambda}\right)^2\right)\left\{2(\frac{L}{\lambda}-\alpha_4)\right\}}{\left\{\alpha_3+\left(\frac{L}{\lambda}-\alpha_4\right)^2\right\}^2}\right],$$

Now setting the derivative to zero and the above equation (3.5) becomes

$$\left\{\alpha_3+\left(\frac{L}{\lambda}-\alpha_4\right)^2\right\}\left\{-2\alpha_2\frac{L}{\lambda}\right\} - \alpha_2\left\{1-\left(\frac{L}{\lambda}\right)^2\right\}\left\{2\left(\frac{L}{\lambda}-\alpha_4\right)\right\} = 0 \tag{3.6}$$

$$\{2\alpha_2\alpha_4\}\left(\frac{L}{\lambda}\right)^2 - 2\left\{\alpha_2\alpha_3+\alpha_2(\alpha_4)^2+\alpha_2\right\}\left(\frac{L}{\lambda}\right) + \{2\alpha_2\alpha_4\} = 0, \tag{3.7}$$

$$\frac{L}{\lambda} = \frac{\{\alpha_3+(\alpha_4)^2+1\} \pm \sqrt{\{\alpha_3+(\alpha_4)^2+1\}^2 - 4\alpha_4\alpha_4}}{2\alpha_4}. \tag{3.8}$$

By substituting all the coefficients value into equation (3.8), we find the $|z_0|$ is minimum at $\frac{L}{\lambda} \approx 0.4959$.

3.3.2 Phase of the Self-impedance ($\angle z_0$)

[5] [6]

The best model for the phase of the self-impedance is

$$\angle z_0 \quad \cong \quad \beta_1 \sin\left(2\pi \frac{L}{\lambda}\right), \tag{3.9}$$

where

$\beta_1 := -1.7343$,

with $R^2 = 0.8607$.

According to the R^2 value of 0.8607, our model can explain 86.07% of the VLab's data for the phase of the self-impedance. Figure 3.3 shows the results of fitting (graphical view) of VLab data with least-squares fitted curve (Model). From the figure we can observe that the changing of the phase is as like a simple 'sin' wave, and it goes to zero near the $\frac{L}{\lambda} \approx 0.5$.

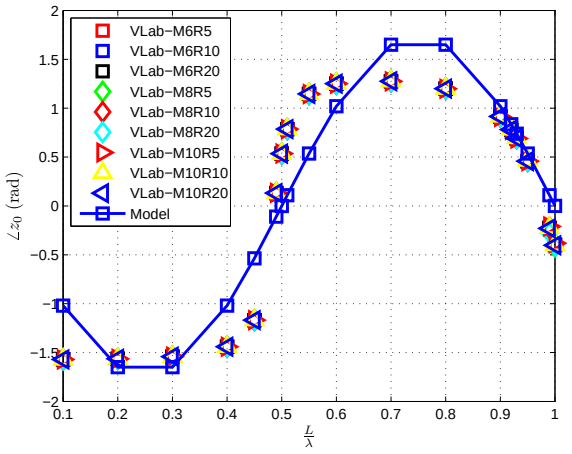

Figure 3.3: Phase of the self-impedance ($\angle z_0$) versus $\frac{L}{\lambda} \in [0.1, 1.0]$ for $M = \{6, 8, 10\}$ and $\frac{R}{\lambda} = \{5, 10, 20\}$.

[5] "best" in terms of fewness of parameters.

[6] "Other candidate models are presented in appendix A.

According to electromagnetics, the dipole's electric-field pattern is exactly $\sin\theta$, where θ denotes the spatial angle with respect to the dipole axis. Again, the dipoles go through a resonance at $\frac{L}{\lambda} \approx \frac{1}{2}$, and the phase behavior changes because the real part keeps rising while the imaginary part goes from negative to positive, then start to track the real part.

Further, the self-impedance is independent of M and of $\frac{R}{\lambda}$, as shown in the figures 3.2 and 3.3, and this independence is reasonable in terms of electromagnetics, because the inter-dipole spacing in here is larger even with the large value of M. Due to this the dipoles are significantly far apart relative to the size of their near fields. Thus, the self-impedance may no longer be dependent on the presence of the other dipoles.

3.3.3 Magnitude of the Mutual Impedance: $|z_m|,\ \forall m \in \{1, 2, \cdots, \lceil \frac{M-1}{2} \rceil\}$

The magnitude of the mutual impedance is modeled by varying the radius $\left(\frac{R}{\lambda}\right)$ and the number of elements (M) of the UCA for $\frac{L}{\lambda} = 0.1 \sim 1.0$.

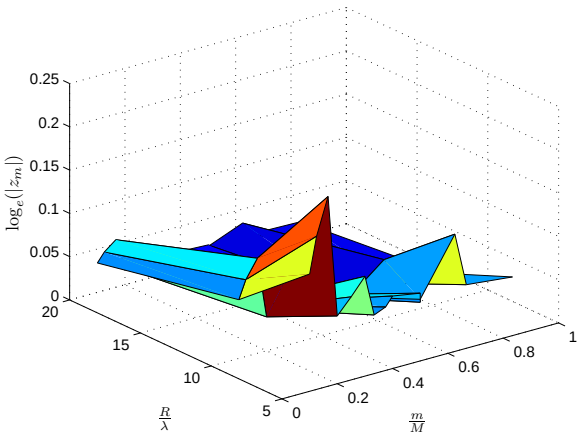

Figure 3.4: VLab data of the magnitude of the mutual impedance($\log_e(|z_m|)$) versus $\frac{R}{\lambda}$ and versus $\frac{m}{M}$ at $\frac{L}{\lambda} = 0.1$.

[7]

The proposed "best" phenomenological model for the magnitude of the mutual impedance is [8] [9]

$$|z_m| \ \cong \ \left\{ \gamma_1 \left(\frac{L}{\lambda}\right)^{\gamma_2} \left(\frac{\lambda}{R}\right) \left| \left(1 - \cos\left(2\pi \frac{m}{M}\right)\right)^{\gamma_3} \right\} \right|, \qquad (3.10)$$

where

$\gamma_1 := 1909.24$,

[7] The VLab data plots of $\frac{L}{\lambda} = 0.1 \sim 1.0$ are shown in appendix D.1

[8] "Best" considering the fewness of coefficients.

[9] "Other candidate models are presented in appendix A.

$\gamma_2 := 8.894,$

$\gamma_3 := -0.2798,$

with $R^2 = 0.8347.$

According to the R^2 value of 0.8347, our model can explain 83.47% of the variability in the VLab's data for the magnitude of the mutual impedance.

The R^2 is evaluated of the equation (3.10) as

$$\log_e |z_m| \approxeq \log_e \gamma_1 + \gamma_2 \log_e \left(\frac{L}{\lambda}\right) - \log_e \left(\frac{R}{\lambda}\right) + \gamma_3 \log_e \left|\left(1 - \cos\left(2\pi \frac{m}{M}\right)\right)\right| \quad (3.11)$$

The inversely proportional relationship between the magnitude $|z_m|$ of the mutual impedance and the radius of the circle $(\frac{R}{\lambda})$ in equation (3.10) suggests that the magnitude decreases monotonically with an increase inter-dipole separation by $\frac{R}{\lambda}$. Indeed as $\frac{R}{\lambda} \approx \infty$ the model gives $|z_m| \approx 0$.

This trend is reasonable in terms of electromagnetics because the induced electric fields among the neighboring dipoles are proportional and whose magnitude is inversely proportional to the distance between the emitting dipole and the induced dipole.

Further, the magnitude of the mutual impedance is directly proportional to the length of the dipole. In terms of electromagnetics this is obvious, because the emitted and the induced current depends on the surface area of the dipole and which is increased by increasing the length of the dipole.

The absolute part of the model equation (3.10) (as shown in figure 3.5) suggest that $|z_m|$ would increase as the number of dipoles M increase in an array (as the VLab data plots in the figure 3.6).

This is considerable in terms of electromagnetics, because the excited voltage and the induced voltage would increase as the number of antennas in an array increased as well as the mutual impedance increases.

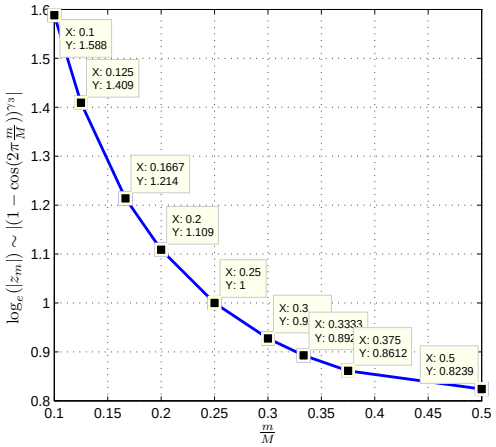

Figure 3.5: The absolute part of the model eq.(3.10) versus $\frac{m}{M}$, where $M = \{6, 8, 10\}$, and $m = 1, 2, 3$.

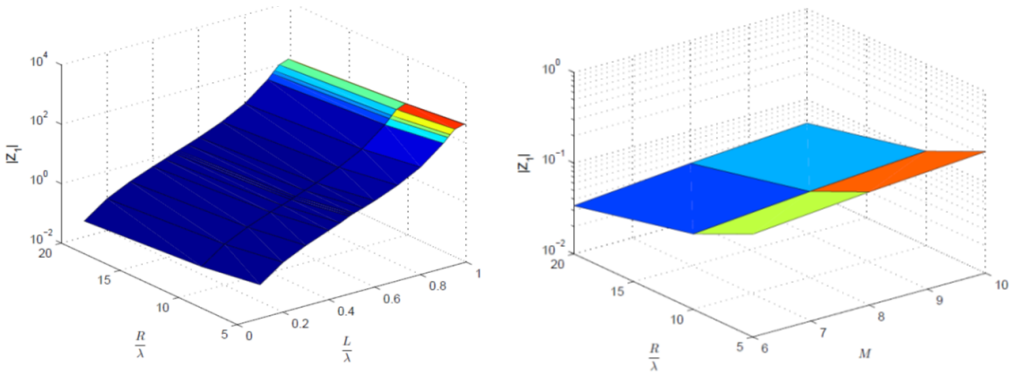

(a) (b)

Figure 3.6: VLab data of the magnitude of the mutual impedance (a) versus $\frac{L}{\lambda}$ versus $\frac{R}{\lambda}$, and (b) versus $\frac{R}{\lambda}$ versus M.

3.3.4 Phase of the Mutual Impedance: $\angle z_m,\ \forall m \in \{1, 2, \cdots, \lceil \frac{M-1}{2} \rceil\}$

The phase of the mutual impedance is modeled by varying the radius $\left(\frac{R}{\lambda}\right)$ and the number of elements (M) of the UCA for $\frac{L}{\lambda} = 0.1 \sim 1.0$.

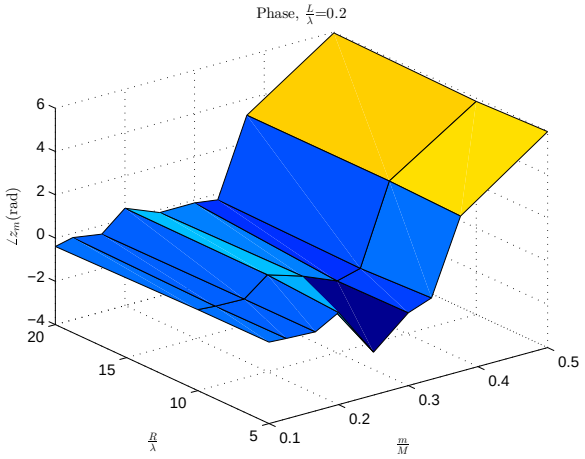

Figure 3.7: VLab data of the phase of the mutual impedance $(\angle z_m)$ versus $\frac{R}{\lambda}$ and versus $\frac{m}{M}$, at $\frac{L}{\lambda} = 0.2$, using MOD operator and $\pm 360°$.

The proposed "best" phenomenological model for the phase of the mutual impedance is

[10] [11]

$$\angle z_m \approx \left\{\delta_1 - \delta_2 \left(\frac{R}{\lambda}\right)^0 \sin\left(\delta_3 \left(\frac{m}{M}\right)\right)\right\} \left\{\frac{1 + \delta_4 \left(\frac{L}{\lambda}\right) + \delta_5 \left(\frac{L}{\lambda}\right)^2}{\delta_6 + \delta_7 \left(\frac{L}{\lambda}\right) + \left(\frac{L}{\lambda}\right)^2}\right\} \quad (3.12)$$

where

$\delta_1 := 2.3399,$

$\delta_2 := 3.1079,$

[10] "Best" considering the fewness of coefficients.

[11] "Other candidate models are presented in appendix A.

$\delta_3 := 7.2066,$

$\delta_4 := -2.5483,$

$\delta_5 := 1.6364,$

$\delta_6 := 0.6377,$

$\delta_7 := -1.5876,$

with $R^2 = 0.8230$.

According to the R^2 value of 0.8230, our model can explain 82.30% of the variability in the VLab's data for the phase of the mutual impedance.

The first part of our model equation (3.12) states that the phase of the mutual impedance is varying sinusoid, shown in the figure 3.8, and this is obvious in view of electromagnetics because the dipole's electric-field pattern is exactly sinusoid.

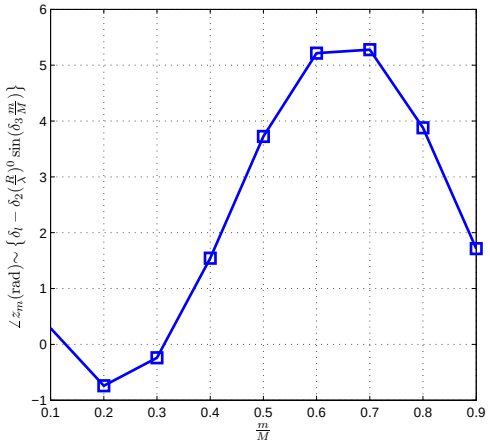

Figure 3.8: The first part of eq. (3.12) versus $\frac{m}{M}$, where $M = 10$, and $m = 1, 2, 3, ..., (M-1)$.

The fractional inside of the last part of our model equation (3.12) states that the phase of the mutual impedance is varying with the dipole's length as in the figure 3.9 (b), The trend of change of the phase with $\frac{L}{\lambda}$ is reasonable

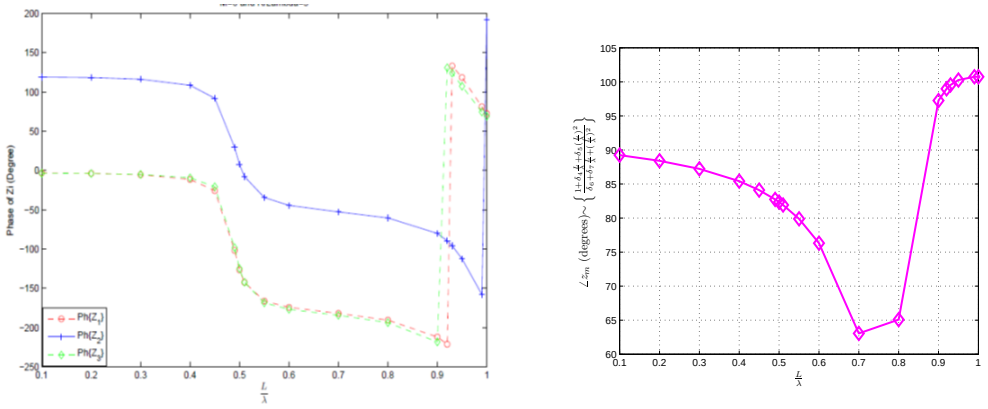

(a) (b)

Figure 3.9: VLab data of (a) the phase of the mutual impedance versus $\frac{L}{\lambda}$, and (b) the phase of the mutual impedance from model equation (3.12) versus $\frac{L}{\lambda}$.

in view of VLab data as shown in the figure 3.9 (a).

3.4 DOA Estimation

To show the utility of the proposed phenomenological mutual coupling model, the performance of the DOA estimation with the UCA of vertical dipoles is analyzed in this section.

3.4.1 Measurement Model

Suppose a pure tone signal $s(t) = \exp[j(\omega t + \psi)]$ impinge on a horizontal UCA of M vertical dipoles with the direction-of-arrival (DOA) of (θ, ϕ), where ψ is the initial phase, θ denotes the elevation angle measured from the positive z-axis, and ϕ denotes the azimuth angle measured from the positive x-axis as in figure 2.2. At the tth time instant the received signal model is

$$\mathbf{x}(t) \;=\; \mathbf{a}(\theta, \phi, \mathbf{C})\; s(t) + \mathbf{n}(t), \tag{3.13}$$

where $\mathbf{n}(t)$ denotes a $M \times 1$ the spatially white Gaussian thermal noise vector with zero mean and covariance $\sigma^2 \mathbf{I}_M$ and $\mathbf{C}$ is the $M \times M$ coupling matrix as in (2.21). Thus $\mathbf{x}(t) \sim \mathcal{N}(\boldsymbol{\mu}, \boldsymbol{\Sigma})$ where $\boldsymbol{\mu} = \mathbf{a}(\theta, \phi, \mathbf{C}) s(t)$ and $\boldsymbol{\Sigma} = \sigma^2 \mathbf{I}_M$. The UCA array manifold equals to (please see (2.10) for details)

$$\mathbf{a}(\theta, \phi, \mathbf{C}) \;=\; \mathbf{C} \begin{bmatrix} e^{j\frac{2\pi}{\lambda} R \sin(\theta)\cos(\phi)} \\ e^{j\frac{2\pi}{\lambda} R \sin(\theta)\cos\left(\phi - \frac{2\pi}{M}\right)} \\ \vdots \\ e^{j\frac{2\pi}{\lambda} R \sin(\theta)\cos\left(\phi - \frac{2\pi(M-1)}{M}\right)} \end{bmatrix}. \tag{3.14}$$

Collecting N discrete time samples of the received signal (3.13), i.e., $\mathbf{x}_n = \mathbf{x}(t_n)$ for $n = 1, 2, \ldots, N$, gives the observed data matrix

$$\mathbf{X} \;=\; \mathbf{a}(\theta, \phi, \mathbf{C})\; \mathbf{s} + \mathbf{N}, \tag{3.15}$$

where $\mathbf{X} \triangleq [\mathbf{x}_1, \mathbf{x}_2, \ldots, \mathbf{x}_N]$, $\mathbf{s} = [s(t_1), s(t_2), \ldots, s(t_N)]$, and $\mathbf{N}$ is the thermal noise matrix.

3.4.2 Maximum Likelihood Estimator

From equation (3.13), the joint probability density function for the multivariate Gaussian vector $\mathbf{x}(t)$ equals to

$$f\left(\mathbf{x}_n|(\theta,\phi,\mathbf{C})\right) = \frac{\exp\left\{-\frac{1}{2}\left(\mathbf{x}_n-\boldsymbol{\mu}\right)^H\boldsymbol{\Sigma}^{-1}\left(\mathbf{x}_n-\boldsymbol{\mu}\right)\right\}}{\left[(2\pi)^M\det(\boldsymbol{\Sigma})\right]^{\frac{1}{2}}} \tag{3.16}$$

With the N independent snapshots, the likelihood function can be expressed as

$$\begin{aligned} & f\left(\mathbf{x}_1,\mathbf{x}_2,...,\mathbf{x}_N|(\theta,\phi,\mathbf{C})\right) \\ = & \prod_{n=1}^{N} f\left(\mathbf{x}_n|(\theta,\phi,\mathbf{C})\right) \\ = & \frac{\prod_{n=1}^{N}\exp\left\{-\frac{1}{2}\left(\mathbf{x}_n-\boldsymbol{\mu}\right)^H\boldsymbol{\Sigma}^{-1}\left(\mathbf{x}_n-\boldsymbol{\mu}\right)\right\}}{\left[(2\pi)^M\det(\boldsymbol{\Sigma})\right]^{\frac{N}{2}}} \end{aligned} \tag{3.17}$$

The log-likelihood function equals to

$$\begin{aligned} \mathcal{L}(\theta,\phi,\mathbf{C}) = & \ln f\left(\mathbf{x}_1,\mathbf{x}_2,...,\mathbf{x}_N|(\theta,\phi)\right) \\ = & -\frac{1}{2}\sum_{n=1}^{N}\left\{\left(\mathbf{x}_n-\boldsymbol{\mu}\right)^H\boldsymbol{\Sigma}^{-1}\left(\mathbf{x}_n-\boldsymbol{\mu}\right)\right\} - \frac{N}{2}\ln\left[(2\pi)^M\det(\boldsymbol{\Sigma})\right] \end{aligned} \tag{3.18}$$

C is unknown

From (3.18), the maximum likelihood estimator (MLE) can be found as

$$(\hat{\theta},\hat{\phi},\hat{\mathbf{C}}) = \underset{\theta,\phi,\mathbf{C}}{\arg\max}\ \mathcal{L}(\theta,\phi,\mathbf{C}) \tag{3.19}$$

By noting that the second term in (3.18) is data independent, finding the MLE in (3.19) is equivalent to minimize the variance of the observed data as

$$\begin{aligned}(\hat{\theta},\hat{\phi},\hat{\mathbf{C}}) &= \underset{\theta,\phi,\mathbf{C}}{\arg\min}\sum_{n=1}^{N}\left\{(\mathbf{x}_n-\boldsymbol{\mu})^H\boldsymbol{\Sigma}^{-1}(\mathbf{x}_n-\boldsymbol{\mu})\right\}\\ &= \underset{\theta,\phi,\mathbf{C}}{\arg\min}\sum_{n=1}^{N}\left\{(\mathbf{x}_n-\boldsymbol{\mu})^H(\mathbf{x}_n-\boldsymbol{\mu})\right\},\end{aligned} \tag{3.20}$$

where the second equality holds because $\boldsymbol{\Sigma}=\sigma^2\mathbf{I}_M$.

In the optimization (3.20), $4+2\lfloor\frac{M}{2}\rfloor$ real variables (θ, ϕ, $\Re\{z_0\}$, $\Im\{z_0\}$, ..., $\Re\{z_{\lfloor\frac{M}{2}\rfloor}\}$, $\Im\{z_{\lfloor\frac{M}{2}\rfloor}\}$) are simultaneously searched. As a UCA with M vertical dipoles takes $2M$ real measurements, (3.20) works under the condition of $2M\geq 4+2\lfloor\frac{M}{2}\rfloor$, or equivalently $M\geq 3$.

C is known or modeled

When $\mathbf{C}$ is priorly known or calculated using the proposed phenomenological model of $\mathbf{Z}$, the maximum likelihood estimator can be similarly found as

$$(\hat{\theta},\hat{\phi}) = \underset{\theta,\phi}{\arg\min}\sum_{n=1}^{N}\left\{(\mathbf{x}_n-\boldsymbol{\mu})^H(\mathbf{x}_n-\boldsymbol{\mu})\right\}, \tag{3.21}$$

3.4.3 Monte Carlo Simulations

Three cases are shown by assuming the estimation algorithm

(i) knows the exact mutual coupling matrix in $\mathbf{C}$ =VLab data in (2.21);

(ii) pretends there's no mutual coupling such that $\mathbf{C}$ is a scaled identity matrix, and estimates the DOA using equation (3.21);

(iii) assumes the proposed phenomenological model of the mutual coupling matrix, and estimates the DOA using equation (3.21);

To have a fair comparison with the same level of SNR, in each of the above cases the mutual coupling matrix is normalized by its Frobenius norm.

3.4.4 Monte Carlo Simulation Plots

Monte Carlo simulations using eq. (3.3), eq. (3.9), eq.(3.10), and eq. (3.12) of $|z_0|$, $\angle z_0$, $|z_m|$, and $\angle z_m$ respectively.

The DOA estimation plots in the figures 3.10 $\sim$ 3.21 show the estimation root-mean-square error (RMSE)[12] of $\hat{\phi}$ and $\hat{\theta}$, versus SNR in dB. Each icon in figures represents 1000 independent Monte-Carlo trails.

These figures verify the usefulness of the proposed phenomenological models- that these models offer estimation precisions almost as good as if the exact impedance were known, whereas ignoring mutual coupling causes a degradation that can be several orders of magnitude.

[12]Expression in appendix D.2

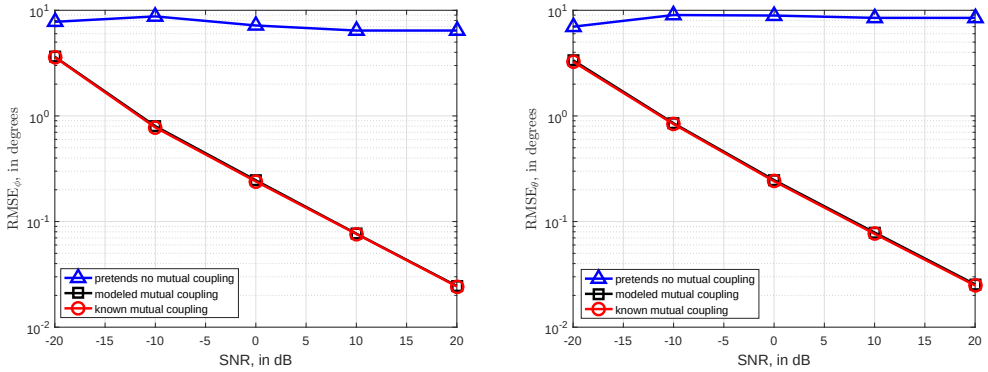

Figure 3.10: RMSE versus SNR at $\frac{L}{\lambda} = 0.45$, $M = 6$, $\frac{R}{\lambda} = 5$, and $(\phi, \theta) = (30^0, 45^0)$: 180 sanpshots, 1000 Monte Carlo trials.

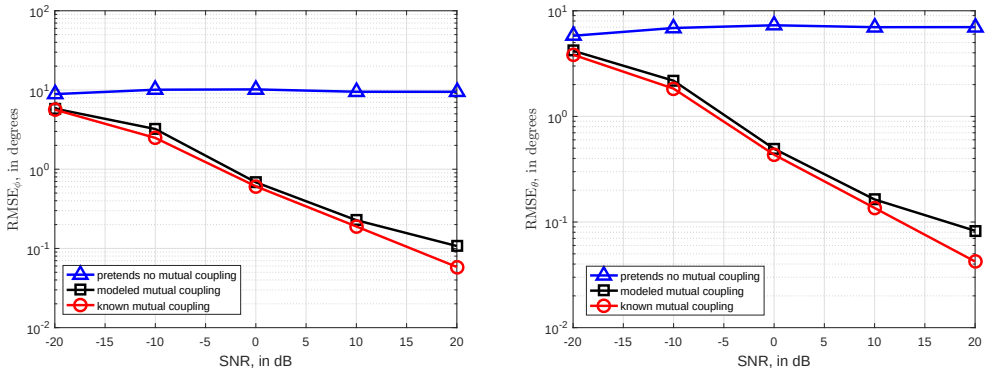

Figure 3.11: RMSE versus SNR at $\frac{L}{\lambda} = 0.5$, $M = 6$, $\frac{R}{\lambda} = 5$, and $(\phi, \theta) = (36^0, 36^0)$: 180 sanpshots, 1000 Monte Carlo trials.

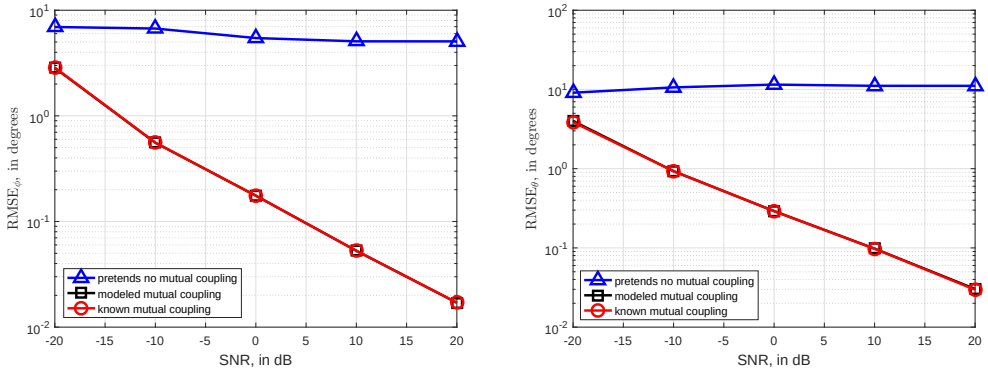

Figure 3.12: RMSE versus SNR at $\frac{L}{\lambda} = 0.6$, $M = 6$, $\frac{R}{\lambda} = 5$, and $(\phi, \theta) = (30^0, 60^0)$: 180 sanpshots, 1000 Monte Carlo trials

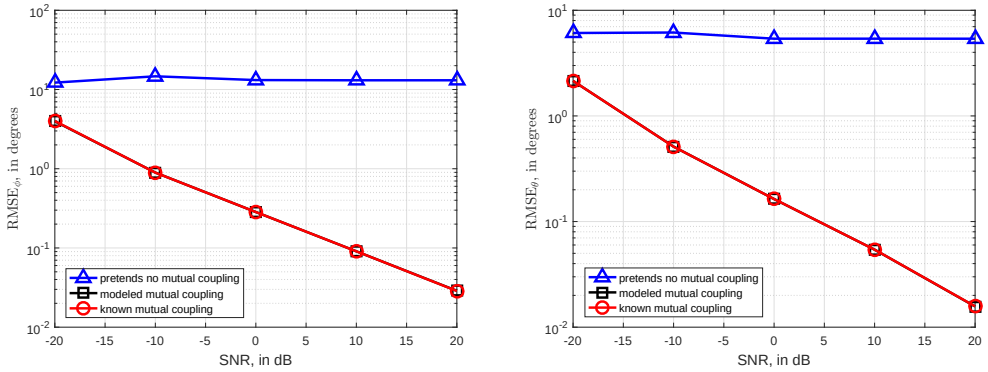

Figure 3.13: RMSE versus SNR at $\frac{L}{\lambda} = 0.7$, $M = 6$, $\frac{R}{\lambda} = 5$, and $(\phi,\ \theta) = (45^0, 30^0)$: 180 sanpshots, 1000 Monte Carlo trials.

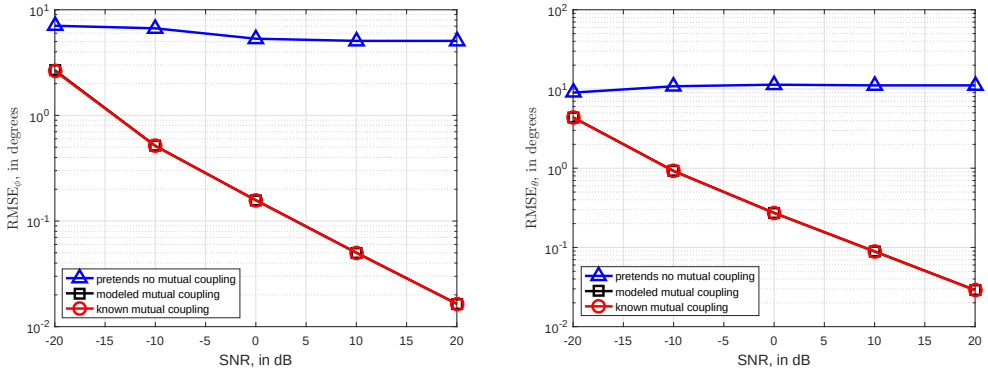

Figure 3.14: RMSE versus SNR at $\frac{L}{\lambda} = 0.8$, $M = 6$, $\frac{R}{\lambda} = 5$, and $(\phi,\ \theta) = (45^0, 30^0)$: 180 sanpshots, 1000 Monte Carlo trials.

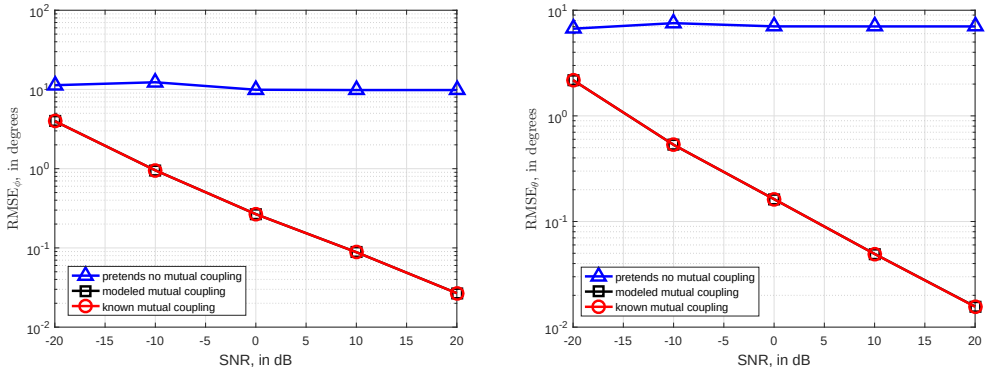

Figure 3.15: RMSE versus SNR at $\frac{L}{\lambda} = 0.9$, $M = 6$, $\frac{R}{\lambda} = 5$, and $(\phi,\ \theta) = (30^0, 30^0)$: 180 sanpshots, 1000 Monte Carlo trials

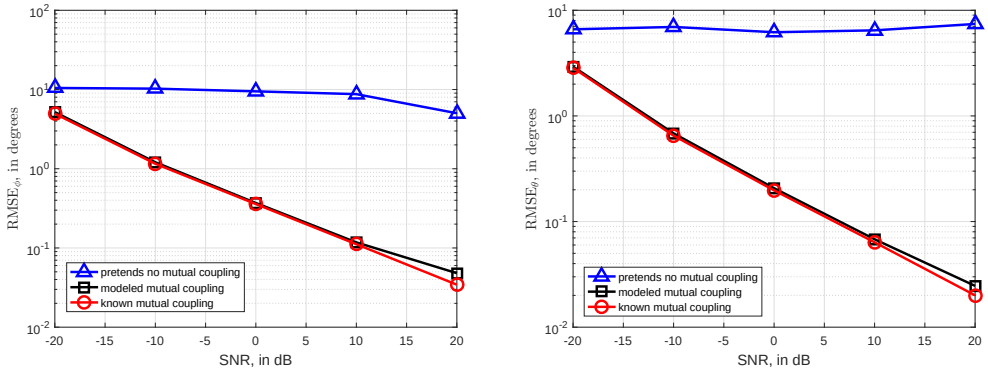

Figure 3.16: RMSE versus SNR at $\frac{L}{\lambda} = 0.45$, $M = 8$, $\frac{R}{\lambda} = 5$, and $(\phi, \theta) = (30^0, 30^0)$: 180 sanpshots, 1000 Monte Carlo trials.

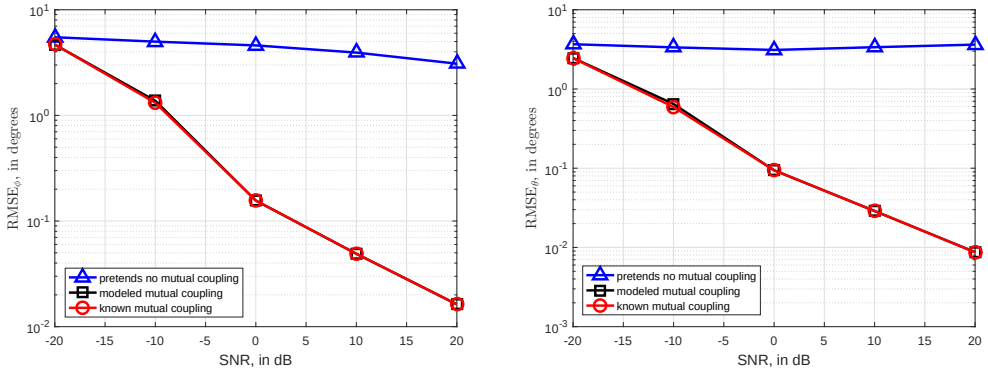

Figure 3.17: RMSE versus SNR at $\frac{L}{\lambda} = 0.55$, $M = 8$, $\frac{R}{\lambda} = 10$, and $(\phi, \theta) = (30^0, 45^0)$: 180 sanpshots, 1000 Monte Carlo trials

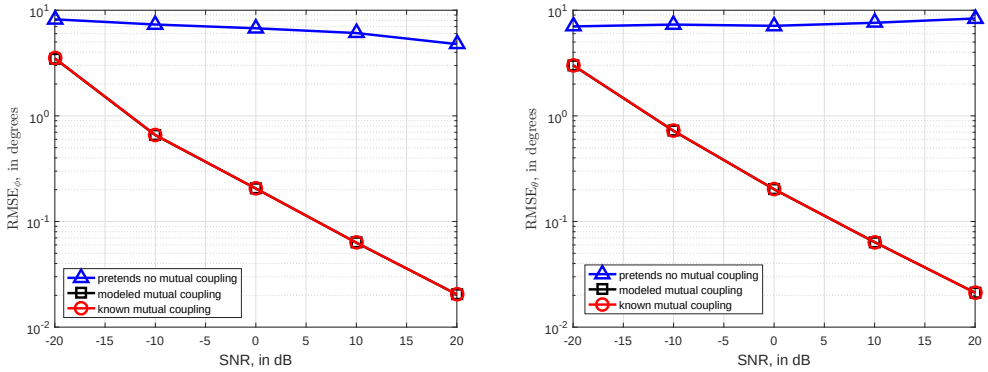

Figure 3.18: RMSE versus SNR at $\frac{L}{\lambda} = 0.6$, $M = 8$, $\frac{R}{\lambda} = 5$, and $(\phi, \theta) = (45^0, 45^0)$: 180 sanpshots, 1000 Monte Carlo trials.

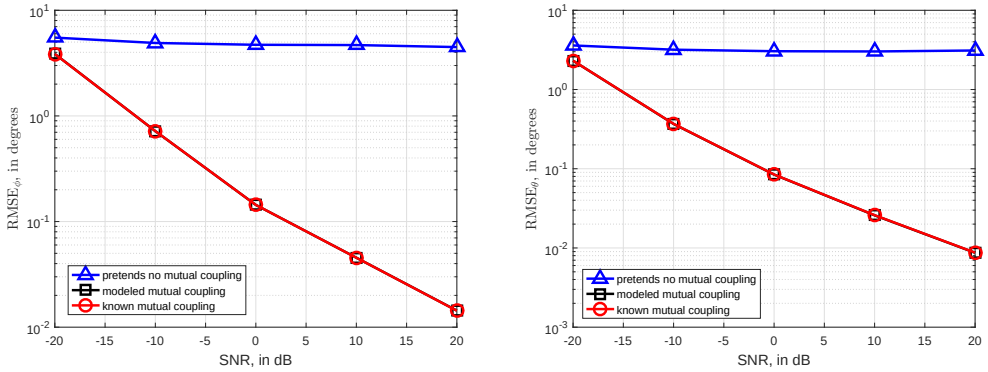

Figure 3.19: RMSE versus SNR at $\frac{L}{\lambda} = 0.6$, $M = 10$, $\frac{R}{\lambda} = 10$, and $(\phi, \theta) = (30^0, 30^0)$: 180 sanpshots, 1000 Monte Carlo trials.

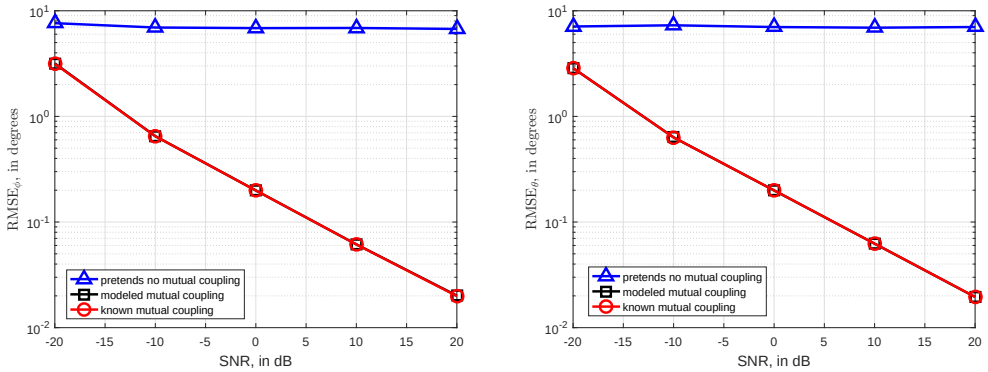

Figure 3.20: RMSE versus SNR at $\frac{L}{\lambda} = 0.7$, $M = 10$, $\frac{R}{\lambda} = 5$, and $(\phi, \theta) = (30^0, 45^0)$: 180 sanpshots, 1000 Monte Carlo trials

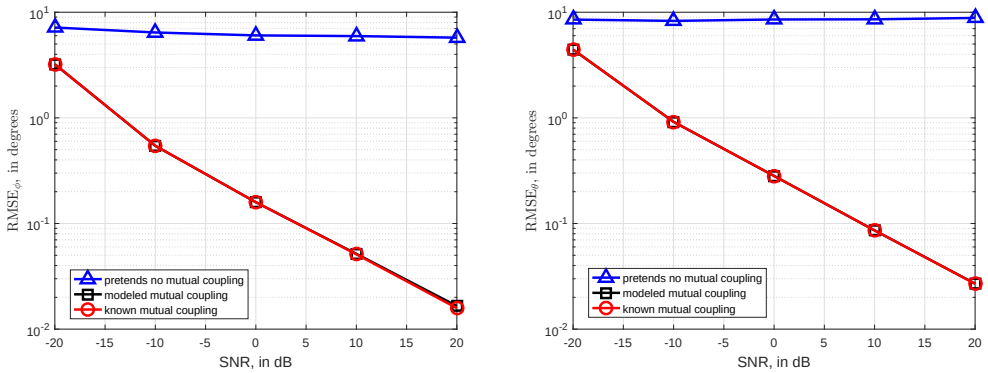

Figure 3.21: RMSE versus SNR at $\frac{L}{\lambda} = 0.8$, $M = 10$, $\frac{R}{\lambda} = 5$, and $(\phi, \theta) = (45^0, 60^0)$: 180 sanpshots, 1000 Monte Carlo trials.

3.5 Summary

The proposed phenomenological models for the magnitude and the phase of the self-and mutual impedance for the UCA of vertical dipoles with inter-dipole spacing more than 1λ are summarized in the Table 3.2.

Table 3.2: The best phenomenological models for a UCA of vertical dipoles

Inter-dipole spacing of vertically oriented dipoles, more than 1λ.	
Impedance	Models
$\lvert z_0\rvert$	$\lvert z_0\rvert \approxeq \exp\left\{\left\lvert \alpha_1 + \frac{\alpha_2\left(1-\left(\frac{L}{\lambda}\right)^2\right)}{\alpha_3+\left(\frac{L}{\lambda}-\alpha_4\right)^2}\right\rvert\right\}$, where $\alpha_1 := 8.6288, \alpha_2 := -0.1745, \alpha_3 := 0.0333, \alpha_4 := 0.5184$.
$\angle z_0$	$\angle z_0 \approxeq \beta_1 \sin\left(2\pi\frac{L}{\lambda}\right)$, where $\beta_1 := -1.7343$.
$\lvert z_m\rvert$	$\lvert z_m\rvert \approxeq \left\{\gamma_1\left(\frac{L}{\lambda}\right)^{\gamma_2}\left(\frac{\lambda}{R}\right)\left(1-\cos\left(2\pi\frac{m}{M}\right)\right)^{\gamma_3}\right\}$, where $\gamma_1 := 1909.24, \gamma_2 := 8.894, \gamma_3 := -0.2798$.
$\angle z_m$	$\angle z_m \approxeq \left\{\delta_1 - \delta_2\left(\frac{R}{\lambda}\right)^0 \sin\left(\delta_3\left(\frac{m}{M}\right)\right)\right\}\left\{\frac{1+\delta_4\left(\frac{L}{\lambda}\right)+\delta_5\left(\frac{L}{\lambda}\right)^2}{\delta_6+\delta_7\left(\frac{L}{\lambda}\right)+\left(\frac{L}{\lambda}\right)^2}\right\}$, where $\delta_1 := 2.3399, \delta_2 := 3.1079, \delta_3 := 7.2066, \delta_4 := -2.5483, \delta_5 := 1.6364, \delta_6 := 0.6377, \delta_7 := -1.5876$.

Chapter 4

UCA of Vertical Dipoles with Inter-dipole Spacing less than 1.0λ

A "phenomenological" or "behavioral" approach is used here to model the electromagnetic mutual impedance among dipoles placed uniformly on a circle, with the dipole axis perpendicular to the circular plane, where the inter-dipoles spacing vary from 0.2 λ to 1.0 λ.

4.1 Introduction

In this chapter, we have considered a circular array shown in the figure 4.1, where the dipole's axis is parallel to the z-axis and spaced uniformly on the $x-y$ plane. The angular location of each dipole is

$$\varphi_m = 2\pi(m-1)/M, \tag{4.1}$$

where M is the number of dipoles in an array, $m = 1, 2, ..., M$,

and the inter-dipole spacing is

$$\Delta = 2R\sin(\pi/M), \tag{4.2}$$

where R is the radius of the circle.

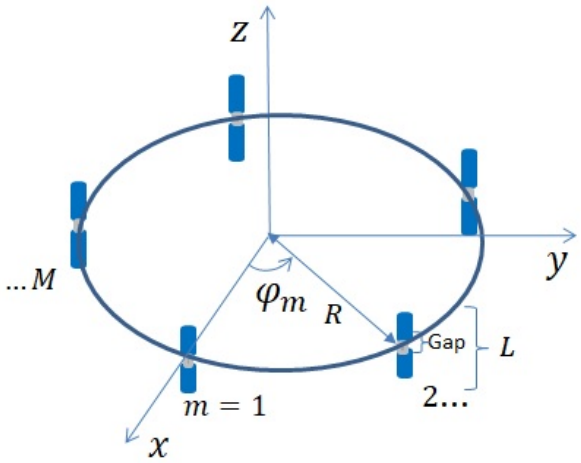

Figure 4.1: The spatial geometry of a circular array of $M = 5$ identical dipoles, spaced uniformly on a circle, but oriented perpendicular to the circular plane.

Such a uniform circular array (UCA) of dipoles oriented orthogonal to the circular plane – it has been used in [32, 33, 37–39, 42, 51, 53, 60, 66, 68].

4.2 Basic Consideration to Generate the Mutual Impedance Matrix

To obtain mathematically simple models of the mutual impedance matrix's $2\lceil\frac{M+1}{2}\rceil$ real-value scalars, this dissertation uses a "phenomenological" or

"behavioral" approach as described in the chapter 2.

In this chapter, we have assumed for all subsequently presented results: each dipole's diameter is maintained at 0.02λ millimeters; each dipole's feeding gap equals $\frac{\lambda}{50}$; the voltage source's internal impedance is always matched to a half-wavelength dipole, regardless of the actual value of $\frac{L}{\lambda}$; there exist $1,000$ segments over the length of each dipole. The following $3 \times 3 \times 12$ combinations of numerical settings will be evaluated:

1) a radius of $R \in \{0.3, 0.6, 1.0\}\lambda$ for the circle,

2) $M \in \{5, 7, 9\}$ number of identical dipoles on the circle[1],

3) each dipole's electric length $\frac{L}{\lambda} \in \{0.1, 0.2, 0.3, 0.4, 0.45,$
$0.5, 0.55, 0.6, 0.7, 0.8, 0.9, 1.0\}$,

4) inter-dipole spacing is shown in the Table 4.1.

Table 4.1: Inter-dipole spacing in a UCA of vertically oriented dipoles

inter-dipole spacing, $\Delta = 2R\sin(\pi/M)$			
Radius	$M = 5$	$M = 7$	$M = 9$
R = 0.3 λ	0.35 λ	0.26 λ	0.2 λ
R = 0.6 λ	0.7 λ	0.52 λ	0.41 λ
R = 1.0 λ	1.17 λ	0.86 λ	0.68 λ

[1]The student edition of EMCoS Antenna VLab V 1.0.1 SV would run out of memory for a higher value for M.

4.3 Phenomenological Model of the Entire Trivariate Dataset

[2]

4.3.1 Magnitude of the Self-impedance ($|z_0|$)

The "best" model [3] for the magnitude of the self-impedance for the entire trivariate dataset is found as

$$|z_0| \;\cong\; \exp\left\{\left|\alpha_1 + \frac{\alpha_2\left(1-\left(\frac{L}{\lambda}\right)^2\right)}{\alpha_3+\left(\frac{L}{\lambda}-\alpha_4\right)^2}\right|\right\}, \tag{4.3}$$

at

$\alpha_1 := 8.3302$,

$\alpha_2 := -0.1375$,

$\alpha_3 := 0.0294$,

$\alpha_4 := 0.5173$,

with $R^2 = 0.9232$.

According to the R^2 value of 0.9232, our model can explain 92.32% of the VLab's data variability for the magnitude of the self-impedance.

The R^2 is evaluated of the equation (4.3) as

$$\log_e|z_0| \cong \left\{\left|\alpha_1 + \frac{\alpha_2\left(1-\left(\frac{L}{\lambda}\right)^2\right)}{\alpha_3+\left(\frac{L}{\lambda}-\alpha_4\right)^2}\right|\right\}. \tag{4.4}$$

[2] "Other candidate models are presented in appendix B.

[3] "Best" considering the fewness of coefficients.

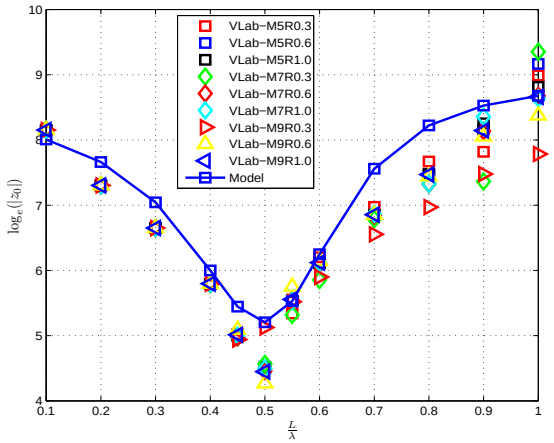

Figure 4.2: Magnitude of the self-impedance ($\log_e(|z_0|)$) versus $\frac{L}{\lambda} \in [0.1, 1.0]$ for $M = \{5, 7, 9\}$ and $\frac{R}{\lambda} = \{0.3, 0.6, 1.0\}$.

Figure 4.2 shows the results of fitting (graphical view) of VLab data with least-squares fitted curve (Model). From the figure we can observe that when $\frac{L}{\lambda}$ becomes small, the dipole works like an open circuit with maximum impedance and decreases by increasing $\frac{L}{\lambda}$ up to 0.5 after that the impedance increases before decreasing $\frac{L}{\lambda}$ near 1.0.

This trend is reasonable in view of electromagnetics, the magnitude of $|z_0|$ should go through a minimum at near $\frac{L}{\lambda} = 0.5$.

The partial derivation of equation (4.3) with respect to $\frac{L}{\lambda}$ is

$$\frac{d|z_0|}{d\frac{L}{\lambda}} = \exp\left\{\alpha_1 + \frac{\alpha_2\left(1-\left(\frac{L}{\lambda}\right)^2\right)}{\alpha_3+\left(\frac{L}{\lambda}-\alpha_4\right)^2}\right\}\cdot\left[\frac{d|z_0|}{d\frac{L}{\lambda}}\left\{\alpha_1 + \frac{\alpha_2\left(1-\left(\frac{L}{\lambda}\right)^2\right)}{\alpha_3+\left(\frac{L}{\lambda}-\alpha_4\right)^2}\right\}\right]$$

$$= \exp\left\{\alpha_1 + \frac{\alpha_2\left(1-\left(\frac{L}{\lambda}\right)^2\right)}{\alpha_3+\left(\frac{L}{\lambda}-\alpha_4\right)^2}\right\} \tag{4.5}$$

$$\cdot\left[\frac{\left\{\alpha_3+\left(\frac{L}{\lambda}-\alpha_4\right)^2\right\}\left\{-2\alpha_2\frac{L}{\lambda}\right\} - \alpha_2\left(1-\left(\frac{L}{\lambda}\right)^2\right)\left\{2(\frac{L}{\lambda}-\alpha_4)\right\}}{\left\{\alpha_3+\left(\frac{L}{\lambda}-\alpha_4\right)^2\right\}^2}\right],$$

now setting the derivative to zero and the above equation (4.5) becomes

$$\left\{\alpha_3+\left(\frac{L}{\lambda}-\alpha_4\right)^2\right\}\left\{-2\alpha_2\frac{L}{\lambda}\right\} - \alpha_2\left\{1-\left(\frac{L}{\lambda}\right)^2\right\}\left\{2\left(\frac{L}{\lambda}-\alpha_4\right)\right\} = 0, \tag{4.6}$$

$$\{2\alpha_2\alpha_4\}\left(\frac{L}{\lambda}\right)^2 - 2\left\{\alpha_2\alpha_3+\alpha_2(\alpha_4)^2+\alpha_2\right\}\left(\frac{L}{\lambda}\right) + \{2\alpha_2\alpha_4\} = 0, \tag{4.7}$$

$$\frac{L}{\lambda} = \frac{\{\alpha_3+(\alpha_4)^2+1\} \pm \sqrt{\{\alpha_3+(\alpha_4)^2+1\}^2 - 4\alpha_4\alpha_4}}{2\alpha_4}. \tag{4.8}$$

By substituting all the coefficients value into the equation (4.8), we find the $|z_0|$ is minimum at $\frac{L}{\lambda} \approx 0.4988$.

4.3.2 Phase of the Self-impedance ($\angle z_0$)

4 5

The "best" model for the phase of the self-impedance is

$$\angle z_0 \quad \cong \quad \beta_1 \sin\left(2\pi \frac{L}{\lambda}\right), \tag{4.9}$$

where

$\beta_1 := -1.7678$,

with $R^2 = 0.8589$.

According to the R^2 value of 0.8589, our model can explain 85.89% of the VLab's data variability for the phase of the self-impedance. Figure 4.3 shows the results of fitting (graphical view) of VLab data with least-squares fitted curve (Model). From the figure we can observe that the changing of the phase is as like a simple sinusoid wave, and it goes to zero near the $\frac{L}{\lambda} \approx 0.5$.

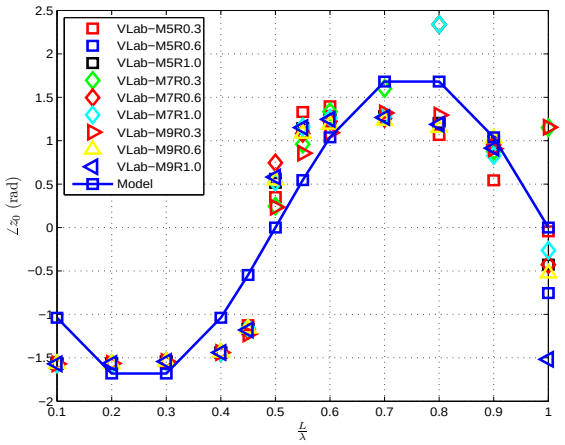

Figure 4.3: Phase of the self-impedance ($\angle z_0$) versus $\frac{L}{\lambda} \in [0.1, 1.0]$ for $M = \{5, 7, 9\}$ and $\frac{R}{\lambda} = \{0.3, 0.6, 1.0\}$.

[4] "Best" in terms of fewness of parameters and R^2.

[5] "Other candidate models are presented in appendix B.

According to electromagnetics, the dipole's electric-field pattern is exactly $\sin\theta$, where θ denotes the spatial angle with respect to the dipole axis. Again, the dipoles go through a resonance at $\frac{L}{\lambda} \approx \frac{1}{2}$, and the phase behavior changes because the real part keeps rising while the imaginary part goes from negative to positive, then starting to track the real part.

Further, the model is independent of M and of $\frac{R}{\lambda}$, for $\frac{L}{\lambda} < 0.4$, even with the largest M and smallest $\frac{R}{\lambda}$, this is because the dipoles are significantly far apart relative to the "size" of their near fields. Thus, the self-impedance may no longer be dependent on the presence of the other dipoles. When the dipoles are larger $\left(\frac{L}{\lambda} > 0.4\right)$, they have started to resonate more strongly, and are more efficiently radiating into each other. Therefore,the self-impedance of the magnitude of the figure 4.2, and the phase of the figure 4.3 have changed with larger the dipole length $\left(\frac{L}{\lambda} > 0.4\right)$ for uniform circular array (UCA) of radius less than 1λ.

4.3.3 Magnitude of the Mutual Impedance: $|z_m|,\ \forall m \in \{1, 2, \cdots, \lceil \frac{M-1}{2} \rceil\}$

The magnitude of the mutual impedance is modeled by varying the radius $\left(\frac{R}{\lambda}\right)$ and the number of elements (M) of the UCA for $\frac{L}{\lambda} = 0.1 \sim 1.0$.

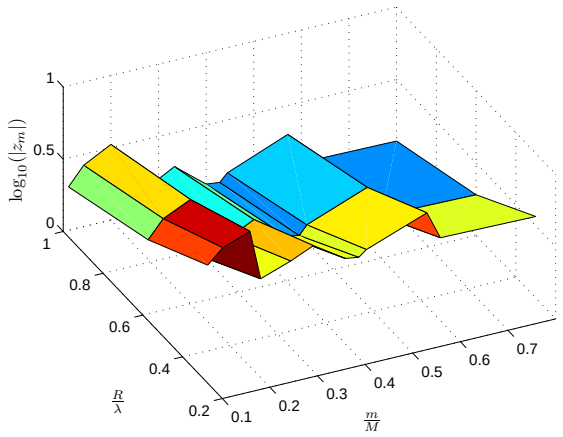

Figure 4.4: VLab data of the magnitude of the mutual impedance($\log_{10}(|z_m|)$) versus $\frac{R}{\lambda}$ and versus $\frac{m}{M}$ at $\frac{L}{\lambda} = 0.2$.

The proposed "best" phenomenological model for the magnitude of the mutual impedance is [6] [7]

$$|z_m| \ \approxeq \ \left\{ 10^{\gamma_1} \left(\frac{R}{\lambda}\right)^{-\gamma_2} \left(\frac{L}{\lambda}\right)^{\gamma_3} \left| \left(1 - \cos\left(2\pi \frac{m}{M}\right)\right)^{\gamma_4} \right| \right\}, \qquad (4.10)$$

where

$\gamma_1 := 2.4097,$

$\gamma_2 := 0.8806,$

[6] "Best" considering the fewness of coefficients.

[7] "Other candidate models are presented in appendix B.

$\gamma_3 := 3.2165,$

$\gamma_4 := -0.3482,$

with $R^2 = 0.8400.$

According to the R^2 value of 0.8400, our model can explain 84.00% of the VLab's data variability for the magnitude of the mutual impedance.

The R^2 is evaluated of the equation (4.10) as

$$\begin{aligned} \log_{10}|z_m| \cong \gamma_1 - \gamma_2 \log_{10}\left(\frac{R}{\lambda}\right) + \gamma_3 \log_{10}\left(\frac{L}{\lambda}\right) \\ +\gamma_4 \log_{10}\left|\left(1 - \cos\left(2\pi\frac{m}{M}\right)\right)\right|. \end{aligned} \tag{4.11}$$

The inversely proportional relationship between the magnitude $|z_m|$ of the mutual impedance and the radius of the circle $(\frac{R}{\lambda})$ in equation (4.10) suggests that the magnitude decreases monotonically with an increase inter-dipole separation by $\frac{R}{\lambda}$. Indeed as $\frac{R}{\lambda} \approx \infty$ the model gives $|z_m| \approx 0$.

This trend is reasonable in terms of electromagnetics because the induced electric fields among the neighboring dipoles are proportional and whose magnitude is inversely proportional to the distance between the emitting dipole and the induced dipole.

Further, the magnitude of the mutual impedance is directly proportional to the length of the dipole. In terms of electromagnetics this is obvious, because the emitted and the induced current depends on the surface area of the dipole and which is increased by increasing the length of the dipole.

The absolute part of the model equation (4.10) suggest that $|z_m|$ increases as the number of dipoles (M) increases in an array. The figure 4.5 shows that the $|z_m|$ is the highest when the number of the dipoles $(M = 9)$ is maximum and decreasing as $|M|$ decreases.

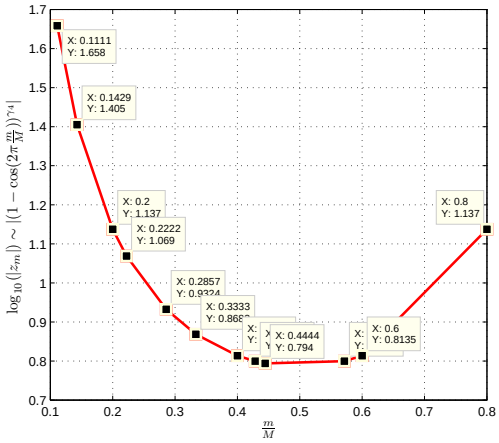

Figure 4.5: The absolute part of the model eq.(4.10) versus $\frac{m}{M}$, where $M = \{5, 7, 9\}$, and $m = 1, 2, 3, 4$.

This is reasonable in terms of electromagnetics because the electric field interaction from the excited dipoles towards the induced dipoles will increase as the number of dipoles are increased in an array.

4.3.4 Phase of the Mutual Impedance: $\angle z_m,\ \forall m \in \{1, 2, \cdots, \lceil \frac{M-1}{2} \rceil\}$

The phase of the mutual impedance is modeled varying the radius $\left(\frac{R}{\lambda}\right)$ and the number of elements (M) of the UCA for $\frac{L}{\lambda} = 0.1 \sim 1.0$.

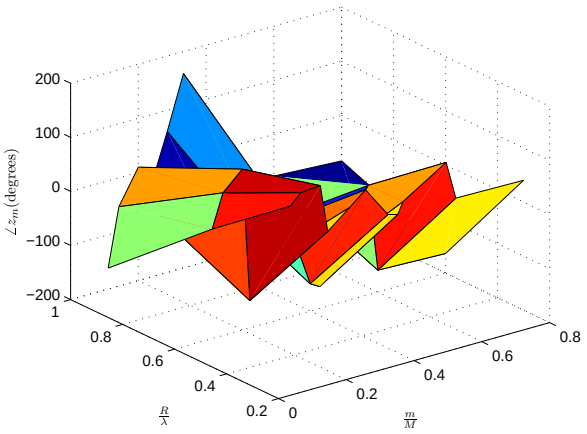

Figure 4.6: VLab data of the phase of the mutual impedance $(\angle z_m)$ versus $\frac{R}{\lambda}$ and versus $\frac{m}{M}$, at $\frac{L}{\lambda} = 0.1$.

The proposed "best" phenomenological model for the phase of the mutual impedance is

[8] [9]

$$\angle z_m \approx \left\{\delta_1 - \delta_2 \sin\left(\pi\left(\frac{m}{M}\right)\right)\right\}\left\{\frac{1 + \delta_3\left(\frac{L}{\lambda}\right) + \delta_4\left(\frac{L}{\lambda}\right)^2}{\delta_5 + \delta_6\left(\frac{L}{\lambda}\right) + \left(\frac{L}{\lambda}\right)^2}\right\}, \quad (4.12)$$

where

$\delta_1 := 0.8439,$

$\delta_2 := 0.1039,$

[8] "Best" considering the fewness of coefficients.

[9] "Other candidate models are presented in appendix B.

$\delta_3 := -3.3494,$

$\delta_4 := 2.7360,$

$\delta_5 := 0.6126,$

$\delta_6 := -1.5517,$

with $R^2 = 0.8209$.

According to the R^2 value of 0.8209, our model can explain 82.09% of the VLab's data variability for the phase of the mutual impedance.

The first part of our model equation (4.12) states that the phase of the mutual impedance is varying sinusoid, shown in the figure 4.7, and this is obvious in view of electromagnetics because the dipole's electric-field pattern is exactly sinusoid.

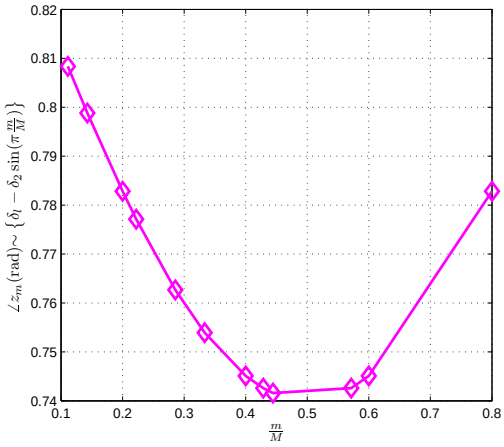

Figure 4.7: The first part of the model eq. (4.12) versus $\frac{m}{M}$.

The fractional inside of the last part of our model equation (4.12) states that the phase of the mutual impedance is varying with the dipole's length as in the figure 4.8.

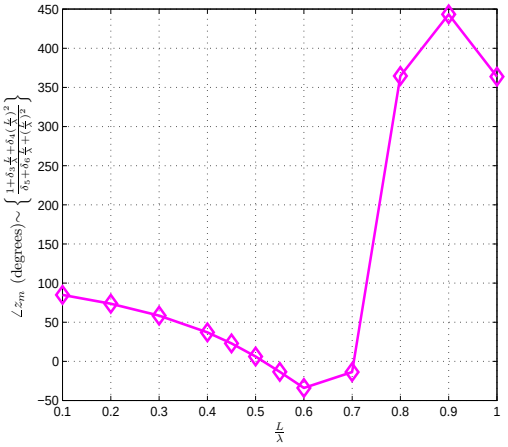

Figure 4.8: The fraction inside of the last part of eq. (4.12) versus $\frac{L}{\lambda}$ in [0.1, 1.0].

4.4 DOA Estimation

To show the utility of the proposed phenomenological mutual coupling model, the performance of the DOA estimation with the UCA of vertical dipoles is analyzed in this section. The details measurement model is same as in the sub-section 3.4.1, here we have used the maximum-likelihood estimator (MLE) for estimating the DOA elevation angle $\hat{\theta}$ and the azimuth angle $\hat{\phi}$ as in the sub-section 3.4.2.

4.4.1 Monte Carlo Simulation Plots

We have considered three scenarios for Monte Carlo simulations as (i) the mutual coupling is exactly known from the VLab simulation data, (ii) the mutual coupling is approximately known from our proposed phenomenological models, and (iii) pretends there's no mutual coupling such that scaled a identity coupling matrix. Monte Carlo simulations uses eq. (4.3), eq. (4.9), eq.(4.10), and eq. (4.12) of $|z_0|$, $\angle z_0$, $|z_m|$, and $\angle z_m$ respectively.

The DOA estimation plots in the figures 4.9 $\sim$ 4.20 show the estimation root-mean-square error (RMSE)[10] of $\hat{\phi}$ and $\hat{\theta}$, versus SNR in dB. Each icon in figures represents 1000 independent Monte-Carlo trails.

These figures verify the usefulness of the proposed phenomenological models that these models offer estimation precisions almost as good as if the exact impedance were known, whereas ignoring mutual coupling causes a degradation that can be several orders of magnitude.

[10]Expression in appendix D.2

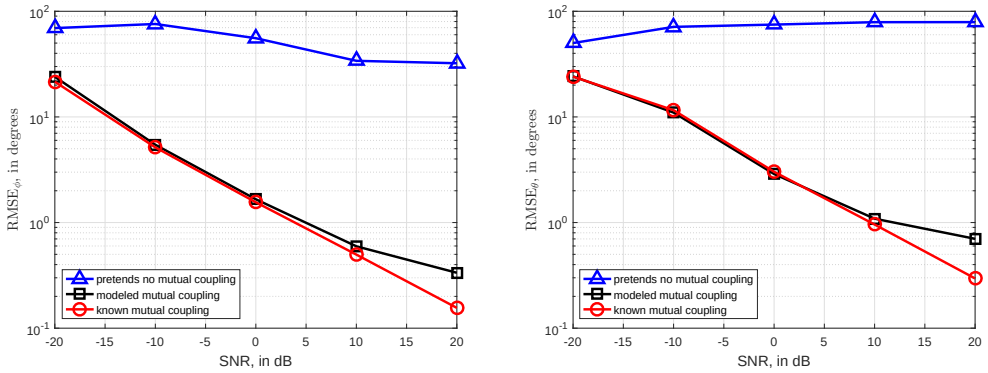

Figure 4.9: RMSE versus SNR at $\frac{L}{\lambda} = 0.45$, $M = 5$, $\frac{R}{\lambda} = 0.6$, and $(\phi, \theta) = (45^0, 60^0)$: 180 sanpshots, 1000 Monte Carlo trials.

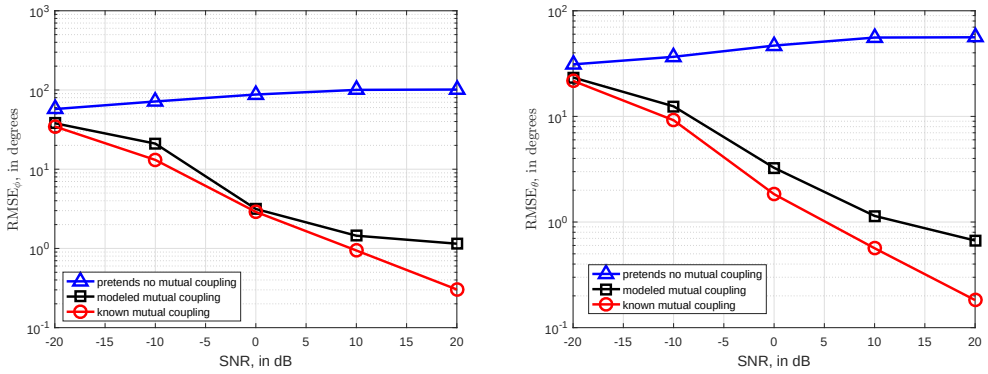

Figure 4.10: RMSE versus SNR at $\frac{L}{\lambda} = 0.5$, $M = 5$, $\frac{R}{\lambda} = 1.0$, and $(\phi, \theta) = (30^0, 30^0)$: 180 sanpshots, 1000 Monte Carlo trials.

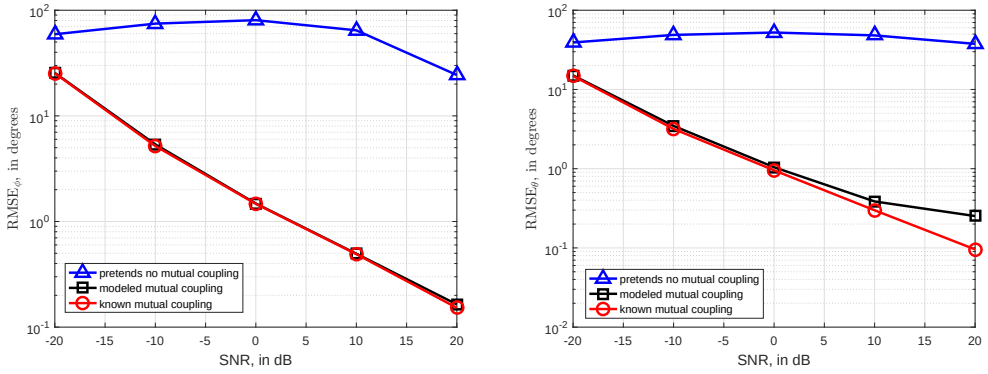

Figure 4.11: RMSE versus SNR at $\frac{L}{\lambda} = 0.55$, $M = 7$, $\frac{R}{\lambda} = 1.0$, and $(\phi, \theta) = (30^0, 30^0)$: 180 sanpshots, 1000 Monte Carlo trials

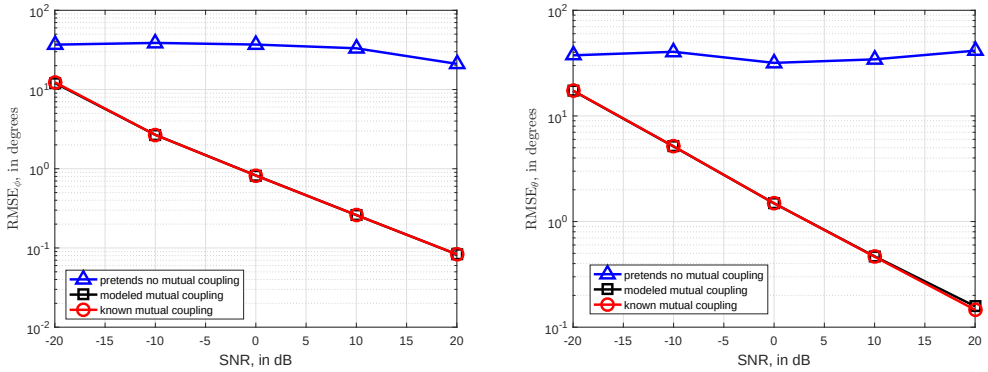

Figure 4.12: RMSE versus SNR at $\frac{L}{\lambda} = 0.6$, $M = 7$, $\frac{R}{\lambda} = 1.0$, and $(\phi, \theta) = (30^0, 60^0)$: 180 sanpshots, 1000 Monte Carlo trials.

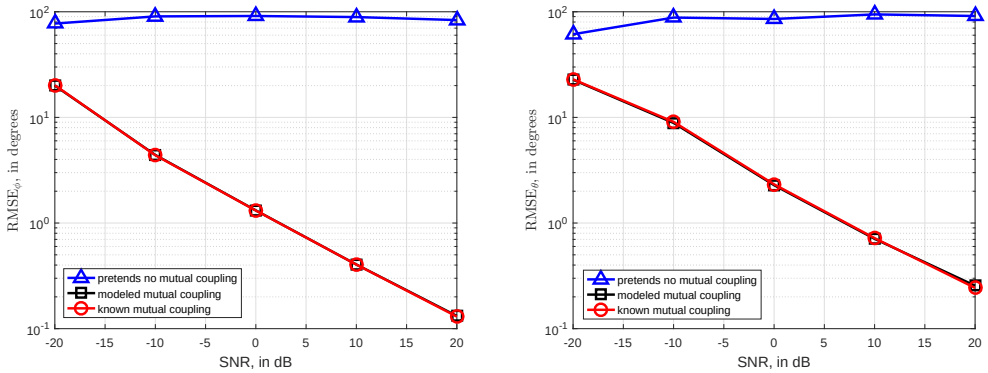

Figure 4.13: RMSE versus SNR at $\frac{L}{\lambda} = 0.7$, $M = 5$, $\frac{R}{\lambda} = 0.6$, and $(\phi, \theta) = (30^0, 60^0)$: 180 sanpshots, 1000 Monte Carlo trials.

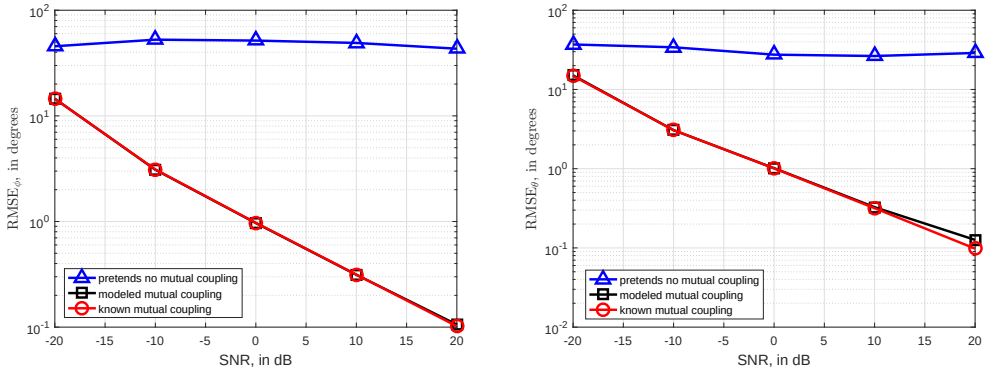

Figure 4.14: RMSE versus SNR at $\frac{L}{\lambda} = 0.7$, $M = 7$, $\frac{R}{\lambda} = 1.0$, and $(\phi, \theta) = (30^0, 45^0)$: 180 sanpshots, 1000 Monte Carlo trials

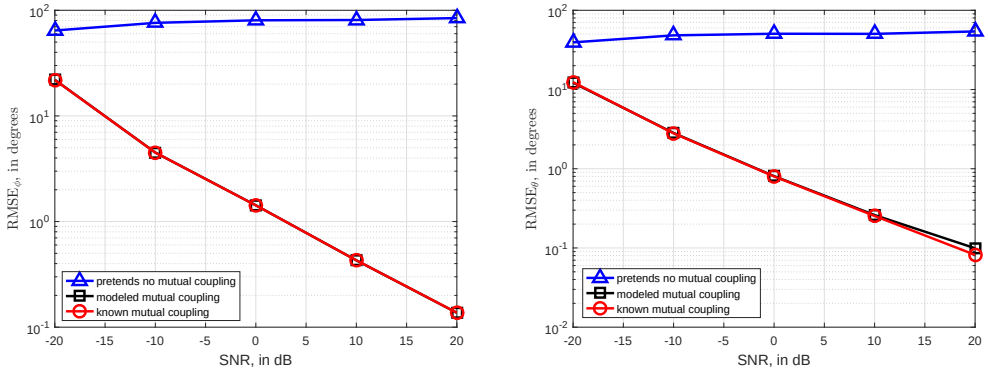

Figure 4.15: RMSE versus SNR at $\frac{L}{\lambda} = 0.7$, $M = 9$, $\frac{R}{\lambda} = 1.0$, and $(\phi, \theta) = (30^0, 30^0)$: 180 sanpshots, 1000 Monte Carlo trials.

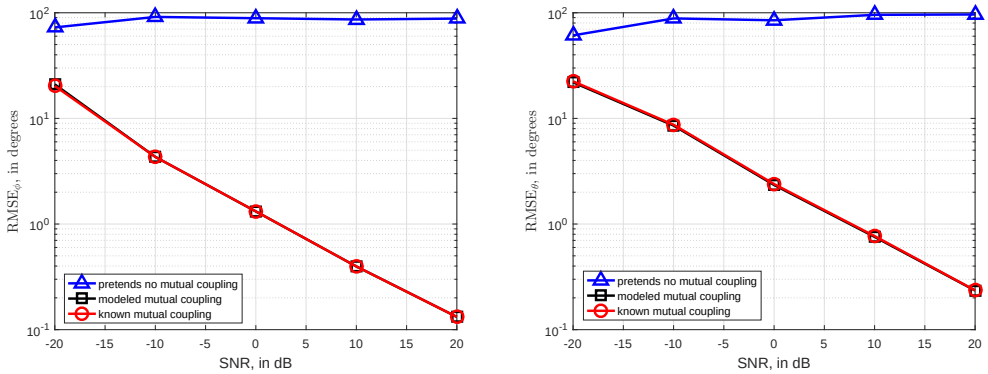

Figure 4.16: RMSE versus SNR at $\frac{L}{\lambda} = 0.8$, $M = 9$, $\frac{R}{\lambda} = 0.6$, and $(\phi, \theta) = (30^0, 60^0)$: 180 sanpshots, 1000 Monte Carlo trials

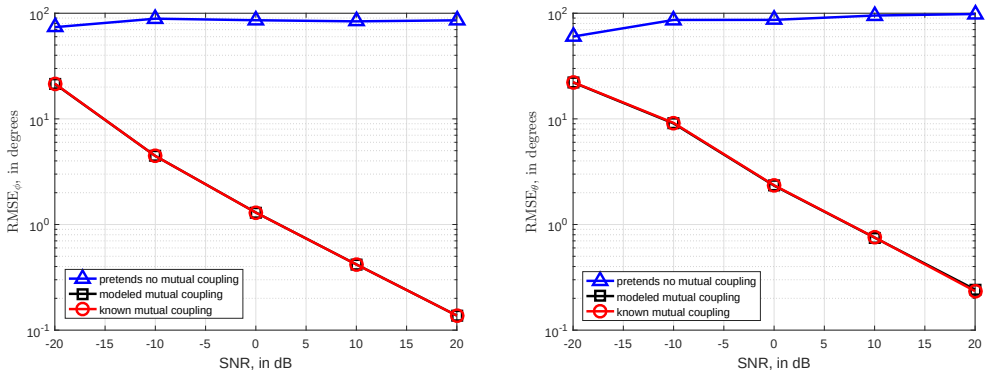

Figure 4.17: RMSE versus SNR at $\frac{L}{\lambda} = 0.8$, $M = 7$, $\frac{R}{\lambda} = 0.6$, and $(\phi, \theta) = (30^0, 60^0)$: 180 sanpshots, 1000 Monte Carlo trials.

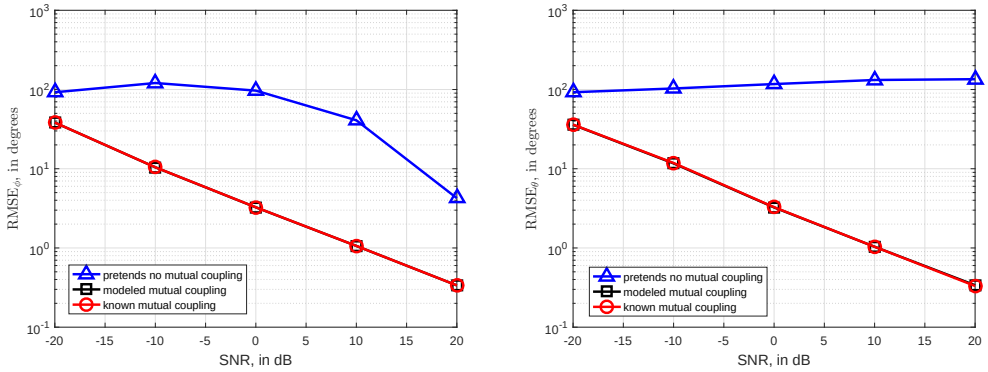

Figure 4.18: RMSE versus SNR at $\frac{L}{\lambda} = 0.8$, $M = 5$, $\frac{R}{\lambda} = 0.3$, and $(\phi, \theta) = (30^0, 45^0)$: 180 sanpshots, 1000 Monte Carlo trials.

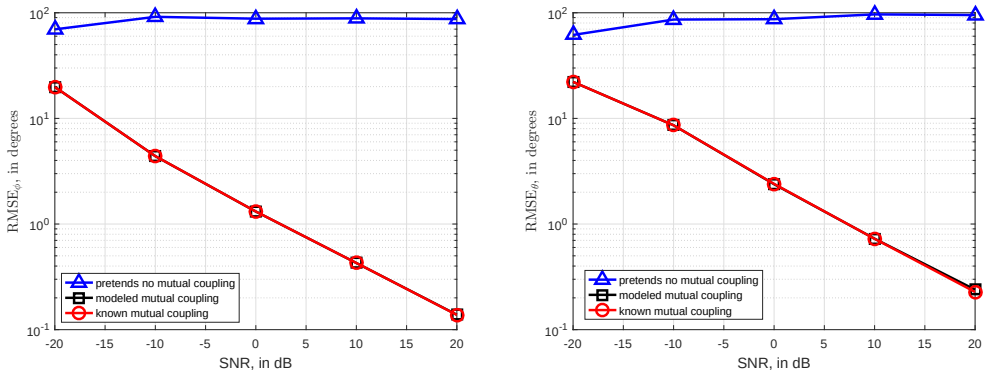

Figure 4.19: RMSE versus SNR at $\frac{L}{\lambda} = 0.9$, $M = 5$, $\frac{R}{\lambda} = 0.6$, and $(\phi, \theta) = (30^0, 45^0)$: 180 sanpshots, 1000 Monte Carlo trials

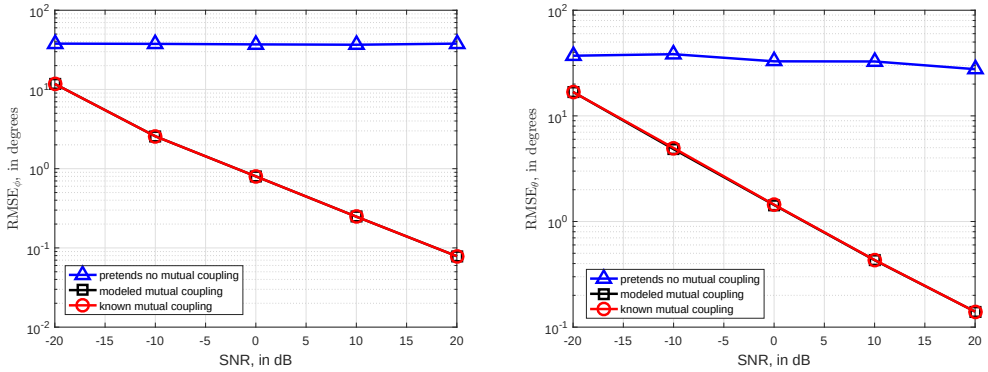

Figure 4.20: RMSE versus SNR at $\frac{L}{\lambda} = 0.9$, $M = 9$, $\frac{R}{\lambda} = 1.0$, and $(\phi, \theta) = (30^0, 60^0)$: 180 sanpshots, 1000 Monte Carlo trials.

4.5 Summary

The proposed phenomenological models for the magnitude and the phase of the self-and mutual impedance for the UCA vertical dipoles with inter-dipole spacing less than 1λ are summarized in the Table 4.2.

Table 4.2: The best phenomenological models for a UCA of vertical dipoles of small circle's radius

Inter-dipole spacing of vertically oriented dipoles, less than 1λ.	
Impedance	Models
$\lvert z_0\rvert$	$\lvert z_0\rvert \;\approxeq\; \exp\left\{\left\lvert \alpha_1 + \frac{\alpha_2\left(1-\left(\frac{L}{\lambda}\right)^2\right)}{\alpha_3+\left(\frac{L}{\lambda}-\alpha_4\right)^2}\right\rvert\right\}$, where $\alpha_1 := 8.3302, \alpha_2 := -0.1375, \alpha_3 := 0.0294, \alpha_4 := 0.5173$.
$\angle z_0$	$\angle z_0 \approxeq \beta_1 \sin\left(2\pi\frac{L}{\lambda}\right)$, where $\beta_1 := -1.7678$.
$\lvert z_m\rvert$	$\lvert z_m\rvert \approxeq \left\{10^{\gamma_1}\left(\frac{R}{\lambda}\right)^{-\gamma_2}\left(\frac{L}{\lambda}\right)^{\gamma_3}\left\lvert\left(1-\cos\left(2\pi\frac{m}{M}\right)\right)^{\gamma_4}\right\rvert\right\}$, where $\gamma_1 := 2.4097, \gamma_2 := 0.8806, \gamma_3 := 3.2165, \gamma_4 := -0.3482$.
$\angle z_m$	$\angle z_m \approxeq \left\{\delta_1 - \delta_2 \sin\left(\pi\left(\frac{m}{M}\right)\right)\right\}\left\{\frac{1+\delta_3\left(\frac{L}{\lambda}\right)+\delta_4\left(\frac{L}{\lambda}\right)^2}{\delta_5+\delta_6\left(\frac{L}{\lambda}\right)+\left(\frac{L}{\lambda}\right)^2}\right\}$, where $\delta_1 := 0.8439, \delta_2 := 0.1039, \delta_3 := -3.3494, \delta_4 := 2.7360, \delta_5 := 0.6126, \delta_6 := -1.5517$.

Chapter 5

UCA of Radially Oriented Dipoles with Inter-dipole Spacing less than 1.0λ

A "phenomenological" or "behavioral" approach is used here to model the electromagnetic mutual impedance among dipoles placed uniformly on a circle, with the dipole axis radially oriented to the circular plane, where the inter-dipoles spacing vary from 0.2 λ to 1.0 λ.

5.1 Introduction

In this chapter, we have considered a circular array shown in the figure 5.1, where the dipoles are oriented radially and spaced uniformly on the $x - y$ plane. The angular location of each dipole is

$$\phi_m = 2\pi(m-1)/M, \tag{5.1}$$

where M is the number of dipoles in an array, $m = 1, 2, ..., M$,

and the inter-dipole spacing is

$$\Delta = 2R\sin(\pi/M), \tag{5.2}$$

where R is the radius of the circle.

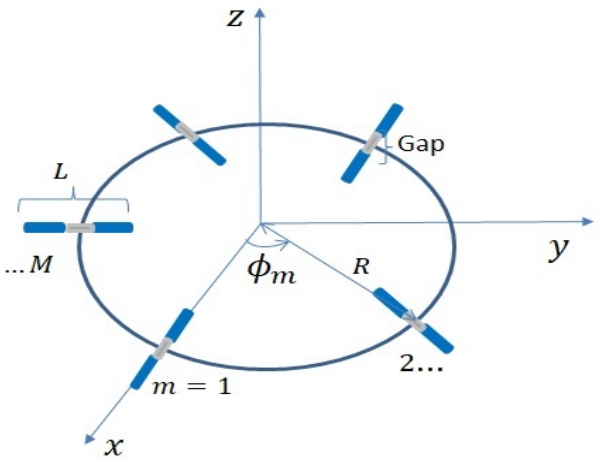

Figure 5.1: The spatial geometry of a circular array of $M = 5$ identical dipoles, spaced uniformly on a circle, but oriented radially to the circle's radius.

Such a uniform circular array (UCA) of dipoles oriented radially to the circle's radius – it has been used in [71, 72].

5.2 Basic Consideration to Generate the Mutual Impedance Matrix

In this chapter, we have assumed for all subsequently presented results: each dipole's diameter is maintained at 0.02λ millimeters; each dipole's feeding gap equals $\frac{\lambda}{50}$; the voltage source's internal impedance is always matched to a half-wavelength dipole, regardless of the actual value of $\frac{L}{\lambda}$; there exist $1,000$ segments The following $3 \times 3 \times 12$ combinations of numerical settings will be evaluated:

1) a radius of $R \in \{0.5, 0.75, 1.0\}\lambda$ for the circle,

2) $M \in \{5, 7, 9\}$ number of identical dipoles on the circle[1],

3) each dipole's electric length $\frac{L}{\lambda} \in \{0.1, 0.2, 0.3, 0.4, 0.45,$
$0.5, 0.55, 0.6, 0.7, 0.8, 0.9, 1.0\}$,

4) inter-dipole spacing is shown in the Table 5.1.

Table 5.1: Inter-dipole spacing in a UCA of radially oriented dipoles

inter-dipole spacing, $\Delta = 2R\sin(\pi/M)$			
Radius	$M = 5$	$M = 7$	$M = 9$
R = 0.5 λ	0.58 λ	0.43 λ	0.34 λ
R = 0.75 λ	0.88 λ	0.65 λ	0.51 λ
R = 1.0 λ	1.17 λ	0.86 λ	0.68 λ

[1]The student edition of EMCoS Antenna VLab V 1.0.1 SV would run out of memory for a higher value for M.

5.3 Phenomenological Model of the Entire Trivariate Dataset

[2]

5.3.1 Magnitude of the Self-impedance ($|z_0|$)

The "best" model [3] for the magnitude of the self-impedance for the entire trivariate dataset is found as

$$|z_0| \;\approxeq\; \exp\left\{\left|\alpha_1 + \frac{\alpha_2\left(1-\left(\frac{L}{\lambda}\right)^2\right)}{\alpha_3+\left(\frac{L}{\lambda}-\alpha_4\right)^2}\right|\right\}, \tag{5.3}$$

at

$\alpha_1 := 8.4156$,

$\alpha_2 := -0.1450$,

$\alpha_3 := 0.0303$,

$\alpha_4 := 0.5161$,

with $R^2 := 0.9503$.

According to the R^2 value of 0.9503, our model can explain 95.03% of the VLab's data variability for the magnitude of the self-impedance.

The R^2 is evaluated of the equation (5.3) as

$$\log_e|z_0| \approxeq \left\{\left|\alpha_1 + \frac{\alpha_2\left(1-\left(\frac{L}{\lambda}\right)^2\right)}{\alpha_3+\left(\frac{L}{\lambda}-\alpha_4\right)^2}\right|\right\}. \tag{5.4}$$

Figure 5.2 shows the results of fitting (graphical view) of VLab data with least-squares fitted curve (Model). From the figure we can observe that

[2] "Other candidate models are presented in appendix C.

[3] "Best" considering the fewness of coefficients.

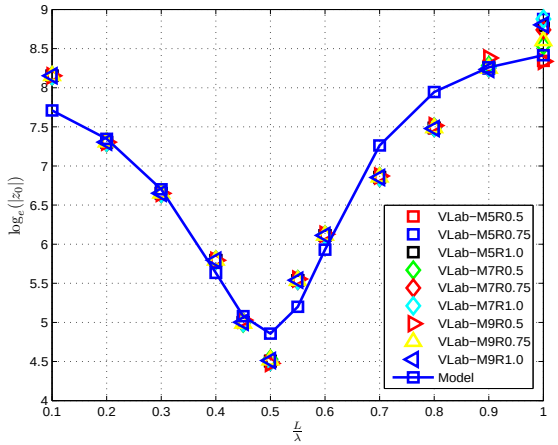

Figure 5.2: Magnitude of the self-impedance ($\log_e(|z_0|)$) versus $\frac{L}{\lambda} \in [0.1, 1.0]$ for $M = \{5, 7, 9\}$ and $\frac{R}{\lambda} = \{0.5, 0.75, 1.0\}$.

when $\frac{L}{\lambda}$ becomes small, the dipole works like an open circuit with maximum impedance and decreases by increasing $\frac{L}{\lambda}$ up to 0.5 after that the impedance increases before decreasing $\frac{L}{\lambda}$ near 1.0.

This trend is reasonable in view of electromagnetics, the magnitude of $|z_0|$ should go through a minimum at near $\frac{L}{\lambda} = 0.5$,

The partial derivation of equation (5.3) with respect to $\frac{L}{\lambda}$ is

$$\frac{d|z_0|}{d\frac{L}{\lambda}} = \exp\left\{\alpha_1 + \frac{\alpha_2\left(1-\left(\frac{L}{\lambda}\right)^2\right)}{\alpha_3 + \left(\frac{L}{\lambda}-\alpha_4\right)^2}\right\} \cdot \left[\frac{d|z_0|}{d\frac{L}{\lambda}}\left\{\alpha_1 + \frac{\alpha_2\left(1-\left(\frac{L}{\lambda}\right)^2\right)}{\alpha_3 + \left(\frac{L}{\lambda}-\alpha_4\right)^2}\right\}\right]$$

$$= \exp\left\{\alpha_1 + \frac{\alpha_2\left(1-\left(\frac{L}{\lambda}\right)^2\right)}{\alpha_3 + \left(\frac{L}{\lambda}-\alpha_4\right)^2}\right\} \tag{5.5}$$

$$\cdot \left[\frac{\left\{\alpha_3 + \left(\frac{L}{\lambda}-\alpha_4\right)^2\right\}\left\{-2\alpha_2\frac{L}{\lambda}\right\} - \alpha_2\left(1-\left(\frac{L}{\lambda}\right)^2\right)\left\{2(\frac{L}{\lambda}-\alpha_4)\right\}}{\left\{\alpha_3 + \left(\frac{L}{\lambda}-\alpha_4\right)^2\right\}^2}\right],$$

now setting the derivative to zero and the above equation (5.5) becomes

$$\left\{\alpha_3 + \left(\frac{L}{\lambda} - \alpha_4\right)^2\right\}\left\{-2\alpha_2\frac{L}{\lambda}\right\} - \alpha_2\left\{1 - \left(\frac{L}{\lambda}\right)^2\right\}\left\{2\left(\frac{L}{\lambda} - \alpha_4\right)\right\} = 0 \quad (5.6)$$

$$\{2\alpha_2\alpha_4\}\left(\frac{L}{\lambda}\right)^2 - 2\left\{\alpha_2\alpha_3 + \alpha_2(\alpha_4)^2 + \alpha_2\right\}\left(\frac{L}{\lambda}\right) + \{2\alpha_2\alpha_4\} = 0, \quad (5.7)$$

$$\frac{L}{\lambda} = \frac{\{\alpha_3 + (\alpha_4)^2 + 1\} \pm \sqrt{\{\alpha_3 + (\alpha_4)^2 + 1\}^2 - 4\alpha_4\alpha_4}}{2\alpha_4}. \quad (5.8)$$

By substituting all the coefficients value into equation (5.8), we find the $|z_0|$ is minimum at $\frac{L}{\lambda} \approx 0.4984$.

5.3.2 Phase of the Self-impedance ($\angle z_0$)

[4] [5]

The "best" model for the phase of the self-impedance is

$$\angle z_0 \quad \cong \quad \beta_1 \sin\left(2\pi \frac{L}{\lambda}\right), \tag{5.9}$$

where

$\beta_1 := -1.7454$,

with $R^2 = 0.8803$.

According to the R^2 value of 0.8803, our model can explain 88.03% of the VLab's data variability for the phase of the self-impedance. Figure 5.3 shows the results of fitting (graphical view) of VLab data with least-squares fitted curve (Model). From the figure we can observe that the changing of phase is as like a simple sinusoid wave, and it goes to zero near the $\frac{L}{\lambda} \approx 0.5$.

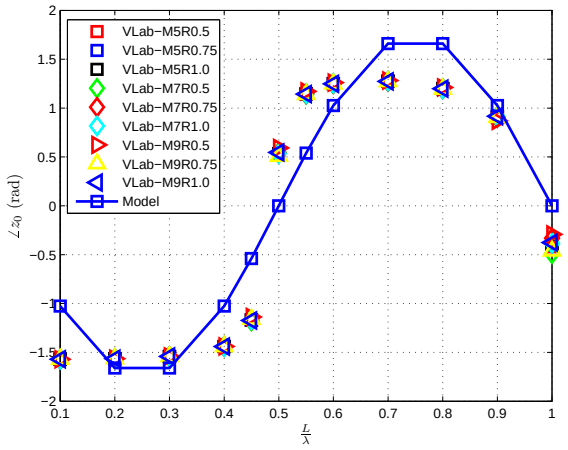

Figure 5.3: Phase of the self-impedance ($\angle z_0$) versus $\frac{L}{\lambda} \in [0.1, 1.0]$ for $M = \{5, 7, 9\}$ and $\frac{R}{\lambda} = \{0.5, 0.75, 1.0\}$.

[4] "Best" in terms of fewness of parameters and R^2.

[5] "Other candidate models are presented in appendix C.

According to electromagnetics, the dipole's electric-field pattern is exactly $\sin\theta$, where θ denotes the spatial angle with respect to the dipole axis. Again, the dipoles go through a resonance at $\frac{L}{\lambda} \approx \frac{1}{2}$, and the phase behavior changes because the real part keeps rising while the imaginary part goes from negative to positive, then start to track the real part.

Further, the magnitude and the phase of the self-impedance is independent of M and of $\frac{R}{\lambda}$, as shown in the figure 5.2, and 5.3, and this independence is reasonable in terms of electromagnetics, because of the rotational symmetry of a UCA about its origin. The re-radiated signal from the induced antenna to the excited antenna cancels each other and which is independent on the number of antennas (M) and the radius ($\frac{R}{\lambda}$) of a UCA.

5.3.3 Magnitude of the Mutual Impedance: $|z_m|,\ \forall m \in \{1, 2, \cdots, \lceil \frac{M-1}{2} \rceil\}$

The magnitude of the mutual impedance is modeled by varying the radius $\left(\frac{R}{\lambda}\right)$ and the number of elements (M) of the UCA for $\frac{L}{\lambda} = 0.1 \sim 1.0$.

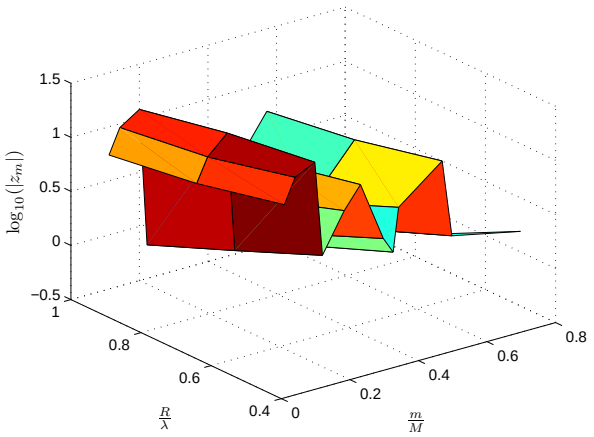

Figure 5.4: Magnitude of the mutual impedance of VLab data ($\log_{10}(|z_m|)$) versus $\frac{R}{\lambda}$ and versus $\frac{m}{M}$ at $\frac{L}{\lambda} = 0.1$.

The proposed best phenomenological model for the magnitude of the mutual impedance is [6] [7]

$$|z_m| \ \cong \ \left\{ 10^{\gamma_1} \left(\frac{R}{\lambda}\right)^{-\gamma_2} \left(\frac{L}{\lambda}\right)^{\gamma_3} \left| \left(1 - \cos\left(2\pi \frac{m}{M}\right)\right)^{\gamma_4} \right| \right\}, \qquad (5.10)$$

where

$\gamma_1 := 1.6695,$

$\gamma_2 := 1.5394,$

[6] "Best" considering the fewness of coefficients.

[7] "Other candidate models are presented in appendix C.

$\gamma_3 := 2.8833$,

$\gamma_4 := -1.3020$,

with $R^2 = 0.8488$.

According to the R^2 value of 0.8488, our model can explain 84.88% of the VLab's data variability for the magnitude of the mutual impedance.

The R^2 is evaluated of the equation (5.10) as

$$\begin{aligned} \log_{10}|z_m| \cong \gamma_1 - \gamma_2 \log_{10}\left(\frac{R}{\lambda}\right) + \gamma_3 \log_{10}\left(\frac{L}{\lambda}\right) \\ +\gamma_4 \log_{10}\left|\left(1 - \cos\left(2\pi\frac{m}{M}\right)\right)\right|. \end{aligned} \tag{5.11}$$

The inversely proportional relationship between the magnitude $|z_m|$ of the mutual impedance and the radius of the circle $(\frac{R}{\lambda})$ in equation (5.10) suggests that the magnitude decreases monotonically with an increase inter-dipole separation by $\frac{R}{\lambda}$. Indeed as $\frac{R}{\lambda} \approx \infty$ the model gives $|z_m| \approx 0$.

This trend is reasonable in terms of electromagnetics because the induced electric fields among the neighboring dipoles are proportional and whose magnitude is inversely proportional to the distance between the emitting dipole and the induced dipole.

Further, the magnitude of the mutual impedance is directly proportional to the length of the dipole. In terms of electromagnetics this is obvious, because the emitted and the induced current depends on the surface area of the dipole and which is increased by increasing the length of the dipole.

The absolute part of the model equation (5.10) (as shown in figure 5.5) suggest that $|z_m|$ is increased as the number of dipoles (M) increase in an array.

This is considerable in terms of electromagnetics, because the excited voltage and the induced voltage are increased as the number of antennas in

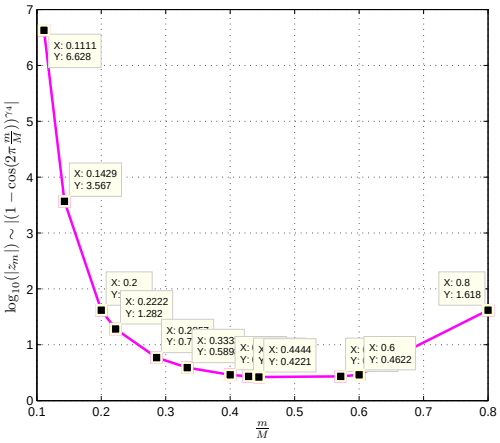

Figure 5.5: The absolute part of the model eq.(5.10) versus $\frac{m}{M}$, where $M = \{5, 7, 9\}$, and $m = 1, 2, 3, 4$.

an array increased as well as the mutual impedance increases.

5.3.4 Phase of the Mutual Impedance: $\angle z_m,\ \forall m \in \{1, 2, \cdots, \lceil \frac{M-1}{2} \rceil\}$

The phase of the mutual impedance is modeled by varying the radius $\left(\frac{R}{\lambda}\right)$ and the number of elements (M) of the UCA for $\frac{L}{\lambda} = 0.1 \sim 1.0$.

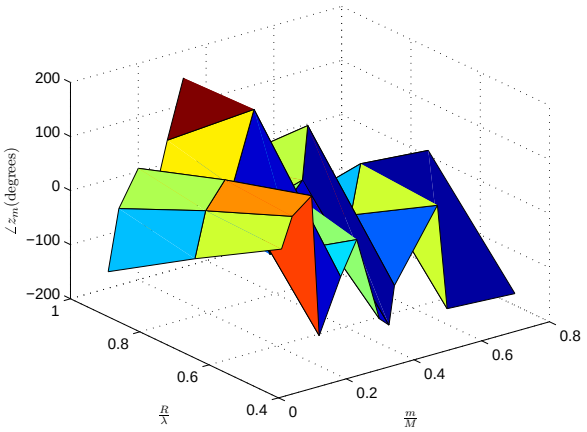

Figure 5.6: Phase of the mutual impedance of VLab data $(\angle z_m)$ versus $\frac{R}{\lambda}$ and versus $\frac{m}{M}$, at $\frac{L}{\lambda} = 0.1$.

The proposed best phenomenological model for the phase of the mutual impedance is

[8] [9]

$$\angle z_m \approxeq \delta_1 + \delta_2 \frac{L}{\lambda} + \delta_3 \frac{R}{\lambda} + \delta_4 \frac{m}{M}, \tag{5.12}$$

where

$\delta_1 := 12.0839,$

$\delta_2 := 1.0268,$

[8] "Best" considering the fewness of coefficients.

[9] "Other candidate models are presented in appendix C.

$\delta_3 := -16.4643,$

$\delta_4 := 1.8900,$

with $R^2 = 0.8134$.

According to the R^2 value of 0.8134, our model can explain 81.34% of the VLab's data variability for the phase of the mutual impedance.

The phenomenological model of the phase in equation (5.12) suggests that the phase of the mutual impedance varies linearly with the dipole's length $\frac{L}{\lambda}$. In terms of electromagnetics this is considerable because the radiation is emitted from driving dipole along that dipole's entire length and is received by the induced dipole along the induced dipole's entire length. The average of such distances increases linearly with the two dipoles' length. Hence, the phase would change linearly with $\frac{L}{\lambda}$.

The negative value of the coefficient δ_3 in equation (5.12) suggests that the phase of the mutual impedance decreases linearly with the inter-dipole spacing by varying $\frac{R}{\lambda}$. In terms of electromagnetics this is reasonable because the radiation propagation outward from the excited dipole, its phase would change linearly with the distance transverse.

Also, the phase of the mutual impedance varies linearly with $\frac{m}{M}$. This is reasonable in terms of electromagnetics, because when the number of antennas in an array increases, the interaction of the phase of the radiation and the induced wave will change accordingly.

5.4 DOA Estimation

To show the utility of the proposed phenomenological mutual coupling model, the performance of the DOA estimation with the UCA of radially oriented dipoles is analyzed in this section.

For an array of vertically oriented dipoles, the effective length of a dipole can be factor out as a multiplicative factor common to all entries of the array manifold. But to express the array manifold of radially oriented dipoles where each dipole's effective length as a function of that dipole's orientation is considered. The derivation of the array manifold for radially oriented dipoles is used here as same as the equation (4.6) on p.42 of [19].

The maximum-likelihood estimator (MLE) is used here to estimate the elevation angle $\hat{\theta}$ and the azimuth angle $\hat{\phi}$ as described in the sub-section 3.4.2.

5.4.1 Monte Carlo Simulation Plots

Three cases are shown by assuming the estimation algorithm

(i) knows the exact mutual coupling matrix in $\mathbf{C}$ = VLab data;

(ii) pretends there's no mutual coupling such that $\mathbf{C}$ is a scaled identity matrix;

(iii) assumes the proposed phenomenological model of the mutual coupling matrix such that $\mathbf{C}$ is computed from our model equations;

To have a fair comparison with the same level of SNR, in each of the above cases the mutual coupling matrix is normalized by its Frobenius norm.

Monte Carlo simulations using eq. (5.3), eq. (5.9), eq.(5.10), and eq. (5.12) of $|z_0|$, $\angle z_0$, $|z_m|$, and $\angle z_m$ respectively.

The DOA estimation plots in the figures 5.7 $\sim$ 5.12 show the estimation root-mean-square error (RMSE)[10] of $\hat{\phi}$ and $\hat{\theta}$, versus SNR in dB. Each icon in figures represents 1000 independent Monte-Carlo trails. [11]

These figures verify the usefulness of the proposed phenomenological models that these models offer estimation precisions almost as good as if the exact impedance were known, whereas ignoring mutual coupling causes a degradation that can be several orders of magnitude.

[10]Expression in appendix D.2

[11]The (γ, η) in the DOA plots figure caption is the polarization angle and the polarization phase diff. respectivley as in the p. 40 of ref. [19]

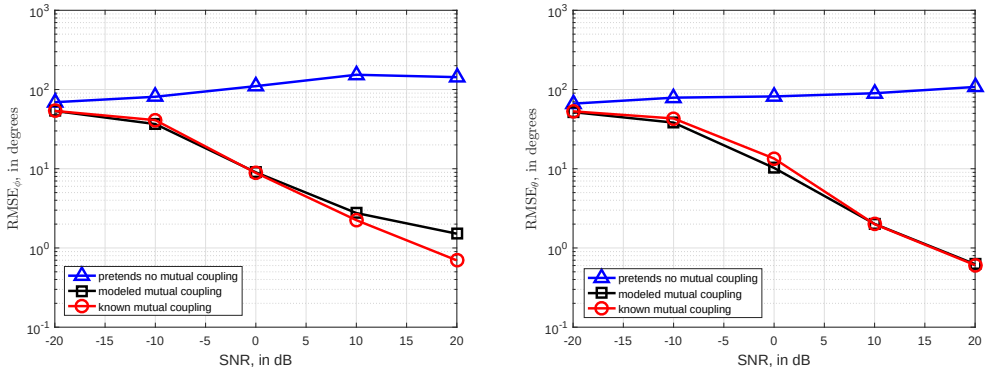

Figure 5.7: RMSE versus SNR at $\frac{L}{\lambda} = 0.45$, $M = 5$, $\frac{R}{\lambda} = 0.5$, $(\phi,\ \theta) = (45^0, 30^0)$, and $(\gamma,\ \eta) = (45^0, 30^0)$: 180 sanpshots, 1000 Monte Carlo trials.

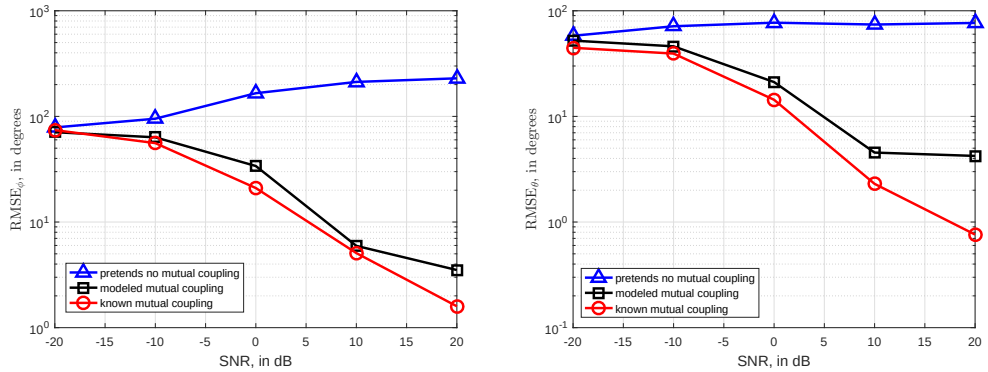

Figure 5.8: RMSE versus SNR at $\frac{L}{\lambda} = 0.5$, $M = 5$, $\frac{R}{\lambda} = 0.5$, $(\phi,\ \theta) = (30^0, 15^0)$, and $(\gamma,\ \eta) = (45^0, 30^0)$: 180 sanpshots, 1000 Monte Carlo trials.

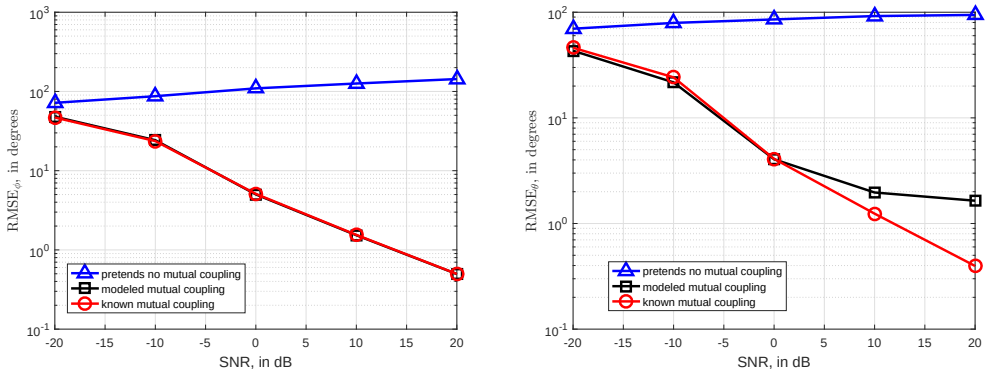

Figure 5.9: RMSE versus SNR at $\frac{L}{\lambda} = 0.55$, $M = 7$, $\frac{R}{\lambda} = 0.5$, $(\phi,\ \theta) = (45^0, 30^0)$, and $(\gamma,\ \eta) = (45^0, 30^0)$: 180 sanpshots, 1000 Monte Carlo trials

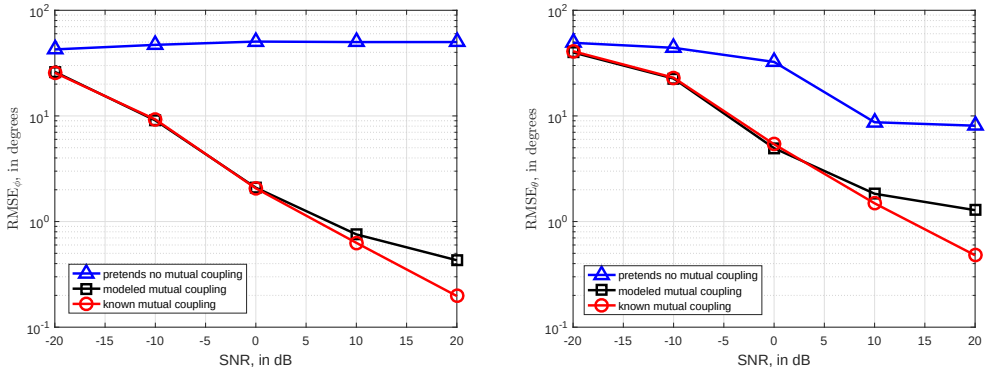

Figure 5.10: RMSE versus SNR at $\frac{L}{\lambda} = 0.6$, $M = 5$, $\frac{R}{\lambda} = 0.75$, $(\phi,\ \theta) = (30^0, 60^0)$, and $(\gamma,\ \eta) = (45^0, 30^0)$: 180 sanpshots, 1000 Monte Carlo trials.

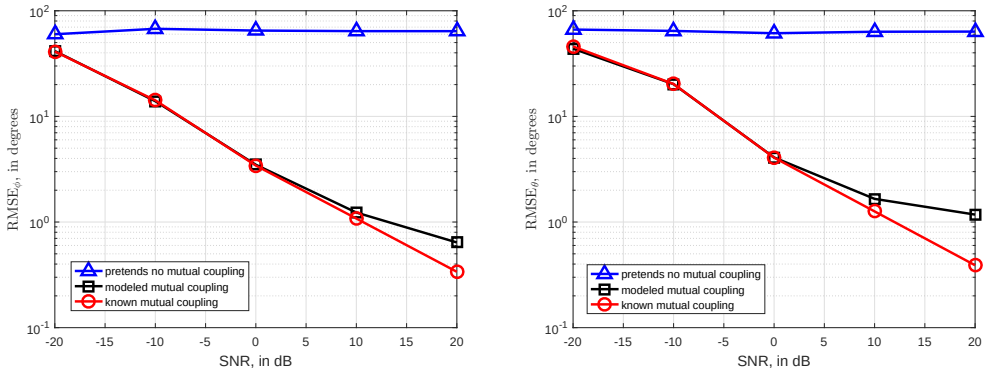

Figure 5.11: RMSE versus SNR at $\frac{L}{\lambda} = 0.6$, $M = 5$, $\frac{R}{\lambda} = 0.5$, $(\phi,\ \theta) = (45^0, 45^0)$, and $(\gamma,\ \eta) = (45^0, 60^0)$: 180 sanpshots, 1000 Monte Carlo trials.

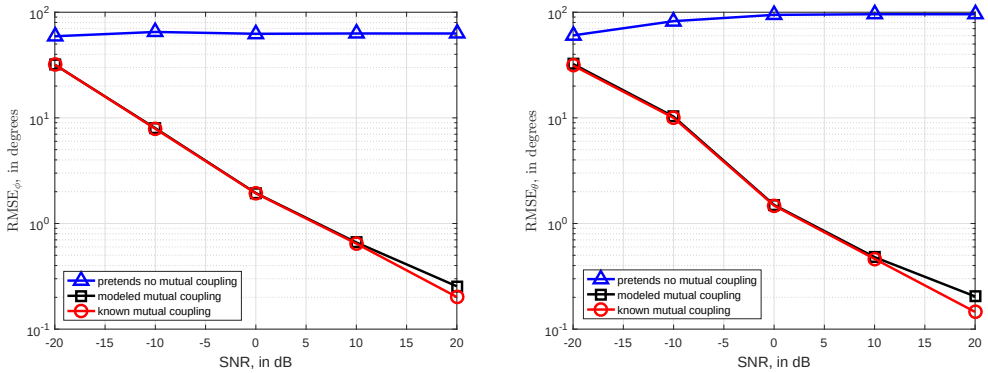

Figure 5.12: RMSE versus SNR at $\frac{L}{\lambda} = 0.7$, $M = 5$, $\frac{R}{\lambda} = 0.75$, $(\phi,\ \theta) = (45^0, 30^0)$, and $(\gamma,\ \eta) = (45^0, 30^0)$: 180 sanpshots, 1000 Monte Carlo trials

5.5 Summary

The proposed phenomenological models for the magnitude and the phase of the self-and mutual impedance for the UCA radial dipoles with inter-dipole spacing less than 1λ are summarized in the Table 5.2.

Table 5.2: The best phenomenological models for a UCA of radial dipoles

Inter-dipole spacing of radially oriented dipoles, less than 1λ.	
Impedance	Models
$\lvert z_0\rvert$	$\lvert z_0\rvert \approxeq \exp\left\{\left\lvert \alpha_1 + \frac{\alpha_2\left(1-\left(\frac{L}{\lambda}\right)^2\right)}{\alpha_3+\left(\frac{L}{\lambda}-\alpha_4\right)^2}\right\rvert\right\}$, where $\alpha_1 := 8.4156, \alpha_2 := -0.1450, \alpha_3 := 0.0303, \alpha_4 := 0.5161$.
$\angle z_0$	$\angle z_0 \approxeq \beta_1 \sin\left(2\pi\frac{L}{\lambda}\right)$, where $\beta_1 := -1.7454$.
$\lvert z_m\rvert$	$\lvert z_m\rvert \approxeq \left\{10^{\gamma_1}\left(\frac{R}{\lambda}\right)^{-\gamma_2}\left(\frac{L}{\lambda}\right)^{\gamma_3}\left\lvert\left(1-\cos\left(2\pi\frac{m}{M}\right)\right)^{\gamma_4}\right\rvert\right\}$, where $\gamma_1 := 1.6695, \gamma_2 := 1.5394, \gamma_3 := 2.8833, \gamma_4 := -1.3020$.
$\angle z_m$	$\angle z_m \approxeq \delta_1 + \delta_2\frac{L}{\lambda} + \delta_3\frac{R}{\lambda} + \delta_4\frac{m}{M}$, where $\delta_1 := 12.0839, \delta_2 := 1.0268, \delta_3 := -16.4643, \delta_4 := 1.8900$.

Chapter 6

Conclusion and Future Work

6.1 Conclusion

The phenomenological study of the mutual coupling is a new approach for modeling the mutual coupling of a UCA. In this thesis, we have obtained the phenomenological models of the mutual coupling in a simple closed form comparing to existing expression of "Induced EMF method" or "Integration method" of the full complexity of nested integrals/sums in each entry of the coupling matrix. We have used the EMCoS antenna VLab computer simulation software to calculate the mutual coupling among an array. The EMCoS uses the well-known method-of-moments (MoM) approach to calculate the mutual coupling effects in an array.

We have proposed several phenomenological models with unknown coefficients based on the expected electromagnetic trends and the graphical behavior of the VLab data plots of various scenarios. The unknown coefficients are optimized by least-squares fitting. Then, based on the fitting parameter R^2, the low degrees-of-freedom, and considerable electromagnetics explanation we have selected the best phenomenological models of the

mutual coupling.

Chapter 3 presents the phenomenological models of the mutual coupling among the vertical dipoles placed uniformly on a horizontal circle, where the inter-dipole spacing is between 3 λ to 20 λ. We have explained our models in terms of electromagnetic theories and principles. The demonstration of the usefulness of these obtained models for direction-of-arrival (DOA) estimation shows that our proposed models, estimation precisions as well as the mutual coupling were exactly known.

Further, in Chapter 4, we have studied the phenomenological modeling of the mutual coupling for the vertical dipoles on a horizontal circle where the inter-dipole spacing between the dipoles' varying from 0.3 λ to 1.0 λ. These obtained models are considerable with the existing electromagnetic. We have found that our proposed phenomenological models of the mutual coupling provide the estimation precision for the DOA application as like the mutual coupling were known perfectly.

Chapter 5 describes the phenomenological study of the mutual coupling among dipoles oriented radially to the circle's radius. The proposed phenomenological models are reasonable in views of the existing electromagnetic. Also, our obtained phenomenological models are found useful in direction finding, despite these models' few degrees of freedom. The DOA estimation plots of RMSE versus SNR show that the phenomenological model estimation accuracy is almost same as the mutual coupling were precisely computed. Whereas overlooking the mutual coupling reasons a degradation up to a several orders of magnitude.

The contribution of this research will be helpful in carrying out researches for other antenna array configurations in the future. This dissertation serves as an important reference for similar studies in modeling the mutual coupling

or any other phenomena in antenna arrays.

6.2 Future Work

For the future work, the phenomenological study of the mutual coupling among tangential dipoles spaced uniformly on a horizontal circle will investigate.

The geometry of the dipole antennas is shown in figure 6.1,

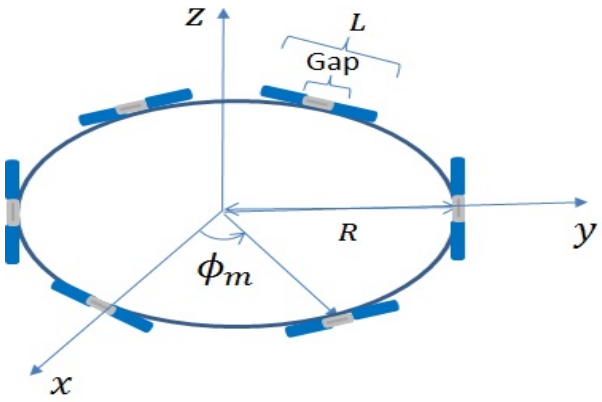

Figure 6.1: The spatial geometry of a circular array of $M = 6$ identical dipoles, spaced uniformly on a circle, but oriented tangentially to the circular plane.

where $\phi_m = \frac{2\pi(m-1)}{M}, (m = 1, 2, ..., M)$ is the angular displacement of each dipole on the horizontal $x - y$ plane, R denotes the radius of the circle, and L is the length of each dipole antenna.

To use the EMCoS antenna VLab computer simulation software we will produce the mutual coupling data by varying (i)the number of antennas (M) in an array, (ii) the cirlce's radius (R), and (iii) the length (L) of each antenna. Then several phenomenological models with unknown coefficients are

proposed based on the data variation of the above trivariates, the unknown coefficients will be optimized by least-squares fitting. Then the best models will select based on the fewness of degrees-of-freedom.

Appendices

Appendix A

Candidate Models for a UCA of Vertical Dioples in Chapter 3

A.1 Candidate Models of the Magnitude of the Self-impedance ($|z_0|$)

No further models have investigated for the magnitude of the self-impedance, because our obtained phenomenological model is explained almost all our VLab data by high R^2 value. The proposed model is also reasonable in terms of electromagnetic.

A.2 Candidate Models of the Phase of the Self-impedance ($\angle z_0$)

A.2.1 2-DoF Model

[1]

with $R^2 = 0.8920$

$$\angle z_0 \;\approxeq\; \beta_1 \cos\left(2\pi\frac{L}{\lambda} + \beta_2\right) \tag{A.1}$$

where

$\beta_1 = 1.7950$,

$\beta_2 = 1.6976$.

This model is not selected as the best model because of the higher number of coefficients.

A.2.2 4-DoF Model

with $R^2 = 0.8966$

$$\angle z_0 \;\approxeq\; \beta_1 \cos\left(\beta_2\frac{L}{\lambda} + \beta_3\right) + \beta_4 \tag{A.2}$$

where

$\beta_1 = 1.7959$,

$\beta_2 = 6.1478$,

[1] DoF is the "Degrees-of-freedom"

$\beta_3 = 1.7897,$

$\beta_4 = -0.0920.$

This model is not selected as the best model because of the higher number of coefficients.

A.2.3 6-DoF Model

with $R^2 = 0.9596$

$$\angle z_0 \approxeq \begin{cases} \beta_1 \left(\frac{L}{\lambda}\right)^{\beta_2} + \beta_3, & \text{for } 0.1 \leq \frac{L}{\lambda} < 0.6 \\ \beta_4 \left(\frac{L}{\lambda}\right)^{\beta_5} + \beta_6, & \text{for } 0.6 \leq \frac{L}{\lambda} \leq 1.0 \end{cases} \tag{A.3}$$

where

$\beta_1 = 88.7448,$

$\beta_2 = 5.5809,$

$\beta_3 = -1.6783,$

$\beta_4 = -1.6970,$

$\beta_5 = 14.6934,$

$\beta_6 = 1.2691.$

Though the goodness of the fit R^2 high, but this model is not selected as the best model because of the higher number of coefficients and as well as not explainable with existing electromagnetic.

A.3 Candidate Models of the Mgnitude of the Mutual Impedance ($|z_m|$)

A.3.1 4-DoF Model

with $R^2 = 0.83547$

$$|z_m| \;\cong\; \left\{\gamma_1 \left(\frac{L}{\lambda}\right)^{\gamma_2} \left(\frac{\lambda}{R}\right)^{\gamma_3} \left(1 - \cos\left(2\pi \frac{m}{M}\right)\right)^{\gamma_4}\right\} \tag{A.4}$$

where

$\gamma_1 = 1710.45$,

$\gamma_2 = 8.80049$,

$\gamma_3 = 0.9392$,

$\gamma_4 = -0.27891$.

This model is not selected as the best model because of the higher number of coefficients.

A.3.2 5-DoF Model-1

with $R^2 = 0.8597$

$$|z_m| \;\cong\; \exp\left\{\gamma_1 - \gamma_2 \log_e\left(\frac{R}{\lambda}\right) + \gamma_3 \log_e\left(\frac{L}{\lambda}\right) + \gamma_3 \log_e\left|\sin\left(\gamma_4\left(\frac{m}{M}\right)\pi + \gamma_5\right)\right|\right\} \tag{A.5}$$

where

$\gamma_1 = 15.9938$,

$\gamma_2 = 0.9998$,

$\gamma_3 = 3.8457,$

$\gamma_4 = -0.0183,$

$\gamma_5 = 0.0978.$

This model is not selected as the best model because of the higher number of coefficients.

A.3.3 5-DoF Model-2

with $R^2 = 0.9737$

$$|z_m| \;\cong\; \exp\left\{\gamma_1 + \gamma_2\left(\frac{L}{\lambda}\right) - \left(\frac{R}{\lambda}\right)^{\gamma_3}\left|\sin\left(\gamma_4\left(\frac{m}{M}\right)\pi + \gamma_5\right)\right|\right\} \qquad \text{(A.6)}$$

where

$\gamma_1 = -1.5817,$

$\gamma_2 = 8.9804,$

$\gamma_3 = 0.4132,$

$\gamma_4 = 0.4455,$

$\gamma_5 = 0.6905.$

This model is not selected as the best model because of the higher number of coefficients and not explainable with existing electromagnetic.

A.4 Candidate Models of the Phase of the Mutual Impedance ($\angle z_m$)

A.4.1 8-DoF Model -1

with $R^2 = 0.7510$

$$\angle z_m \approxeq \left\{\delta_1 - \delta_2 \left(\frac{R}{\lambda}\right)^{\delta_3} \sin\left(\delta_4 \left(\frac{m}{M}\right)\right)\right\} \left\{\frac{1 + \delta_5 \left(\frac{L}{\lambda}\right) + \delta_6 \left(\frac{L}{\lambda}\right)^2}{\delta_7 + \delta_8 \left(\frac{L}{\lambda}\right) + \left(\frac{L}{\lambda}\right)^2}\right\} \quad \text{(A.7)}$$

where

$\delta_1 = 2.3057$,

$\delta_2 = 3.0170$,

$\delta_3 = -0.0087$,

$\delta_4 = 7.2345$,

$\delta_5 = -2.5818$,

$\delta_6 = 1.6862$,

$\delta_7 = 0.6175$,

$\delta_8 = -1.5571$.

This model is not selected as the best model because of the higher number of coefficients and the goodness of fit R^2 is not good enough.

A.4.2 8-DoF Model -2

with $R^2 = 0.7510$

$$\angle z_m \approxeq \left\{\delta_1 - \delta_2 \left(\frac{R}{\lambda}\right)^{0} \sin\left(\delta_3 \left(\frac{m}{M}\right)\right)\right\} \left\{\frac{\delta_4 + \delta_5 \left(\frac{L}{\lambda}\right) + \delta_6 \left(\frac{L}{\lambda}\right)^2}{\delta_7 + \delta_8 \left(\frac{L}{\lambda}\right) + \left(\frac{L}{\lambda}\right)^2}\right\} \quad \text{(A.8)}$$

where

$\delta_1 = 2.1843,$

$\delta_2 = 2.8018,$

$\delta_3 = 7.2344,$

$\delta_4 = 1.0549,$

$\delta_5 = -2.7244,$

$\delta_6 = 1.7799,$

$\delta_7 = 0.6171,$

$\delta_8 = -1.5566.$

This model is not selected as the best model because of the higher number of coefficients and the goodness of fit R^2 is not good enough.

A.4.3 9-DoF Model

with $R^2 = 0.7511$

$$\angle z_m \approxeq \left\{ \delta_1 - \delta_2 \left(\frac{R}{\lambda} \right)^{\delta_3} \sin\left(\delta_4 \left(\frac{m}{M} \right) \right) \right\} \left\{ \frac{\delta_5 + \delta_6 \left(\frac{L}{\lambda} \right) + \delta_7 \left(\frac{L}{\lambda} \right)^2}{\delta_8 + \delta_9 \left(\frac{L}{\lambda} \right) + \left(\frac{L}{\lambda} \right)^2} \right\}. \quad \text{(A.9)}$$

where

$\delta_1 = 2.184,$

$\delta_2 = 2.8580,$

$\delta_3 = -0.0086,$

$\delta_4 = 7.2344,$

$\delta_5 = 1.0555,$

$\delta_6 = -2.7250,$

$\delta_7 = 1.7797,$

$\delta_8 = 0.6175,$

$\delta_9 = -1.5572.$

This model is not selected as the best model because of the higher number of coefficients and the goodness of fit R^2 is not good enough.

Appendix B

Candidate Models for a UCA of Vertical Dioples in Chapter 4

B.1 Candidate Models of the Magnitude of the Self-impedance ($|z_0|$)

B.1.1 3-DoF Model

[1]

with $R^2 = 0.5743$

$$|z_0| \;\approxeq\; \exp\left\{\left|\alpha_1 + \frac{\alpha_2\left(1-\left(\frac{L}{\lambda}\right)^2\right)}{0+\left(\frac{L}{\lambda}-\alpha_4\right)^2}\right|\right\}, \tag{B.1}$$

where

$\alpha_1 = 9.4652$,

[1] DoF is the "Degrees-of-freedom"

$\alpha_2 = -7.8442,$

$\alpha_3 = 1.8081.$

This model is not selected as the best model because of the higher number of coefficients and the goodness of fit R^2 is not good enough.

B.1.2 5-DoF Model-1

with $R^2 = 0.9239$

$$|z_0| \;\approxeq\; \exp\left\{\left|\alpha_1 + \frac{\alpha_2\left(1-\left(\frac{L}{\lambda}\right)^2\right)}{\alpha_3+\left(\frac{L}{\lambda}-\alpha_4\right)^2}\right| + \alpha_5\frac{R}{\lambda}\right\}, \tag{B.2}$$

where

$\alpha_1 = 8.2580,$

$\alpha_2 = -0.1375,$

$\alpha_3 = 0.0294,$

$\alpha_4 = 0.5173,$

$\alpha_5 = 0.1139.$

This model is not selected as the best model because of the higher number of coefficients.

B.1.3 5-DoF Model-2

with $R^2 = 0.9241$

$$|z_0| \;\approxeq\; \exp\left\{\left|\alpha_1 + \frac{\alpha_2\left(1-\left(\frac{L}{\lambda}\right)^2\right)}{\alpha_3+\left(\frac{L}{\lambda}-\alpha_4\right)^2}\right| + \alpha_5 M\right\}, \tag{B.3}$$

where

$\alpha_1 = 8.4943$,

$\alpha_2 = -0.1375$,

$\alpha_3 = 0.0294$,

$\alpha_4 = 0.5173$,

$\alpha_5 = -0.0235$.

This model is not selected as the best model because of the higher number of coefficients and not explainable with existing electromagnetic.

B.1.4 6-DoF Model-1

with $R^2 = 0.9248$

$$|z_0| \;\approxeq\; \exp\left\{\left|\alpha_1 + \frac{\alpha_2\left(1-\left(\frac{L}{\lambda}\right)^2\right)}{\alpha_3 + \left(\frac{L}{\lambda}-\alpha_4\right)^2}\right| + \alpha_5 M + \alpha_6\left(\frac{R}{\lambda}\right)\right\}, \qquad \text{(B.4)}$$

where

$\alpha_1 = 8.4222$,

$\alpha_2 = -0.1375$,

$\alpha_3 = 0.0294$,

$\alpha_4 = 0.5173$,

$\alpha_5 = -0.0234$,

$\alpha_6 = 0.1139$.

This model is not selected as the best model because of the higher number of coefficients and not easy to explain by existing electromagnetic.

B.1.5 6-DoF Model-2

with $R^2 = 0.9249$

$$|z_0| \;\approxeq\; \exp\left\{\left|\alpha_1 + \frac{\alpha_2\left(1-\left(\frac{L}{\lambda}\right)^2\right)}{\alpha_3+\left(\frac{L}{\lambda}-\alpha_4\right)^2}\right|\right\}(M)^{\alpha_5}\left(\frac{R}{\lambda}\right)^{\alpha_6}, \tag{B.5}$$

where

$\alpha_1 = 8.6765,$

$\alpha_2 = -0.1375,$

$\alpha_3 = 0.0294,$

$\alpha_4 = 0.5173,$

$\alpha_5 = -0.1593,$

$\alpha_6 = 0.0714.$

This model is not selected as the best model because of the higher number of coefficients and not explainable with existing electromagnetic.

B.2 Candidate Models of the Phase of the Self-impedance ($\angle z_0$)

B.2.1 2-DoF Model

with $R^2 = 0.8591$

$$\angle z_0 \;\approxeq\; -\beta_1 \sin\left(2\pi\frac{L}{\lambda}\right) e^{\left(-\beta_2 \frac{R}{\lambda}\right)}, \tag{B.6}$$

where

$\beta_1 = 1.8314$,

$\beta_2 = 0.0561$.

This model is not selected as the best model because of the higher number of coefficients and not explainable with existing electromagnetic.

B.2.2 3-DoF Model-1

with $R^2 = 0.8648$

$$\angle z_0 \;\approxeq\; \beta_1 + \beta_2 \sin\left(2\pi\frac{L}{\lambda}\right) e^{\left(-\beta_3 \frac{R}{\lambda}\right)}, \tag{B.7}$$

where

$\beta_1 = -0.0943$,

$\beta_2 = -1.8315$,

$\beta_3 = 0.0561$.

This model is not selected as the best model because of the higher number of coefficients and not explainable with existing electromagnetic.

B.2.3 3-DoF Model-2

with $R^2 = 0.8646$

$$\angle z_0 \approx \beta_1 M + \beta_2 \sin\left(2\pi\frac{L}{\lambda}\right) e^{\left(-\beta_3 \frac{R}{\lambda}\right)}, \tag{B.8}$$

where

$\beta_1 = -0.0128$,

$\beta_2 = -1.8315$,

$\beta_3 = 0.0561$.

This model is not selected as the best model because of the higher number of coefficients and not explainable with existing electromagnetic.

B.2.4 3-DoF Model-3

with $R^2 = 0.8662$

$$\angle z_0 \approx \beta_1 M + \beta_2 \frac{R}{\lambda} + \beta_3 \sin\left(2\pi\frac{L}{\lambda}\right), \tag{B.9}$$

where

$\beta_1 = 0.0013$,

$\beta_2 = -0.1644$,

$\beta_3 = -1.7678$.

This model is not selected as the best model because of the higher number of coefficients and not explainable with existing electromagnetic.

B.3 Candidate Models of the Magnitude of the Mutual Impedance ($|z_m|$)

B.3.1 3-DoF Model-1

with $R^2 = 0.6431$

$$|z_m| \approx \left\{ \gamma_1 \left(\frac{L}{\lambda}\right)^{\gamma_2} \left(\frac{\lambda}{R}\right) \left(1 - \cos\left(2\pi \frac{m}{M}\right)\right)^{\gamma_3} \right\}, \tag{B.10}$$

where

$\gamma_1 = 1284.38$,

$\gamma_2 = 10.32$,

$\gamma_3 = 0.213$.

This model is not selected as the best model because of the goodness of the fit R^2 is low.

B.3.2 3-DoF Model-2

with $R^2 = 0.8159$

$$|z_m| \approx \left\{ 10^{\gamma_1} \left(\frac{R}{\lambda}\right)^{-\gamma_2} \left(\frac{L}{\lambda}\right)^{\gamma_3} \left|\left(\sin\left(2\pi \frac{m}{M}\right)\right)\right| \right\}, \tag{B.11}$$

where

$\gamma_1 = 2.5778$,

$\gamma_2 = 0.8806$,

$\gamma_3 = 3.2165$.

This model is not selected as the best model because of the goodness of the fit R^2 is low.

B.3.3 4-DoF Model-1

with $R^2 = 0.8159$

$$|z_m| \approxeq \left\{ 10^{\gamma_1} \left(\frac{R}{\lambda}\right)^{-\gamma_2} \left(\frac{L}{\lambda}\right)^{\gamma_3} \left| \left(\sin\left(2\pi \frac{m}{M} + \gamma_4 \right) \right) \right| \right\}, \quad \text{(B.12)}$$

where

$\gamma_1 = 2.5778,$

$\gamma_2 = 0.8805,$

$\gamma_3 = 3.2165,$

$\gamma_4 = 3.1415.$

This model is not selected as the best model because of the goodness of the fit R^2 is low.

B.3.4 4-DoF Model-2

with $R^2 = 0.7917$

$$|z_m| \approxeq \left\{ 10^{\gamma_1} \left(\frac{R}{\lambda}\right)^{-\gamma_2} \left(\frac{L}{\lambda}\right)^{\gamma_3} \left| \left(\sin\left(\pi \frac{m}{M} + \gamma_4 \right) \right) \right| \right\}, \quad \text{(B.13)}$$

where

$\gamma_1 = 2.5105,$

$\gamma_2 = 0.8806,$

$\gamma_3 = 3.2165$,

$\gamma_4 = 3.3791$.

This model is not selected as the best model because of the goodness of the fit R^2 is low.

B.3.5 4-DoF Model-3

with $R^2 = 0.6527$

$$|z_m| \approx \left\{ \gamma_1 \left(\frac{L}{\lambda}\right)^{\gamma_2} \left(\frac{L}{\lambda}\right)^{\gamma_3} \left(1 - \cos\left(2\pi \frac{m}{M}\right)\right)^{\gamma_4} \right\}, \qquad \text{(B.14)}$$

where

$\gamma_1 = 1713.98$,

$\gamma_2 = 10.376$,

$\gamma_3 = 0.7135$,

$\gamma_4 = 0.1595$.

This model is not selected as the best model because of the goodness of the fit R^2 is low.

B.3.6 4-DoF Model-4

with $R^2 = 0.8305$

$$|z_m| \approx \left\{ 10^{\gamma_1} \left(\frac{R}{\lambda}\right)^{-\gamma_2} \left(\frac{L}{\lambda}\right)^{\gamma_3} \left| \left(\sin\left(2\pi \frac{m}{M}\right)\right)^{\gamma_4} \right| \right\}, \qquad \text{(B.15)}$$

where

$\gamma_1 = 2.4413,$

$\gamma_2 = 0.8806,$

$\gamma_3 = 3.2165,$

$\gamma_4 = 0.2106.$

This model is not selected as the best model because of the goodness of the fit R^2 is low.

B.4 Candidate Models of the Phase of the Mutual Impedance ($\angle z_m$)

B.4.1 4-DoF Model

with $R^2 = 0.4348$

$$\angle z_m \approxeq \delta_1 \left(\frac{L}{\lambda}\right)^{\delta_2} \left(\frac{\lambda}{R}\right)^{\delta_3} \left(1 - \cos\left(2\pi \frac{m}{M}\right)\right)^{\delta_4} \tag{B.16}$$

where

$\delta_1 = 4.8312,$

$\delta_2 = 1.7099,$

$\delta_3 = -0.0097,$

$\delta_4 = 0.1994.$

This model is not selected as the best model because of the goodness of the fit R^2 is low.

B.4.2 5-DoF Model-1

with $R^2 = 0.3640$

$$\angle z_m \;\approxeq\; \delta_1 + \delta_2 \frac{L}{\lambda} + \delta_3 \left(\frac{R}{\lambda}\right)^{\delta_4} \sin\left(\delta_5 \frac{m}{M}\right), \tag{B.17}$$

where

$\delta_1 = 4.6712$,

$\delta_2 = -3.7136$,

$\delta_3 = -3.0852$,

$\delta_4 = 0.0008$,

$\delta_5 = 3.4861$.

This model is not selected as the best model because of the goodness of the fit R^2 is low.

B.4.3 5-DoF Model-2

with $R^2 = 0.3640$

$$\angle z_m \;\approxeq\; \delta_1 + \delta_2 \frac{L}{\lambda} + \delta_3 \sin\left(\delta_4 \frac{m}{M}\right) e^{-\delta_5\left(\frac{R}{\lambda}\right)}, \tag{B.18}$$

where

$\delta_1 = 4.6712$,

$\delta_2 = -3.7137$,

$\delta_3 = 3.0822$,

$\delta_4 = -3.4861$,

$\delta_5 = -0.0008$.

This model is not selected as the best model because of the goodness of the fit R^2 is low.

B.4.4 6-DoF Model-1

with $R^2 = 0.3771$

$$\angle z_m \approx \delta_1 + \delta_2 \sin\left(\delta_3 \frac{L}{\lambda}\right) + \delta_4 \left(\frac{R}{\lambda}\right)^{\delta_5} \sin\left(\delta_6 \frac{m}{M}\right), \qquad \text{(B.19)}$$

where

$\delta_1 = 2.4093,$

$\delta_2 = -1.4120,$

$\delta_3 = -4.9843,$

$\delta_4 = 3.0852,$

$\delta_5 = 0.0008,$

$\delta_6 = -3.4861.$

This model is not selected as the best model because of the goodness of the fit R^2 is low.

B.4.5 6-DoF Model-2

with $R^2 = 0.3641$

$$\angle z_m \approx \left\{\delta_1 - \delta_2 \left(\frac{R}{\lambda}\right)^{\delta_3} \sin\left(\delta_4 \frac{m}{M} + \delta_5\right)\right\} + \delta_6 \left(\frac{L}{\lambda}\right), \qquad \text{(B.20)}$$

where

$\delta_1 = 3.2455,$

$\delta_2 = 1.6872,$

$\delta_3 = 0.0031,$

$\delta_4 = -5.0679,$

$\delta_5 = 79.2323,$

$\delta_6 = -3.7136.$

This model is not selected as the best model because of the goodness of the fit R^2 is low.

B.4.6 6-DoF Model-3

with $R^2 = 0.4914$

$$\angle z_m \approx \left\{ \delta_1 - \delta_2 \left(\frac{R}{\lambda} \right)^{\delta_3} \sin\left(\pi \left(\frac{m}{M} \right) \right) \right\} \left\{ \frac{1 + \delta_4 \left(\frac{L}{\lambda} \right) + \delta_5 \left(\frac{L}{\lambda} \right)^2}{\delta_6 + \delta_7 \left(\frac{L}{\lambda} \right) + \left(\frac{L}{\lambda} \right)^2} \right\}, \quad \text{(B.21)}$$

where

$\delta_1 = 0.3629,$

$\delta_2 = -0.3022,$

$\delta_3 = 0.0203,$

$\delta_4 = 1.1417,$

$\delta_5 = -2.4799,$

$\delta_6 = 1.3267,$

$\delta_7 = -2.3719.$

This model is not selected as the best model because of the goodness of the fit R^2 is low.

B.4.7 6-DoF Model-4

with $R^2 = 0.3698$

$$\angle z_m \approx \delta_1 + \delta_2 \sin\left(\delta_3 \frac{L}{\lambda} + \delta_4 \right) + \delta_5 \left(\frac{R}{\lambda} \right)^{\delta_6} \sin\left(\pi \frac{m}{M} \right), \quad \text{(B.22)}$$

where

$\delta_1 = 2.2255,$

$\delta_2 = 1.5262,$

$\delta_3 = -3.7769,$

$\delta_4 = 2.4828,$

$\delta_5 = -3.0255,$

$\delta_6 = 0.0007.$

This model is not selected as the best model because of the goodness of the fit R^2 is low.

Appendix C

Candidate Models for a UCA of Radial Dioples in Chapter 5

C.1 Candidate Models of the Magnitude of the Self-impedance ($|z_0|$)

No further models have investigated for the magnitude of the self-impedance, because our obtained phenomenological model is explained almost all our VLab data by high R^2 value. The proposed model is also reasonable in terms of electromagnetic.

C.2 Candidate Models of the Phase of the Self-impedance ($\angle z_0$)

C.2.1 2-DoF Model

[1]

with $R^2 = 0.8950$

$$\angle z_0 \approx \beta_1 \sin\left(2\pi\frac{L}{\lambda} + \beta_2\right), \tag{C.1}$$

where

$\beta_1 = -1.7563$,

$\beta_2 = 0.1116$.This model is not selected as the best model because of the higher number of coefficients

C.2.2 3-DoF Model

with $R^2 = 0.8968$

$$\angle z_0 \approx \beta_1 \sin\left(\beta_2\frac{L}{\lambda} + \beta_3\right), \tag{C.2}$$

where

$\beta_1 = -1.7563$,

$\beta_2 = 6.4316$,

$\beta_3 = 0.0283$.

This model is not selected as the best model because of the higher number of coefficients

[1] DoF is the "Degrees-of-freedom"

C.3 Candidate Models of the Magnitude of the Mutual Impedance ($|z_m|$)

C.3.1 3-DoF Model-1

with $R^2 = 0.7470$

$$|z_m| \approx \left\{ 10^{\gamma_1} \left(\frac{L}{\lambda}\right)^{\gamma_2} \left(\frac{R}{\lambda}\right) \left(1 - \cos\left(2\pi \frac{m}{M}\right)\right)^{\gamma_3} \right\}, \tag{C.3}$$

where

$\gamma_1 = 2.0301$,

$\gamma_2 = 2.833$,

$\gamma_3 = -1.3020$.

This model is not selected as the best model because of the goodness of the fit R^2 is low.

C.3.2 3-DoF Model-2

with $R^2 = 0.7447$

$$|z_m| \approx \left\{ 10^{\gamma_1} \left(\frac{R}{\lambda}\right)^{-\gamma_2} \left(\frac{L}{\lambda}\right)^{\gamma_3} \left|\left(\sin\left(2\pi \frac{m}{M}\right)\right)\right| \right\}, \tag{C.4}$$

where

$\gamma_1 = 1.8246$,

$\gamma_2 = 1.5394$,

$\gamma_3 = 2.8833$.

This model is not selected as the best model because of the goodness of the fit R^2 is low.

C.3.3 4-DoF Model

with $R^2 = 0.7508$

$$|z_m| \approx \left\{ 10^{\gamma_1} \left(\frac{R}{\lambda}\right)^{-\gamma_2} \left(\frac{L}{\lambda}\right)^{\gamma_3} \left| \left(\sin\left(2\pi \frac{m}{M}\right)\right)^{\gamma_4} \right| \right\}, \tag{C.5}$$

where

$\gamma_1 = 1.9112$,

$\gamma_2 = 1.5394$,

$\gamma_3 = 2.8834$,

$\gamma_4 = 1.5012$.

This model is not selected as the best model because of the goodness of the fit R^2 is low.

C.4 Candidate Models of the Phase of the Mutual Impedance ($\angle z_m$)

C.4.1 2-DoF Model

with $R^2 = 0.3762$

$$\angle z_m \approx \delta_1 \frac{L}{\lambda} + \delta_2 \frac{R}{\lambda} + 2\pi \sin\left(\frac{m}{M}\right) \tag{C.6}$$

where

$\delta_1 = 3.9685$,

$\delta_2 = -5.9662$.

This model is not selected as the best model because of the goodness of the fit R^2 is low.

C.4.2 3-DoF Model-1

with $R^2 = 0.6507$

$$\angle z_m \approx \delta_1 \frac{L}{\lambda} + \delta_2 \frac{R}{\lambda} + 2\pi \sin\left(\frac{m}{M} + \delta_3\right), \tag{C.7}$$

where

$\delta_1 = 2.3875$,

$\delta_2 = -9.6182$,

$\delta_3 = 7.3032$.

This model is not selected as the best model because of the goodness of the fit R^2 is low.

C.4.3 3-DoF Model-2

with $R^2 = 0.3793$

$$\angle z_m \approx \delta_1 \frac{L}{\lambda} + \delta_2 \frac{R}{\lambda} + \delta_3 \sin\left(\frac{m}{M}\right), \tag{C.8}$$

where $\delta_1 = 4.0957$, $\delta_2 = -5.6722$, $\delta_3 = 5.4376$.
This model is not selected as the best model because of the goodness of the fit R^2 is low.

C.4.4 4-DoF Model-1

with $R^2 = 0.6836$

$$\angle z_m \approx \delta_1 \frac{L}{\lambda} + \delta_2 \frac{R}{\lambda} + \delta_3 \sin\left(\frac{m}{M} + \delta_4\right), \tag{C.9}$$

where
$\delta_1 = 1.4388$,
$\delta_2 = -11.8098$,
$\delta_3 = 8.6944$,
$\delta_4 = 0.9887$.
This model is not selected as the best model because of the goodness of the fit R^2 is low.

C.4.5 4-DoF Model-2

with $R^2 = 0.6842$

$$\angle z_m \;\approxeq\; \delta_1 + \delta_2 \frac{L}{\lambda} + \delta_3 \frac{R}{\lambda} + 2\pi \sin\left(\frac{m}{M} + \delta_4\right), \tag{C.10}$$

where

$\delta_1 = 2.4303$,

$\delta_2 = 1.4260$,

$\delta_3 = -11.8392$,

$\delta_4 = 7.2130$.

This model is not selected as the best model because of the goodness of the fit R^2 is low.

C.4.6 4-DoF Model-3

with $R^2 = 0.6814$

$$\angle z_m \;\approxeq\; \delta_1 + \delta_2 \frac{L}{\lambda} + \delta_3 \frac{R}{\lambda} + \delta_4 \left(1 - \cos(\frac{m}{M})\right), \tag{C.11}$$

where

$\delta_1 = 8.1466$,

$\delta_2 = 1.4261$,

$\delta_3 = -11.8392$,

$\delta_4 = 2.6439$.

This model is not selected as the best model because of the goodness of the fit R^2 is low.

C.4.7 5-DoF Model

with $R^2 = 0.6843$

$$\angle z_m \;\; \approxeq \;\; \delta_1 + \delta_2 \frac{L}{\lambda} + \delta_3 \frac{R}{\lambda} + \delta_4 \sin\left(\frac{m}{M} + \delta_5\right), \qquad \text{(C.12)}$$

where

$\delta_1 = 3.5718$,

$\delta_2 = 1.4261$,

$\delta_3 = -11.8392$,

$\delta_4 = 5.1475$,

$\delta_5 = 0.8835$.

This model is not selected as the best model because of the higher number of coefficients and the goodness of the fit R^2 is low.

Appendix D

D.1 Graphical view of the magnitude of the Mutual impedance ($|z_m|$) in Chapter 3

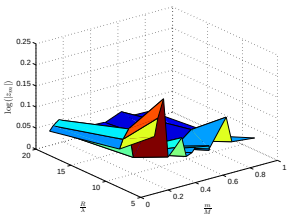

Figure D.1: $\log(|z_m|)$ at $\frac{L}{\lambda} = 0.1$.

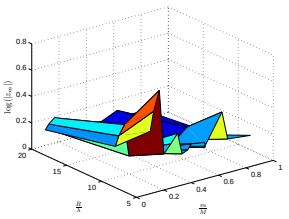

Figure D.2: $\log(|z_m|)$ at $\frac{L}{\lambda} = 0.2$.

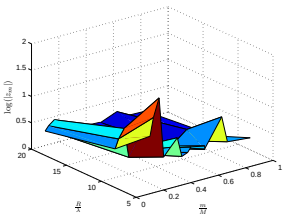

Figure D.3: $\log(|z_m|)$ at $\frac{L}{\lambda} = 0.3$.

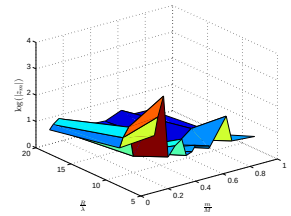

Figure D.4: $\log(|z_m|)$ at $\frac{L}{\lambda} = 0.4$.

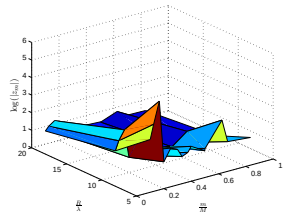

Figure D.5: $\log(|z_m|)$ at $\frac{L}{\lambda} = 0.45$.

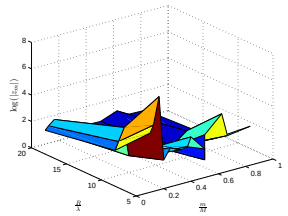

Figure D.6: $\log(|z_m|)$ at $\frac{L}{\lambda} = 0.5$.

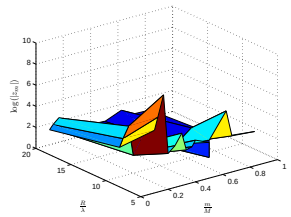

Figure D.7: $\log(|z_m|)$ at $\frac{L}{\lambda} = 0.55$.

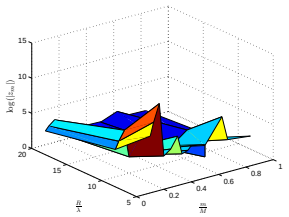

Figure D.8: $\log(|z_m|)$ at $\frac{L}{\lambda} = 0.6$.

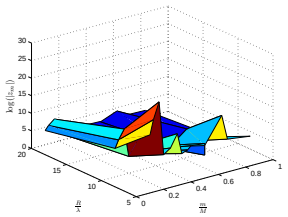

Figure D.9: $\log(|z_m|)$ at $\frac{L}{\lambda} = 0.7$.

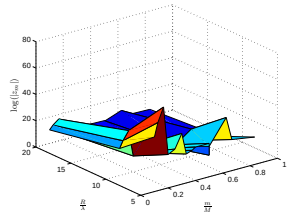

Figure D.10: $\log(|z_m|)$ at $\frac{L}{\lambda} = 0.8$.

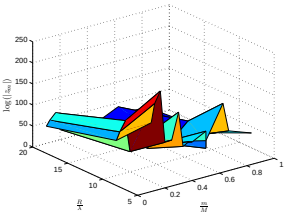

Figure D.11: $\log(|z_m|)$ at $\frac{L}{\lambda} = 0.9$.

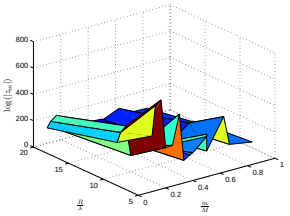

Figure D.12: $\log(|z_m|)$ at $\frac{L}{\lambda} = 1.0$.

D.2 RMSE

According to our DOA estimation the expression of root mean square error (RMSE) is

$$RMSE(\theta) = \sqrt{\frac{\sum_{l=1}^{L}\sum_{i=1}^{K}\left(\hat{\theta}_{il}-\theta_i\right)^2}{KL}} \tag{D.1}$$

Where $\hat{\theta}_{il}$ is the estimate of θ_i in the Lth Monte Carlo experiment. K is the number of imping signal on the array and L is the number of Monte Carlo run.

D.3 More simulation results of "intuitive" model in (1.4)

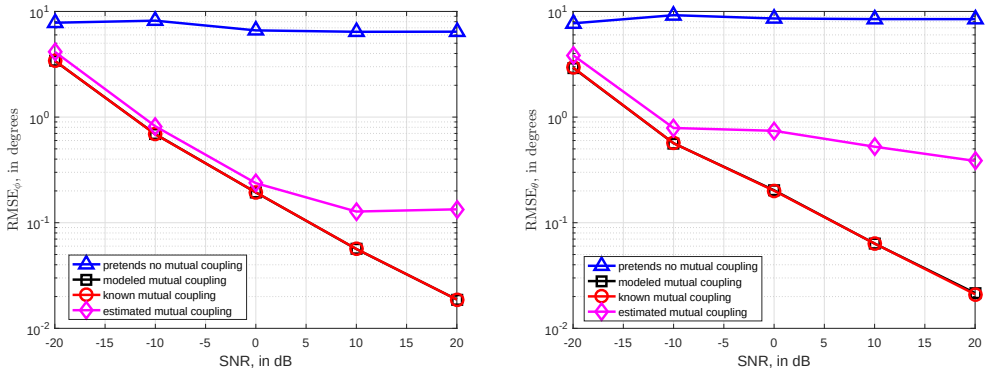

(a) (b)

Figure D.13: RMSE versus SNR at $\frac{L}{\lambda} = 0.4$, $M = 6$, $\frac{R}{\lambda} = 5$, and $(\phi, \theta) = (30^0, 45^0)$: 180 snapshots, 100 Monte Carlo trials

.

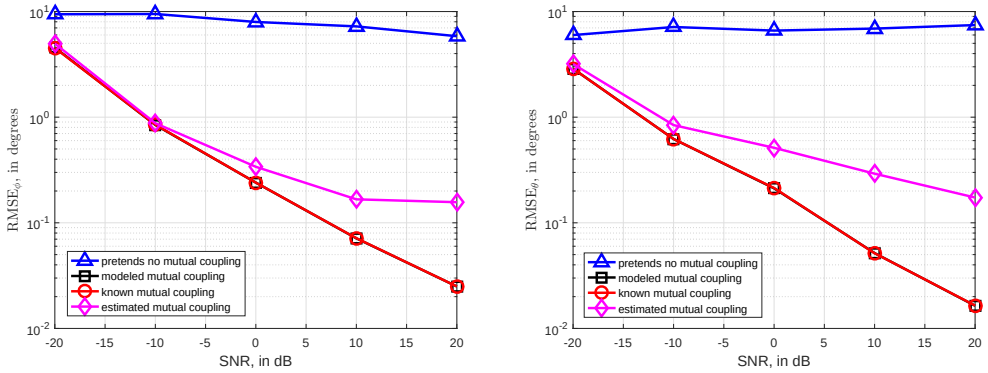

(a) (b)

Figure D.14: RMSE versus SNR at $\frac{L}{\lambda} = 0.4$, $M = 8$, $\frac{R}{\lambda} = 5$, and $(\phi, \theta) = (45^0, 35^0)$: 180 snapshots, 100 Monte Carlo trials

.

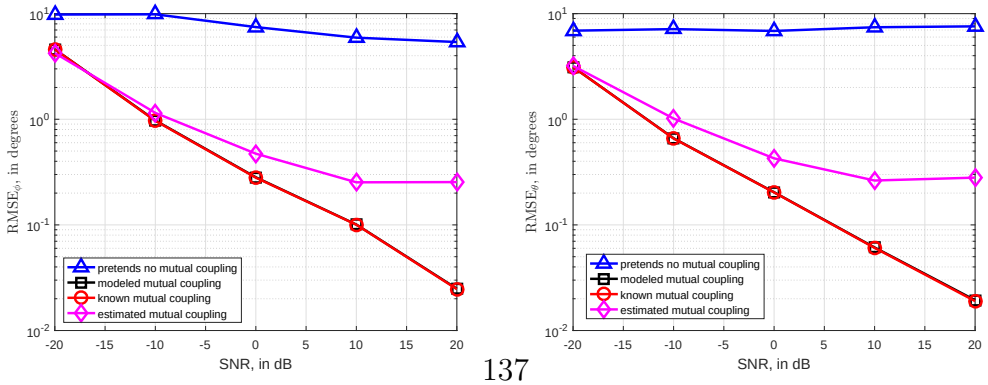

(a) (b)

Figure D.15: RMSE versus SNR at $\frac{L}{\lambda} = 0.55$, $M = 8$, $\frac{R}{\lambda} = 5$, and $(\phi, \theta) = (45^0, 35^0)$: 180 snapshots, 100 Monte Carlo trials

.

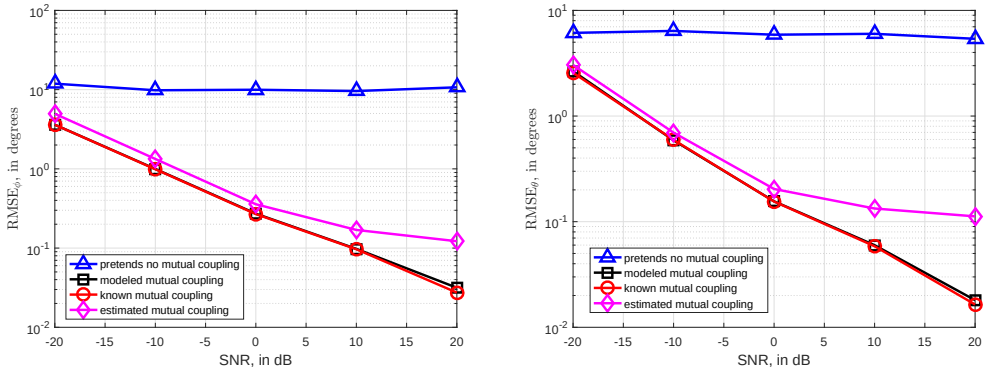

(a) (b)

Figure D.16: RMSE versus SNR at $\frac{L}{\lambda} = 0.6$, $M = 10$, $\frac{R}{\lambda} = 5$, and $(\phi, \theta) = (45^0, 30^0)$: 180 snapshots, 100 Monte Carlo trials

.

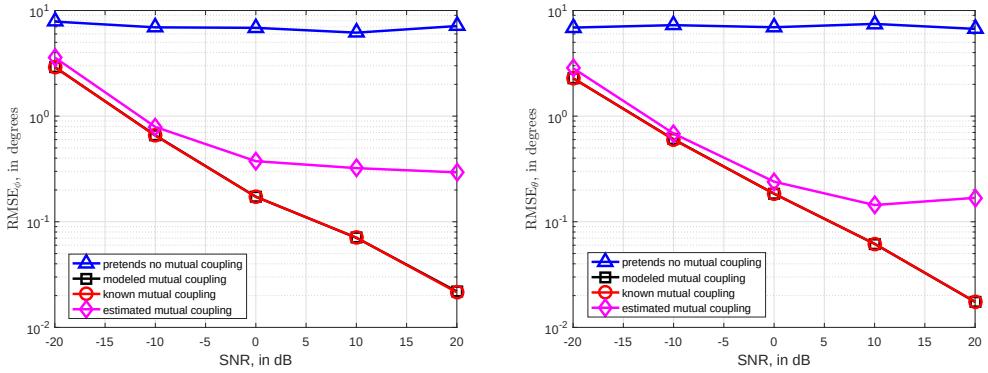

(a) (b)

Figure D.17: RMSE versus SNR at $\frac{L}{\lambda} = 0.7$, $M = 10$, $\frac{R}{\lambda} = 5$, and $(\phi, \theta) = (30^0, 45^0)$: 180 snapshots, 100 Monte Carlo trials

.

Bibliography

[1] IROS JSC, "ARCHAI-I: stationary measuring radio monitoring and direction finding station," web page accessed on February 02, 2018: $http : www.ircos.ru/en/stn_sp.html$.

[2] CHRISTINA TER-MATEVOSYAN, "Round-the-clock radio navigation, security and unauthorized sources of radiation detection," web page accessed on February 10, 2018: $http : //nyut.am/?p = 142495\&l = en$.

[3] F. Tefiku & C. A. Grimes, "Coupling between elements of electrically small compound antennas," *Microwave and Optical Technology Letters*, vol. 22, no. 1, pp. 16–21, 1999.

[4] J. Nagar, B. Q. Lu, M. F. Pantoja & D. H. Werner, "Analytical Expressions for the Mutual Coupling of Loop Antennas Valid From the RF to Optical Regimes," *IEEE Transactions on Antennas and Propagation*, vol. 65, no. 12, pp. 6889–6902, 2017.

[5] O. G. Vendik & D. S. Kozlov, "A Novel Method for the Mutual Coupling Calculation Between Antenna Array Radiators," *IEEE Transactions on Antennas and Propagation*, vol. 57, no. 06, pp. 16–21, 2015.

[6] J. C. Huang, Y. W. Shi & J. W. Tao, "Closed-form estimation of DOA and polarization for multisource with a uniform circular array," *Inter-*

national Conference on Machine Learning and Cybernetics, vol. 7, pp. 4469–4474, 2005.

[7] T. Jun, T. Yantao, C. Wei & Y. Mao, "DOA estimation algorithm of scattered sources based on polarization sensitive sensor array," *Chinese Journal of Scientific Instrument*, vol. 31, no. 6, pp. 1224–1233, 2010.

[8] Y. Wang & Y. Wu, "Direction and polarization estimation using quaternion and polarization rotation matrix," *IEEE Symposium on Electrical & Electronics Engineering*, pp. 319–322, 2012.

[9] L. Wang, G. Wang & Z. Chen, "Joint DOA-polarization estimation based on uniform concentric circular array," *Journal of Electromagnetic Waves and Propagation*, vol. 27, no. 13, pp. 1702–1714, 2013.

[10] H. L. Van Trees, "Optimum Array Processing: Part IV of Detection, Estimation, and Modulation Theory," *John Wiley and Sons*, 2002.

[11] C. A. Balanis, "Antenna Theory, Analysis and Design," *John Wiley and Sons*, 2005.

[12] B. Allen & M. Ghavami, "Adaptive array systems," *John Wiley and Sons*, 2005.

[13] R. L. Haupt, "Antenna Arrays," *John Wiley and Sons*, 2010.

[14] R. C. Hansen, "Phased Array Antenna," *John Wiley and Sons*, 2009.

[15] D. M. Pozar, "Microwave Engineering," *John Wiley and Sons*, 2005.

[16] W. D. Rawle, "The method of moments: A numerical technique for wire antenna design," *High Frequency Electronics 5*, pp. 42–47, 2006.

[17] B. Hamdi, T. Aguili1, N. Raveu & H. Baudrand, "Calculation of the Mutual Coupling Parameters and Their Effects in 1-D Planar Almost Periodic Structures," *Progress In Electromagnetics Research B*, vol. 59, pp. 269–289, 2014.

[18] M. S. Akyz, V. B. Ertrk & M. Kalfa, "Closed-Form Greens Function Representations for Mutual Coupling Calculations Between Apertures on a Perfect Electric Conductor Circular Cylinder Covered With Dielectric Layers," *IEEE Transactions on Antennas and Propagation*, vol. 59, no. 8, pp. 3094–3098, 2011.

[19] S. Khan, "Direction Finding and Polarization Estimation, using Electrically Long Dipoles or Electrically Large Loops," Ph.D Dissertation, *The Hong Kong Polytechnic University, Hong Kong*, 2018.

[20] T. Aksoy & T. E. Tuncer, "Sectorized approach and measurement reduction for mutual coupling calibration of non-omnidirectional antenna arrays," *Radio Science*, vol. 48, no. 2, pp. 102–110, 2013.

[21] T. Aksoy & T. E. Tuncer, "Measurement reduction for mutual coupling calibration in DOA estimation," *Radio Science*, vol. 47, no. 3, pp. RS3004, 2012.

[22] L. Shuai, H. Chen & C. Haixia, "DOA estimation of coherent signals on uniform circular array in the presence of mutual coupling," *International Conference on Communication Software and Networks (ICCSN)*, pp. 86-90, 2016.

[23] J. Bao, Q. Wang, X. Dou, G. Liu, P. Shi & X. Wei, "A new wideband mutual coupling compensation method for adaptive arrays based on cu-

bic Hermite interpolation," *Progress In Electromagnetics Research*, vol. 44, pp. 161–170, 2015.

[24] S. Cai, "Improved rare methods for DOA estimation in uniform circular arrays with unknown mutual coupling," *Statistical Signal Processing Workshop (SSP)*, pp. 1–5, 2016.

[25] S. Caylar, K. Leblebicioglu & G. Dural, 'A neural network method for direction of arrival estimation with Uniform circular dipole array in the presence of mutual coupling," *International Conference on Recent Advances in Space Technologies*, pp. 537–540, 2007.

[26] J. Dai, X. Bao, N. Hu, C. Chang & W. Xu, "A recursive RARE algorithm for DOA estimation with unknown mutual coupling," *IEEE Antennas and Wireless Propagation Letters*, vol. 13, pp. 1593–1596, 2014.

[27] K. L. Du, "Pattern analysis of uniform circular array," *IEEE Transactions on Antennas and Propagation*, vol. 52, no. 4, pp. 1125–1129, 2004.

[28] W. Du, D. Su, S. Xie & H. T. Hon, "A fast calculation method for the receiving mutual impedances of uniform circular arrays," *IEEE Antennas and Wireless Propagation Letters*, vol. 11, pp. 893–896, 2012.

[29] A. M. Elbir & T. E. Tuncer, "Sparse support recovery for DOA estimation in the presence of mutual coupling," *European Signal Processing Conference (EUSIPCO)*, pp. 1366–1370, 2015.

[30] T. Filik & T. E. Tuncer, "A fast and automatically paired 2-D direction-of-arrival estimation with and without estimating the mutual coupling coefficients," *Radio Science*, vol. 45, no. 3, pp. RS3009, 2010.

[31] T. S. Ghazaany, S. Zhu, S. M. R. Jones, R. A. Alhameed, J. M. Noras, T. V. Buren & S. Marker, "Effect of different platforms on coupling compensation matrices in AOA estimation algorithms using small size UCA," *IEEE Radio and Wireless Symposium (RWS)*, pp. 277–279, 2014.

[32] R. Goossens & H. Rogier, "A hybrid UCA-RARE/Root-MUSIC approach for 2-D direction of arrival estimation in uniform circular arrays in the presence of mutual couplings," *IEEE Transactions on Antennas and Propagation*, vol. 55, no. 3, pp. 841–849, 2007.

[33] R. Goossens & H. Rogier, "2-D direction of arrival estimation combining UCA-RARE and MUSIC for uniform circular arrays subject to mutual coupling," *Proceedings of the Joint 9th International Conference on Electromagnetics in Advanced Applications and the 11th European Electromagnetic Structures Conference (ICEAA-EESC)*, pp. 791–794, 2005.

[34] M. Grossmann, V. Ramireddy, K. Jonas, M. Landmann, G. D. Galdo, R. Florian & R. Perthold, "Antenna array optimization strategies for robust direction finding," *European Conference on Antennas and Propagation (EuCAP)*, pp. 1–5, 2016.

[35] I. J. Gupta & A. A. Ksienski, "Effect of mutual coupling on the performance of adaptive arrays," *IEEE Transactions on Antennas and Propagation*, vol. 31, no. 5, pp. 785–791, 1983.

[36] P. Hajiani & M. Hakkak, "Direction finding with compensation of mutual coupling based on Complex fast ICA in circular array antenna," *International Conference on Software, Telecommunications and Computer Networks*, pp. 51–54, 2008.

[37] C. W. Harrison, 'Symmetrical antenna arrays," *Proceedings of the IRE*, vol. 33, no. 12, pp. 892–896, 1945.

[38] Z. Huang, C. A. Balanis & C. R. Birtcher, "Mutual coupling compensation in UCAs: simulations and experiment," *IEEE Transactions on Antennas and Propagation*, vol. 54, no. 11, pp. 3082–3086, 2006.

[39] T. Huang & A. S. Mohan, "Effects of array mutual coupling on near-field DOA estimation," *Canadian Conference on Electrical and Computer Engineering,(CCECE)*, vol. 3, pp. 1881–1884, 2003.

[40] H. T. Hui, "Compensating for the mutual coupling effect in direction finding based on a new calculation method for mutual impedance," *IEEE Antennas and Wireless Propagation Letters*, vol. 2, no. 1, pp. 26–29, 2003.

[41] P. Ioannides & C. A. Balanis, "Mutual coupling in adaptive circular arrays," *Antennas and Propagation Society International Symposium*, vol. 1, pp. 403–406, 2004.

[42] Z. Jianhua, X. Hong & Y. Jianping, "Analysis of the dipole circular array in interferometric direction-finding system," *International Symposium on Antennas, Propagation and EM Theory (ISAPE)*, pp. 255–260, 2000.

[43] A. Khallaayoun, R. J. Weber & Y. Huang, "A blind iterative calibration method for high resolution DoA estimation," *Military Communications Conference*, pp. 199–204, 2011.

[44] M. Lin & L. Yang, "Blind calibration and DOA estimation with uniform circular arrays in the presence of mutual coupling," *IEEE Antennas and Wireless Propagation Letters*, vol. 5, no. 1, pp. 315–318, 2006.

[45] M. Lin, Z. Gong & L. Yang, "A method for DOA estimation with mutual coupling present," *International Symposium on Microwave, Antenna, Propagation and EMC Technologies for Wireless Communications*, vol. 2, pp. 996–999, 2005.

[46] S. Liu, L. Yang & S. Yang, "Robust joint calibration of mutual coupling and channel gain/phase inconsistency for uniform circular array," *IEEE Antennas and Wireless Propagation Letters*, vol. 15, pp. 1191–1195, 2016.

[47] S. Liu, L. Yang, S. Yang, Q. Jiang & H. Wu, 'Blind direction-of-arrival estimation with uniform circular array in presence of mutual coupling," *International Journal of Antennas and Propagation*, vol. 2016, 2016.

[48] P. Ioannides & C. A. Balanis, "Uniform circular arrays for smart antennas," *IEEE Antennas and propagation magazine*, vol. 47, no. 4, pp. 192–206, 2005.

[49] H. S. Lui & H. T. Hui, "Improved mutual coupling compensation in compact antenna arrays," *IET microwaves, antennas and propagation*, vol. 4, no. 10, pp. 1506–1516, 2010.

[50] H. S. Lui & H. T. Hui, "Effective mutual coupling compensation for direction-of-arrival estimations using a new, accurate determination method for the receiving mutual impedance," *Journal of Electromagnetic Waves and Applications*, vol. 24, no. 2-3, pp. 271–281, 2010.

[51] F. Marie, M. Oger, D. Lemur, Y. Erhel, G. L. Bouter, L. Bertel & C. Brousseau, "A low complexity method for HF direction finding," *Electronics Letters*, vol. 42, no. 21, pp. 1194–1196, 2006.

[52] A. Mirkamali, J. Nateghi & L. A. Asl, "Evaluation of mutual coupling models for calibrating the antenna arrays for DOA estimation," *European Conference on Antennas and Propagation (EuCAP)*, pp. 1033–1036, 2009.

[53] S. Murphy & P. M. Eyring, "2-18 GHz circular array interferometer DF antenna system," *Antennas and Propagation Society International Symposium*, vol. 4, pp. 2332–2335, 1998.

[54] T. Ouyang, L. Qian, L. Ding & F. Yang, "Mutual coupling calibration for uniform circular array using a single source," *Wireless Communications and Signal Processing (WCSP)*, pp. 1–6, 2014.

[55] C. Qi, Y. Wang, Y. Zhang & H. Chen, "DOA estimation and self-calibration algorithm for uniform circular array," *Electronics Letters*, vol. 41, no. 20, pp. 1092–1094, 2005.

[56] X. Qiu & Z. Zhu, "Mutual coupling calibration using a single source in near field," *Aerospace and Electronics Conference (NAECON)*, pp. 424–426, 1994.

[57] H. Rogier, "Mutual coupling compensation in uniform circular arrays with center element using a coupling matrix based on phase modes," *Antennas and Propagation Society International Symposium*, pp. 1133–1136, 2006.

[58] H. Rogier & E. Bonek, "Analytical spherical-mode-based compensation of mutual coupling in uniform circular arrays for direction-of-arrival estimation," *AEU-International Journal of Electronics and Communications*, vol. 63, no. 6, pp. 179–189, 2005.

[59] H. Rogier, 'Phase-mode-based construction of a coupling matrix for uniform circular arrays with a center element," *Microwave and optical technology letters*, vol. 48, no. 2, pp. 291–298, 2006.

[60] H. Scott & V. F. Fusco, "360^0 electronically controlled beam scan array," *IEEE Transactions on antennas and propagation*, vol. 52, no. 1, pp. 333–335, 2004.

[61] H. Singh, H. L. Sneha & R. M. Jha, "Mutual coupling in phased arrays: a review," *International Journal of Antennas and Propagation*, vol. 2013, 2013.

[62] T. Su & H. Ling, "On modeling mutual coupling in antenna arrays using the coupling matrix," *Microwave and Optical Technology Letters*, vol. 28, no. 4, pp. 231–237, 2001.

[63] T. Su, K. Dandekar & H. Ling, "Simulation of mutual coupling effect in circular arrays for direction-finding applications," *Microwave and optical technology letters*, vol. 26, no. 5, pp. 331–336, 2000.

[64] T. Svantesson, "Modeling and estimation of mutual coupling in a uniform linear array of dipoles," *International Conference on Acoustics, Speech, and Signal Processing*, vol. 5, pp. 2961–2964, 1999.

[65] T. Svantesson, "The effects of mutual coupling using a linear array of thin dipoles of finite length," *IEEE SP Workshop on Statistical Signal and Array Processing*, pp. 232–235, 1998.

[66] T. Takayama & M. Sato, "A novel direction-finding algorithm for directional borehole radar," *IEEE Transactions on Geoscience and Remote Sensing*, vol. 45, no. 8, pp. 2520–2528, 2007.

[67] J. Tao, H. Xu & H. Tao, "Close-form direction finding for multiple scattered sources based on uniform circular arrays with trimmed vector sensor," *World Congress on Intelligent Control and Automation*, pp. 2392–2395, 2008.

[68] B. H. Wang, H. T. Hui & M. S. Leong, "Decoupled 2D direction of arrival estimation using compact uniform circular arrays in the presence of elevation-dependent mutual coupling," *IEEE Transactions on Antennas and Propagation*, vol. 58, no. 3, pp. 747–755, 2010.

[69] M. Wang, X. Ma, S. Yan & C. Hao, "An autocalibration algorithm for uniform circular array with unknown mutual coupling," *IEEE Antennas and Wireless Propagation Letters*, vol. 15, pp. 12–15, 2016.

[70] M. Wax & J. Sheinvald, "Direction finding of coherent signals via spatial smoothing for uniform circular arrays," *IEEE transactions on antennas and propagation*, vol. 42, no. 5, pp. 613–620, 1994.

[71] J. Hilburn, "Circular arrays of radial and tangential dipoles for turnstile antennas," *IEEE transactions on antennas and propagation*, vol. 17, no. 5, pp. 658 – 660, 1969.

[72] H. Wu, Y. Yuan, Z. Zhang & J. Cang, "UCA-based orbital angular momentum radio beam generation and reception under different array configurations," *International Conference on Wireless Communications and Signal Processing*, pp. 1– 6, 2014.

[73] R. J. Weber & Y. Huang, "Performance analysis of direction of arrival estimation with a uniform circular array," *Aerospace Conference*, pp. 1–7, 2012.

[74] A. J. Weiss & B. Friedlander, "Direction finding in the presence of mutual coupling," *Asilomar Conference on Signals, Systems and Computers*, vol. 2, pp. 598–602, 1988.

[75] L. Xiang, Z. Ye, X. Xu, C. Chang, W. Xu & Y. S. Hung, "Direction of arrival estimation for uniform circular array based on fourth-order cumulants in the presence of unknown mutual coupling," *IET microwaves, antennas and propagation*, vol. 2, no. 3, pp. 281–287, 2008.

[76] J. L. Xie, Z. S. He & H. Y. Li, "A fast DOA estimation algorithm for uniform circular arrays in the presence of unknown mutual coupling," *Progress In Electromagnetics Research*, vol. 21, pp. 257–271, 2011.

[77] H. Yamada, Y. Ogawa & Y. Yamaguchi, "Mutual impedance of receiving array and calibration matrix for high-resolution DOA estimation," *International Conference on Wireless Communications and Applied Computational Electromagnetics*, pp. 361–364, 2005.

[78] K. Yang, S.Cai & Z. Q. Luo, "Convex relaxation approaches to maximum likelihood DOA estimation in ULA's and UCA's with unknown mutual coupling," *IEEE International Conference on Acoustics, Speech and Signal Processing (ICASSP)*, pp. 2556–2559, 2011.

[79] Z. Ye, J. Dai, X. Xu & X. Wu, "DOA estimation for uniform linear array with mutual coupling," *IEEE Transactions on Aerospace and Electronic Systems*, vol. 45, no. 1, pp. 280–288, 2009.

[80] G. Ying & W. Bu-hong, "Robust direction finding for uniform circular array with mutual coupling," *Antennas and Propagation Society International Symposium*, vol. 2, pp. 362–365, 2005.

[81] T. T. Zhang, Y. L. Lu & H. T. Hui, "Compensation for the mutual coupling effect in uniform circular arrays for 2D DOA estimations employing the maximum likelihood technique," *IEEE Transactions on Aerospace and Electronic Systems*, vol. 44, no. 3, pp. 1215–1221, 2008.

[82] T. T. Zhang, Y. L. Lu & H. T. Hui, "Simultaneous estimation of mutual coupling matrix and DOAs for UCA and ULA," *International Zurich Symposium on Electromagnetic Compatibility*, pp. 265–268, 2006.

[83] J. H. Richmond, "Coupled linear antennas with skew orientation," *IEEE Transactions on Antennas and Propagation*, vol. 18, no. 5, pp. 694–696, 1970.

[84] K. E. Schmidt, "Simplified mutual impedance of nonplanar skew dipoles," *IEEE Transactions on Antennas and Propagation*, vol. 44, no. 9, pp. 1298–1299, 1996.

[85] J. H. Han, W. Y. Song, K. S. Oh & N. H. Myung, "Simple formula and its exact analytic solution of mutual impedance for nonplanar-skew dipoles," *Progress in Electromagnetics Research*, vol. 132, pp. 551-570, 2012.

[86] J. H. Han, W. Y. Song, K. S. Oh & N. H. Myung, "Analytical derivation of mutual impedance between two arbitrarily located and slanted dipoles using effective length vector," *Asia-Pacific Microwave Conference*, pp. 401-403, 2013.

[87] Y. Okumura, E. Ohmori, T. Kawano & K. Fukuda, "Field strength and its variability in VHF and UHF land-mobile radio service," *Review of the Electrical Communication Laboratory*, vol. 16, no. 9-10, pp. 825-873, 1968.

[88] J.-G. Hong, W.-H. Ahn & B.-S. Seo, "Compensation of mutual coupling in an antenna array for direction of arrival estimation," *International Conference on Advanced Communication Technology*, pp. 599-603, 2013.

[89] H. Ku & J. Kenney, "Behavioral modeling of nonlinear RF power amplifiers considering memory effects," *IEEE Transactions on Microwave Theory and Techniques*, vol. 51, no. 12, pp. 2495-2504, 2003.

[90] J. C. Pedro & S. A. Maas, "A comparative overview of microwave and wireless power-amplifier behavioral modeling approaches," *IEEE Transactions on Microwave Theory and Techniques*, vol. 53, no. 4, pp. 1150-1163, 2005.

[91] M. Isaksson, D. Wisell & D. Ronnow, "A comparative analysis of behavioral models for RF power amplifiers," *IEEE Transactions on Microwave Theory and Techniques*, vol. 54, no. 1, pp. 348-359, 2006.

[92] A. Zhu, J. C. Pedro & T. J. Brazil, "Dynamic deviation reduction-based Volterra behavioral modeling of RF power amplifiers," *IEEE Transactions on Microwave Theory and Techniques*, vol. 54, no. 12, pp. 4323-4332, 2006.

[93] H. Wang, J. Bao & Z. Wu, "Comparison of the behavioral modelings for RF power amplifier With memory effects," *IEEE Microwave and Wireless Components Letters*, vol. 19, no. 3, pp. 179-181, 2009.

[94] F. M. Ghannouchi & O. Hammi, "Behavioral modeling and predistortion," *IEEE Microwave Magazine*, vol. 10, no. 7, pp. 52-64, 2009.

[95] A. S. Tehrani, H. Cao, S. Afsardoost, T. Eriksson, M. Isaksson & C. Fager, "A comparative analysis of the complexity/accuracy tradeoff in

power amplifier behavioral models," *IEEE Transactions on Microwave Theory and Techniques*, vol. 58, no. 6, pp. 1510-1560, 2010.

[96] S. Wei, D. Goeckel & R. Janaswamy, "On the asymptotic capacity of MIMO systems with antenna arrays of fixed length," *IEEE Transactions on Wireless Communications*, vol. 4, no. 4, pp. 1608-1621, 2005.

[97] H. Shin, M. Z. Win & M. Chiani, "Asymptotic statistics of mutual information for doubly correlated MIMO channels," *IEEE Transactions on Wireless Communications*, vol. 7, no. 2, pp. 562-573, 2008.

[98] A. E. Gera, "A simplified computational procedure for the analysis of planar arrays," *IEEE Transactions on Antennas and Propagation*, vol. 32, no. 6, pp. 647-651-284, 1984.

[99] B. Liao & S. C. Chan, "Adaptive beamforming for uniform linear arrays with unknown mutual coupling," *IEEE Antennas and Wireless Propagation Letters*, vol. 11, pp. 464-467, 2012.

[100] B. Friedlander & A. J. Weiss, "Direction finding in the presence of mutual coupling," *IEEE Transactions on Antennas and Propagation*, vol. 39, no. 3, pp. 273-284, 1991.

[101] F. Sellone & A. Serra, "A novel online mutual coupling compensation algorithm for uniform and linear arrays," *IEEE Transactions on Signal Processing*, vol. 55, no. 2, pp. 560-573, 2007.

[102] Z. Ye & C. Liu, "2-D DOA estimation in the presence of mutual coupling," *IEEE Transactions on Antennas and Propagation*, vol. 56, no. 10, pp. 3150-3158, 2008.

[103] A. Azarbar, G. R. Dadashzadeh & H. R. Bakhshi, "Non-sensitive matrix pencil method against mutual coupling," *IEICE Electronics Express*, vol. 8, no. 6, pp. 318-324, 2011.

[104] H. B. Li, Y. D. Guo, J. Gong & J. Jiang, "Mutual coupling self-calibration algorithm for uniform linear array based on ESPRIT," *International Conference on Consumer Electronics, Communications and Networks*. pp. 3323-3326, 2012.

[105] B. Liao & S. C. Chan, "A cumulant-based method for direction finding in uniform linear arrays with mutual coupling," *IEEE Antennas and Wireless Propagation Letters*, vol. 13, pp. 1717-1720, 2014.

[106] W. Si, D. Wu, L. Liu & X. Qu, "Direction finding with gain/phase errors and mutual coupling errors in the presence of auxiliary sensors," *Mathematical Problems in Engineering*, vol. 2014, pp. 1-12, 2014.

[107] R. Roy & T. Kailath, "ESPRIT-estimation of signal parameters via rotational invariance techniques," *IEEE Transactions on Acoustics, Speech, and Signal Processing*, vol. 37, no. 7, pp. 984-995, 1989.

[108] Y. I. Wu, G. P. Arada, K. T. Wong & W. Y. Tam, "Electromagnetic coupling matrix modeling and ESPRIT-based direction finding - a case study using a uniform linear array of identical dipoles," *IET Intelligent Signal Processing Conference*, pp. 1-5, 2015.

[109] G. P. Arada, "Phenomenological Modeling of the Mutual Impedance between Wire Antennas," Ph.D Dissertation, *The Hong Kong Polytechnic University, Hong Kong*, 2017.